# ATTENUATION OF MULTIPLE REFLECTIONS IN IMAGE SPACE

A DISSERTATION
SUBMITTED TO THE DEPARTMENT OF GEOPHYSICS
AND THE COMMITTEE ON GRADUATE STUDIES
OF STANFORD UNIVERSITY
IN PARTIAL FULFILLMENT OF THE REQUIREMENTS
FOR THE DEGREE OF
DOCTOR OF PHILOSOPHY

Gabriel F. Alvarez
August 2007

Printed as Stanford Exploration Project No. THESIS
by permission of the author

I certify that I have read this dissertation and that, in my opinion, it is fully adequate in scope and quality as a dissertation for the degree of Doctor of Philosophy.

(Biondo L. Biondi) Principal Adviser

I certify that I have read this dissertation and that, in my opinion, it is fully adequate in scope and quality as a dissertation for the degree of Doctor of Philosophy.

(Jon F. Claerbout)

I certify that I have read this dissertation and that, in my opinion, it is fully adequate in scope and quality as a dissertation for the degree of Doctor of Philosophy.

(Gary Mavko)

Approved for the University Committee on Graduate Studies.

# Abstract

In complex subsurface areas, attenuation of specular and diffracted multiples in image space (after migration) is an attractive alternative to the industry standard processes of Surface Related Multiple Elimination (SRME) and data space Radon demultiple. There are several reasons: (1) migration increases the signal-to-noise ratio of the data; (2) migration guarantees that the primaries are mapped to coherent events in either Subsurface Offset Domain Common Image Gathers (SODCIGs) or Angle Domain Common Image Gathers (ADCIGs); (3) unlike data space, image space is by construction regular and usually much smaller; (4) the moveout of the multiples in image space is more predictable than in data space for complex geology; (5) attenuating the multiples in data space may leave "holes" in the frequency-wavenumber space that generate artifacts and amplitude problems after migration.

In this thesis I exploit the power of prestack wave-equation migration to handle complex wave propagation. I design a robust and efficient method to attenuate the multiples in image space via a Radon transform of ADCIGs.

I demonstrate that specular multiples migrate as primaries and develop the equations for their residual moveout in both SODCIGs and ADCIGs for canonical models. In particular, I develop a new equation for the residual moveout of multiples in ADCIGs that accounts for ray bending at the multiple-generating interface. The new equation improves the accuracy of the tangent-squared approximation for the residual moveout of primaries migrated with the wrong velocity (Biondi and Symes, 2004). The tangent-squared equation is shown to be appropriate for multiples only at small aperture angles. A Radon transform whose kernel is the new equation better focuses the multiples and helps separate them from the primaries. This in turn

improves the attenuation of the multiples. Unlike specular multiples, diffracted multiples do not migrate as primaries. That is, they do not map to zero subsurface offset in SODCIGs nor to flat events in ADCIGs even if migrated with their correct velocities. Furthermore, I show that the apex of their residual moveout in ADCIGs is shifted from zero aperture angle similar to their behavior in common midpoint gathers. I design an apex-shifted Radon transform that, for 2D data, maps the 2D ADCIGs to a 3D cube of dimensions depth, curvature and apex-shift distance. I show, with a real 2D dataset from the Gulf of Mexico, that Radon filtering with the apex-shifted transform is effective in attenuating both specular and diffracted multiples.

Estimating a multiple model is the first part of the multiple attenuation process, but it is not the only critical step. In order to estimate the primaries we need to subtract the estimated multiples from the data. Because of amplitude, phase and kinematic errors in the multiple estimate, straight subtraction is inaccurate and some form of adaptive subtraction is often needed. I propose to pose the adaptive matching and subtraction of the multiple model from the data as an iterative least-squares problem that simultaneously matches the estimates of both primaries and multiples to the data. Once converge is achieved, the primary and multiple estimates are updated and the inversion is run again. Standard methods match only the estimate of the multiples. The simultaneous matching of the primaries and the multiples has the advantage of reducing the crosstalk between the matched estimates of the primaries and the matched estimate of the multiples. I demonstrate the method with real and synthetic data and show that it produces better results than the standard multiples-only adaptive subtraction. I also show that the method can be used to tackle similar problems where estimates of signal and noise need to be matched to data containing both, and illustrate it by attenuating spatially-aliased ground-roll from a land shot gather.

In 3D, the multiples exhibit residual moveout in SODCIGs in both the inline and crossline offset directions. They map away from zero subsurface offset when migrated with the faster velocity of the primaries. The ADCIGs are function not only of the aperture angle but also of the reflector azimuth. I show, with a simple 3D synthetic dataset, that the residual moveout of the primaries as a function of the aperture angle is flat for those angles that illuminate the reflector at that reflection azimuth, but appear to have curvature for those reflection azimuth planes that do not illuminate the reflector. The multiples, on the other hand, have residual

moveout towards increasing depth for increasing aperture angles at all azimuths. Likewise, as a function of azimuth, and for a given aperture angle, the primaries show good azimuth resolution for large aperture angles that illuminate the reflector. At zero aperture angle there is no azimuth resolution. For the multiples from a reflector with crossline dip there is no azimuth resolution at any aperture angle because, even in constant velocity, the propagation is not on one plane.

I show, with a real 3D dataset from the Gulf of Mexico, that even below salt, where illumination is poor, and where the requirements of 3D-SRME are less likely to be met, there is enough residual moveout in ADCIGs to discriminate and attenuate the multiples with a direct application of the new 2D Radon transform in planes of azimuth-stacked ADCIGs.

# Preface

The electronic version of this thesis[1] makes the included programs and applications available to the reader. The markings [ER], [CR], and [NR] are promises by myself about the reproducibility of each figure result. Reproducibility is a way of organizing computational research that allows both the author and the reader of a publication to verify the reported results. Reproducibility facilitates the transfer of knowledge within SEP and between SEP and its sponsors.

**ER** denotes Easily Reproducible and are the results of processing described in the paper. I claim that you can reproduce such a figure from the programs, parameters, and makefiles included in the electronic document. The programs are present locally in the different directories or available in the SEP data library[2]. I assume you have a UNIX workstation with Fortran, Fortran90, C, Matlab, X-Windows system and the software downloadable from our website (SEP makerules, SEPlib, and the SEP latex package), or other free software such as SU. Before the publication of the electronic document, someone other than me tested my claim by destroying and rebuilding all ER figures. Some ER figures may not be reproducible by outsiders because they depend on data sets that are too large to distribute.

**CR** denotes Conditional Reproducibility. I certify that the commands are in place to reproduce the figure if certain resources are available. SEP staff have only attempted to make sure that the makefile rules exist and the source codes referenced are provided. The primary reasons for the CR designation is that the processing requires 2 hours or more or

[1] http://sepwww.stanford.edu/public/docs/sep121
[2] http://sepwww.stanford.edu/public/docs/sepdatalib/toc_html/

a special hardware such as computer cluster. In Chapters 5 and 6, proprietary data from CGGVeritas cannot be used without written permission. All the Figures displaying this dataset are CR.

**NR** denotes Non-Reproducible figures. SEP discourages authors from flagging their figures as NR except for figures that are used solely for motivation, comparison, or illustration of the theory, such as: artist drawings, scannings, or figures taken from SEP reports not by the authors or from non-SEP publications.

Our testing is currently limited to LINUX 2.4 using the Intel Fortran90 compiler, but the code should be portable to other architectures. Reader's suggestions are welcome. For more information on reproducing SEP's electronic documents, please visit
`<http://sepwww.stanford.edu/research/redoc/>`.

# Acknowledgments

I would like to express my sincere appreciation to Dr. Jan Pajchell of Norsk Hydro for helping me secure permission to use the 3D real dataset from the Gulf of Mexico. In SEP, getting good, challenging real 3D data, is half the struggle in completing a Ph.D. I would not have been able to get my hands onto this great dataset without Dr. Pajchel's efforts. I also thank him for many nice technical discussions and for providing the migration velocity model.

Thanks to professors Jon Claerbout and Biondo Biondi that gave me the opportunity to come to SEP and allowed me to complete my Ph.D. even when it was clear that we did not see eye-to-eye on most things. I appreciate the elbow room they provided me.

Thanks also to Mr. Hal Dean and the anonymous donors of the Escondido Family fund without whose grants I would have had a very tough time supporting my family all the years at Stanford.

I shared my time at Stanford with many other students. Special mention to Brad Artman with whom I had many technical discussions and whose shot profile migration code I used to compute the results with the real dataset. Brad and I shared somewhat similar experiences at SEP and bonded as a result. I also had a nice friendship with Daniel Rosales, Alejandro Valenciano and Bill Curry. I thank Antoine Guitton for many useful suggestions through the years. Morgan Brown, Jeff Shragge, Marie Clapp and Jesse Lomask also shared with me many coffee breaks and personal and technical discussions. More recently, Madhav Vyas, Yaxun Tang, Piere Jousselin, Satyake Sen, Ben Witten, GBoyega Ayeni, Roland Gunther and Claudio Cardozo were also nice students to be around. Last, but not least, I want to mention my very good Colombian friends Mario Gutierrez, Elizabeth Diaz and Juan Mauricio Florez.

A student could not have graduated from SEP in the last few years and not have a lot to owe to Bob Clapp. Bob always seems to know what is wrong with SEP computers, SEP software and SEP in general. Most people who know Bob know that he is a computer wizard but may not realize how good a geophysicists he is. He has become a de-facto coadvisor of all SEP students. Thank you Bob. Thanks also to Diane Lau who keeps everything running smoothly with apparent little effort and always with a nice smile in her face. In seven years I can not recall seen Diane in a bad mood. She is that great combination of a niceness and efficiency. Tara Ilych also deserves special mention. For the short time she has been in the geophysics department we have all felt the improvement she has made.

Thanks to the professors in the geophysics department, in particular professor Gary Mavko who agreed to be in my committee and whose rock physics class was one of the best I took, rivaled only by the other rock physics class by Jack Dvorkin. I also like to thank professors Simon Klemperer for giving me the chance to do some small piece of work with the SAFOD project and Mark Zoback for his excellent geomechanics class.

I will always be indebted to Doug Hanson of ConocoPhillips for his encouragement and his kindness toward me. It is not every day that you come across an accomplished programmer, who is also an outstanding researcher and a really nice, supportive person. Thank you very much Doug. Thanks to John Etgen of BP for many suggestions on the thesis manuscript.

Thanks to CGGVeritas for providing the 3D real dataset, NOrsk Hydro for providing the migration velocity model for the 3D dataset, ExxonMobil for providing the 3D synthetic dataset and WesternGeco for providing the 2D real dataset. Thanks to the sponsors of SEP.

La última parte de los agradecimientos la dejo para mi familia, con la inveterada costumbre latina de dejar lo mejor para el final. Mi esposa Nancy Coral y mis hijos Cesar Augusto y Gabriel José estuvieron a mi lado todos estos largos años y son parte integral del resultado. Por Uds. y para Uds. A mi mamá, a mis hermanos y a mi hermana muchas, muchas gracias.

# Contents

# List of Figures

# Chapter 1

# Introduction

Subsurface images provided by the seismic reflection method are the single most important tool used in oil and gas exploration. Almost exclusively, our conceptual model of the seismic reflection method, and consequently our seismic data processing algorithms, treat primary reflections, those waves that are scattered back towards the surface only once, as the "signal". The traveltimes of the primary reflections are used to map the structure of lithology contrasts while their amplitudes provide information about the magnitude of the lithology contrasts as well as other information such as presence or absence of fluids in the pore spaces of the rock. All other waves such as multiples, waves that are scattered back toward the surface more than once, are considered "noise".

## CLASSIFICATION OF MULTIPLES

There are many types of multiples, some of which are illustrated in Figure 1.1. For the purpose of this thesis, however, multiples will be classified in two main categories: specular multiples and diffracted multiples. Specular multiples are those that reflect as light rays, following Snell's law at the reflection points. Diffracted multiples, in contrast, are scattered in all directions at the diffractor location. I will further classify the diffracted first-order multiples into receiver-side and source-side multiples depending on which side the diffractor lies as

shown in panels (a) and (b) of Figure 1.2 respectively. The dashed lines represent the arbitrary trajectories that the multiple may take from the diffractor to the receiver (for a receiver-side diffracted multiple) or from the source to the diffractor (for a source-side diffracted multiple). The travelpath from the diffractor to the receiver is independent of the source location for a receiver-side multiple and likewise the travelpath from the source to the diffractor is independent of the receiver location for a source-side multiple. This behavior makes the kinematics of specular and diffracted multiples very different in Common-midpoint (CMP) gathers. Specular multiples have a moveout curve that is symmetric around their apex at zero offset, since reciprocity requires the same traveltime for rays from the source location to the receiver location and from the receiver location to the source location. Diffracted multiples, on the other hand, do not have their apex at zero offset (Hargreaves et al., 2003) and are therefore not symmetric around zero offset as shown in Figure 1.3. The travelpath of the receiver side multiple, for example, is not the same if the source and receiver locations are interchanged. Reciprocity is not violated, however. Receiver-side multiples just become source-side multiples and vice-versa as illustrated in Figure 1.2. A similar splitting of the source- and receiver-side multiple happen with peg-leg multiples from a dipping reflector (Levin and Shah, 1977).

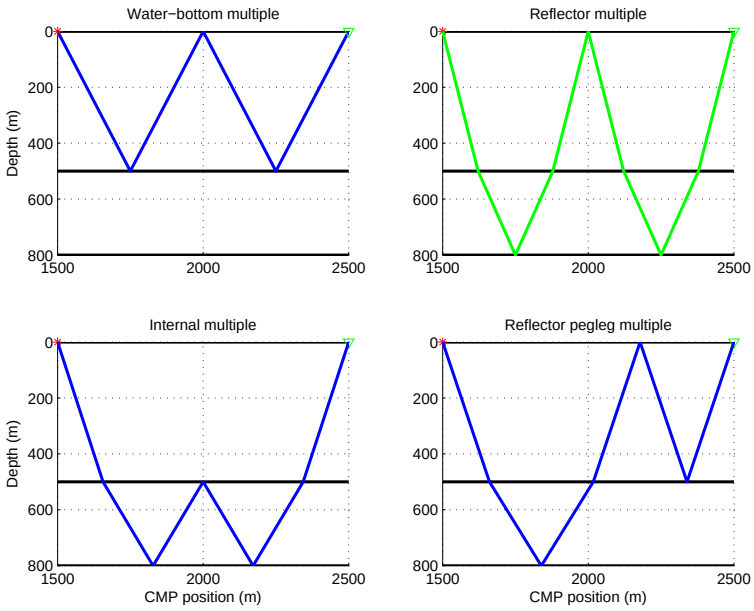


Figure 1.1: Examples of 2D specular multiples. intro-rays [ER]

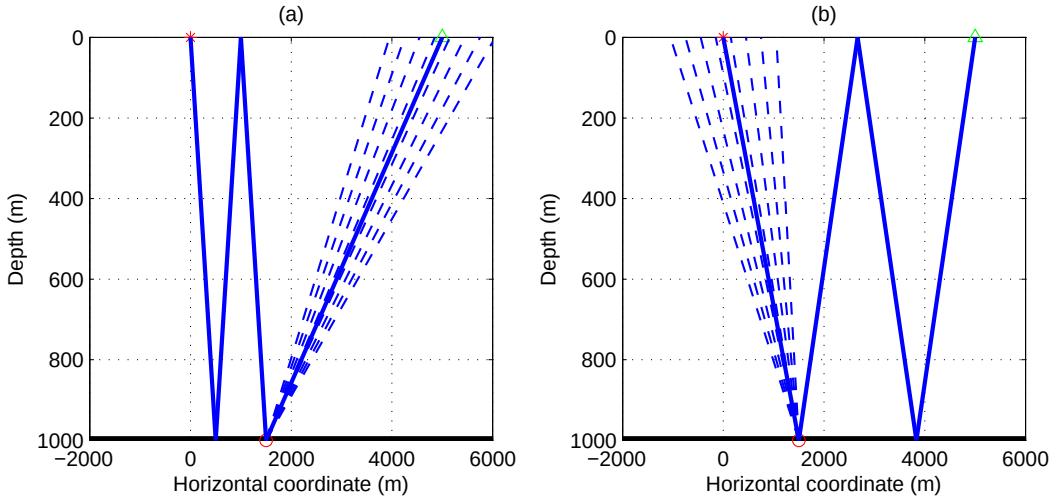


Figure 1.2: Schematics of receiver-side (a) and source-side (b) diffracted multiples. The asterisk represents the source and the triangle represents a receiver. The dashed lines indicate possible trajectories of the diffracted rays from the diffractor to the receiver or from the source to the diffractor. The diffractor itself is indicated by the empty circle at about 1600 m. intro-diffracted_muls_rays [ER]

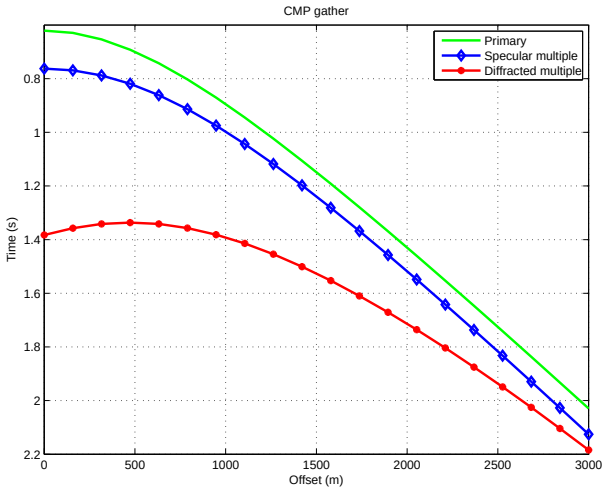


Figure 1.3: Comparison of the move-out curves of a primary, a specular multiple and a diffracted multiple in a CMP gather. Notice that the apex of the diffracted multiple is not at zero offset. intro-moveouts3 [ER]

## DATA SPACE AND IMAGE SPACE

In this thesis, I refer to data space as the un-migrated space. This means data as a function of time. I consider two main sets of data: source gathers and CMP gathers. The first are function of the source coordinates, offsets and time while the second are function of the CMP coordinates, *half*-offsets and time.

I will refer to image space as the domain of migrated data. In particular, data migrated in depth. In image space I consider two main datasets: Subsurface Offset Common Image Gathers (SODCIGs) and Angle Domain Common Image Gathers (ADCIGs). In this thesis I will use exclusively wave-equation migration algorithms.

## ATTENUATION OF MULTIPLES IN DATA SPACE

The standard approach in seismic data processing is to attenuate the multiples before imaging, that is, in data space. Most algorithms for the attenuation of multiples in data space are based on three main characteristics of the multiples: (1) their periodicity in arrival time (predictive deconvolution), (2) their difference in moveout with respect to the primaries in CMPs ( $f$-$k$ and $\tau$-$p$ filtering) and (3) their predictability as the auto-convolution of the primaries (Surface Related Multiple Elimination (SRME)). Each of these approaches have distinctive advantages and disadvantages.

### Predictive deconvolution

The attenuation of short-period multiples (most notably reverberations from relatively flat, shallow water-bottom) can be achieved with predictive deconvolution. The periodicity of the multiples is exploited to design an operator that identifies and removes the predictable part of the wavelet (multiples), leaving only its non-predictable part (signal). The key assumption is that genuine reflections come from an earth reflectivity series that can be considered random and therefore not predictable (Yilmaz, 1987). In general, for other than short-period multiples, only moderate success can be achieved with this simple, one-dimensional procedure.

In principle, deterministic deconvolution can be used to remove water-bottom reverberations when the exact depth and speed of sound of the water layer are known. Since these conditions are rarely met, deterministic deconvolution is not widely used, despite the elegance of its closed, exact mathematical formulation (Robinson and Treitel, 2000).

**Moveout-based filtering**

Primaries and multiples exhibit hyperbolic moveout in CMPs but their curvature is different. After Normal Moveout (NMO) correction with the NMO velocity of the primaries, ideally the primaries exhibit flat moveout whereas the residual moveout of the multiples can be approximated by parabolas or hyperbolas (Hampson, 1986; Foster and Mosher, 1992). This difference in moveout can be exploited to separate the primaries from the multiples in either the $f$-$k$ domain or the $\tau$-$p$ (Radon) domain.

The performance of an $f$-$k$ filter in suppressing multiples strongly depends on primary and multiple reflections being mapped to separate regions of the $f$-$k$ plane. This is in general the case on far-offset traces, for which the difference in moveout can be large, but not on short-offset traces for which the difference in moveout is small. The performance of $f$-$k$ filtering, therefore, is poor at small offsets even if the subsurface geology is not very complex. This usually makes $f$-$k$ filtering an undesirable option for multiple elimination.

Radon demultiple in data space (Hampson, 1986; Foster and Mosher, 1992) has proven successful in attenuating specular multiples if the subsurface is not very complex. In complex subsurface areas, such as under salt, the hyperbolic or in fact any NMO approximation breaks down. The NMO velocities are inaccurate and therefore, after NMO, the primaries are unlikely to be flat. Furthermore, the residual moveout of the multiples is unlikely to be well approximated by parabolas or hyperbolas. The quality of the separation between primaries and multiples in the Radon domain, and their focusing, therefore, deteriorates. As a result, multiples are imperfectly attenuated and, worse, the attenuation is offset dependent. In such complex areas, Radon demultiple in data space is not a good option.

**SRME**

Surface-related multiple elimination (SRME) uses the recorded seismic data to predict and iteratively subtract the multiple series (Verschuur et al., 1992). The key advantage of SRME is that it needs no subsurface information whatsoever. The multiples are completely predicted from the data. 2D SRME can deal with all kinds of surface-related 2D multiples, provided all relevant data are recorded within the aperture and offset limitations of the survey line. Predicting 3D multiples with 2D SRME is hazardous because the accuracy of the prediction depends on the amount of crossline dip. Figure 1.4 shows an example with 3D real data. Panel (a) is an inline common-offset section with an obvious water-bottom multiple. Panel (b) is the inline offset gather taken at horizontal position 12000 m. Panel (c) is the multiple prediction with 2D SRME and panel (d) is the offset gather for the predicted data (figure courtesy of Bill Curry). The prediction is very good except at the canyon where the water-bottom has non-negligible crossline dip. Notice that the predicted multiple arrives later than the multiple in the data inside the canyon but arrives at the correct times to either side of the canyon.

Prediction of multiples from reflectors with crossline dip, and diffracted multiples, especially those from scatterers with a cross-line offset component, cannot be accurately achieved with 2D SRME. Predicting these multiples requires the much more expensive 3D SRME. If the acquisition of the 3D survey is regular and dense enough, the survey apertures large enough in both in-line and cross-line directions, and there is no feathering, 3D SRME performs well. With standard marine streamer acquisition, however, the sampling in the cross-line direction is too coarse, the cross-line aperture is too narrow, short offsets are not recorded and feathering and acquisition obstacles make the acquisition geometry irregular. Any multiple whose surface bounce is not recorded can not be predicted by 3D SRME. Again, diffracted multiples, and multiples from a reflector with significant crossline dip pose the most serious problem because their surface bounce is likely to lie way outside the relatively narrow recording patch. Figure 1.5 shows a schematic map view of this situation. The empty circle represents the surface bounce of the multiple and, since there is not detector at that location, 3D SRME cannot predict that multiple. We do not need a particularly convoluted subsurface for this situation to arise in practice. All it takes is crossline dip of the water-bottom or the multiple-generating surface, or the presence of diffractors. These multiples, therefore, need to be removed by

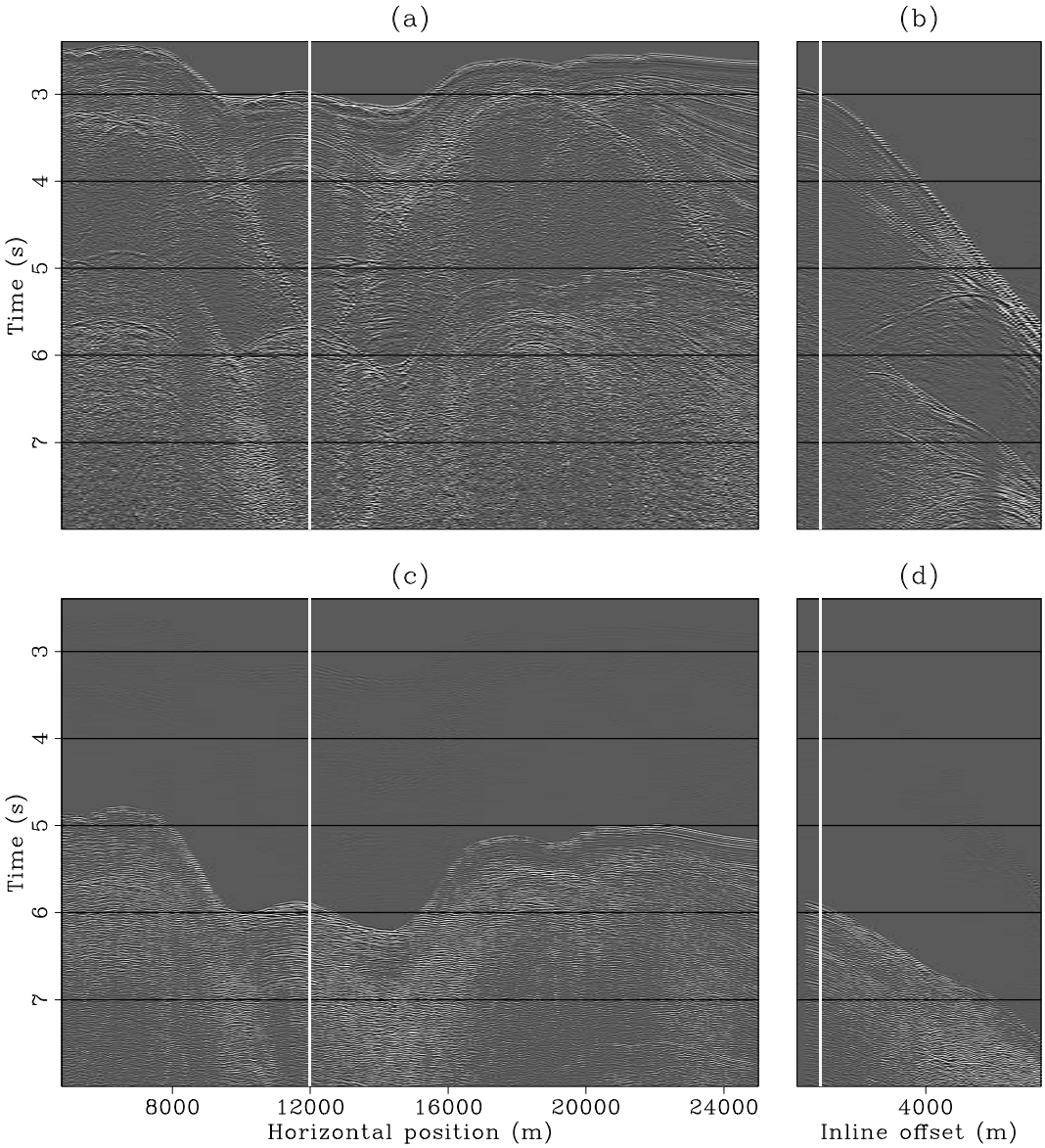


Figure 1.4: Prediction of 3D multiple with 2D SRME. Panel (a) is an inline common-offset section from a 3D survey. Panel (b) is an offset gather. Panel (c) is the inline common-offset section of the predicted multiple with 2D SRME and panel (d) is the offset gather of the predicted multiple. Notice that the prediction is good away from the canyon (the arrival times of the predicted multiple match those of the data) but no in the canyon where the predicted arrival times of the multiple are larger due to the crossline dip of the canyon. intro-bill [ER]

other methods (Hargreaves et al., 2003) or the data need to be interpolated and extrapolated to a dense, large aperture grid (Baumstein and Hadidi, 2006; Curry, 2006; Matson and Abma, 2005; van Dedem and Verschuur, 1998; Nekut, 1998). Interpolation is complicated by the coarse sampling that may introduce aliasing in the steep flanks of the multiple multiple move-out curves. Also, internal multiples cannot be predicted by SRME, unless the data is successively datumed to every multiple-generating interface. This is obviously a time-consuming process that is seldom, if ever, carried out. In most situations this is not a serious drawback, however, since internal multiples are usually weak. The exception is internal multiples from very strong reflectors such as salt boundaries.

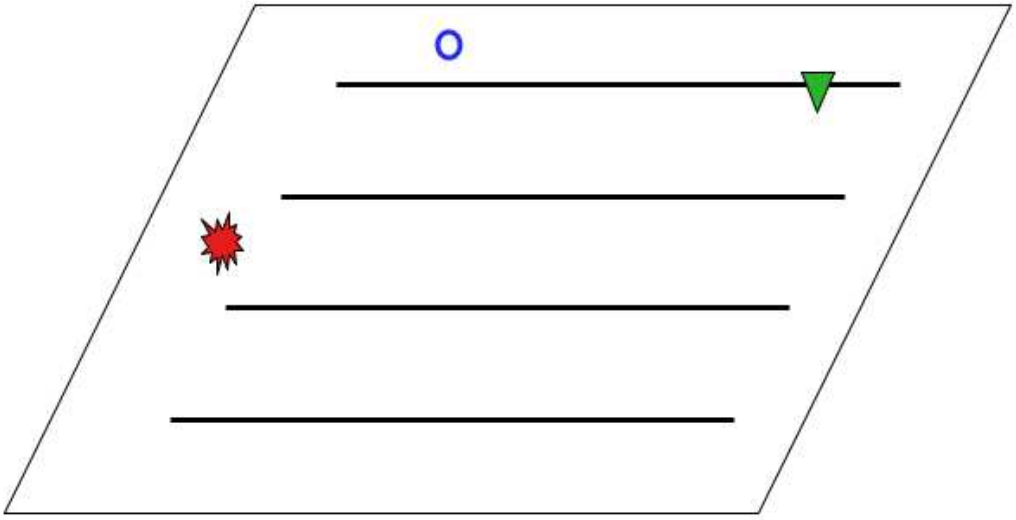

Figure 1.5: Schematic map view of a simple situation in which 3D SRME can not predict a multiple. The subsurface has significant crossline dip such that the surface bounce of the multiple (indicated by the empty circle), lies outside of the recording patch and therefore the multiple can not be predicted from the data. intro-3dsrme_sktch1 [NR]

## PROBLEM DESCRIPTION

The previous section briefly described the weaknesses of the standard multiple attenuation approaches in particular when applied to sparse 3D data over complex subsurface. Data space methods cannot handle the wave distortions associated to complex wave travelpaths and 3D

SRME requires data that is not usually acquired.

The issue I address in this thesis is the development of a relatively simple, practical algorithm, that can attenuate both specular and diffracted multiples for 2D and 3D data acquired with standard marine, narrow-azimuth towed-streamer geometry. The method uses only the recorded data and does not need costly and often inaccurate massive data interpolation and extrapolation. It does, however, require a reasonably accurate migration velocity field. The algorithm works in the image space, meaning it is applied after the data have been migrated. Since wave equation migration accurately handles complex wave propagation, the method works well for data acquired over complex subsurface regions such as under salt, again, provided the migration velocity field is reasonably accurate.

This thesis also makes theoretical contributions that explain the process by which prestack wave equation migration maps multiples from data space (CMP gathers) to image space (ADCIGs). In particular, I develop the equations that explain the residual moveout of canonical multiples in ADCIGs for both specular and diffracted multiples. I demonstrate that the specular multiples are focused similar to primaries whereas the diffracted multiples are not. For 3D data I demonstrate that the reflection azimuth dependency as a function of the dip angle is different for primaries and multiples. Likewise for the aperture angle dependency as a function of reflection azimuth. I develop a Radon transform that separates the primaries from the multiples as a function of both aperture and reflection azimuth angles.

I also develop in this thesis a new approach to the matching and adaptive subtraction of the multiple model from the data. Unlike SRME, the image space Radon transform allows the estimation of a primary model along with the estimation of the multiple model. I exploit this capability to design a nonlinear inversion approach that simultaneously matches and adaptively subtracts from the data both the estimate of the multiples and the estimate of the primaries. The effect is to reduce the well-known crosstalk problem, *i.e.*, that residual multiple energy that contaminates the estimate of the primaries.

## THESIS OVERVIEW

The next chapters develop the subject of the thesis for both 2D and 3D data. In both cases I illustrate the results with synthetic and real data.

### Chapter 2: Attenuation of 2D multiples

In this chapter I present the equations that map specular and diffracted 2D multiples from data space to image space. I implement an apex-shifted Radon transform that separates primaries from specular and diffracted multiples in the Radon domain as a function of depth, residual moveout curvature, and apex shift. I then apply the method to a real 2D line from the Gulf of Mexico plagued with strong subsalt specular and diffracted multiples. I show that most of the multiples can be attenuated without significantly affecting the amplitudes of the primaries.

### Chapter 3: Simultaneous matching and adaptive subtraction of primaries and multiples

In this chapter I address the issue of subtracting an estimated multiple model from data containing primaries and multiples. This is a key step in multiple attenuation methods such as SRME in which the multiple model is expected to have wavelet differences with respect to the data. Instead of just matching and adaptively subtracting the multiple model, I simultaneously match the estimates of both the primaries and the multiples to the data. This has the key advantage of reducing the crosstalk from the multiples in the final estimate of the primaries. I illustrate the method with both synthetic and real 2D data in CMP and angle gathers. Furthermore, I show that the method can be used beyond the attenuation of multiples by applying it to the matching and adaptive subtraction of ground-roll. The adaptive subtraction presented in this chapter is used to compute the results of Chapter 6.

**Chapter 4: Mapping of 3D multiples to image space: Theory and a synthetic data example**

The main problem in the attenuation of multiples is with narrow-azimuth towed-streamer 3D data. In this chapter I extend the basic equations for the residual moveout of specular multiples in ADCIGs for 3D data. I show that the mapping of the multiples is similar to the 2D case, except that the crossline dip generates an azimuth dependency that is different for primaries and multiples. I use a simple 3D synthetic prestack dataset with two primary reflections and two specular multiples to illustrate the mapping of the multiples to 3D ADCIGs. Since the 3D ADCIGs are function of both aperture angle and reflection azimuth, their interpretation is not trivial. I describe in some detail the information contained in the 3D ADCIGs and show how the multiples and the primaries have very different residual moveout. This chapter lays the foundation for the application of the method to the real 3D dataset of Chapters 5 and 6.

**Chapter 5: Imaging and mapping 3D multiples to image gathers: Example with a Gulf of Mexico dataset.**

In this chapter I illustrate the mapping of 3D multiples to image space with a real 3D dataset from the Gulf of Mexico. The data has all the usual shortcomings associated with marine streamer acquisition: sparse sampling in the crossline direction, small crossline aperture, strong feathering, irregularity in the sail lines and uneven midpoint fold. I use shot-profile migration to compute SODCIGs and from them compute 3D ADCIGs. I show that in this case we can discriminate between primaries and multiples in both inline and the crossline subsurface offsets in SODCIGs and aperture and reflection azimuth in ADCIGs, despite the relatively narrow range of aperture angles that illuminate the subsalt reflectors.

**Chapter 6: Attenuation of 3D subsalt multiples with Gulf of Mexico dataset**

In this chapter I tie up the different components presented in the previous chapters. I attenuate subsalt multiples from the real dataset migrated in the previous chapter. I show that some multiple attenuation can be achieved by muting the multiple energy away from zero subsurface

offsets in SODCIGs and stacking the results. I obtain much better attenuation of the multiples by applying Radon filtering on azimuth-stacked ADCIGs.

**Chapter 7: Conclusions**

This last chapter summarizes the conclusions of the thesis.

# Chapter 2

# Image space mapping and attenuation of 2D specular and diffracted multiples


**SUMMARY**

In complex areas, attenuation of specular and diffracted multiples in image space is an attractive alternative to surface-related multiple elimination (SRME) and to data space Radon filtering. In this chapter I present the equations that map, via wave-equation migration, 2D diffracted and specular water-bottom multiples from data space to image space. I show the equations for both subsurface-offset-domain common-image-gathers (SODCIGs) and angle-domain common-image-gathers (ADCIGs). I demonstrate that when migrated with sediment velocities, the over-migrated multiples map to predictable regions in both SODCIGs and ADCIGs. Specular multiples migrate as primaries whereas diffracted multiples do not. In particular, the apex of the residual moveout curve of diffracted multiples in ADCIGs is not located at zero aperture angle.

I use the equation I derive for the residual moveout of the multiples in ADCIGs to design an apex-shifted Radon transform that maps the 2D ADCIGs into a 3D model space cube whose dimensions are depth, residual moveout curvature and apex-shift distance. Well-corrected primaries map to or near the zero curvature plane and specularly-reflected multiples map to

or near the zero apex-shift plane. Diffracted multiples map elsewhere in the cube according to their curvature and apex-shift distance. Thus, specularly reflected as well as diffracted multiples can be attenuated simultaneously. I show the application of the apex-shifted Radon transform to a 2D seismic line from the Gulf of Mexico. Diffracted multiples originate at the edges of the salt body and I show that I can successfully attenuate them, along with the specular multiples, in the image Radon domain.

## INTRODUCTION

In the previous chapter, I described the shortcomings of the standard multiple attenuation methods when the subsurface is complex or the acquisition geometry is sparse, irregular or affected by feathering. With 2D data, SRME is very effective except for diffracted multiples whose surface bounce may be well outside the recording cable.

In this chapter I introduce an alternative method to SRME and data space Radon demultiple. The method attenuates the multiples in the image space rather than in the data space. Prestack wave-equation depth migration accurately handles the complex wave propagation of primaries (Biondi, 2006), to the extent that the presence of the multiples allows an accurate estimation of the migration velocities. The residual moveout of primaries in angle-domain common-image gathers (ADCIGs), therefore, is likely to be flat. It is not immediately obvious, however, what the residual moveout of the over-migrated multiples is in ADCIGs. In order to maximize the separation of primaries and multiples in the Radon domain, the kernel of the Radon transform should approximate the functional dependency of the residual moveout of the multiples as a function of the aperture angle as much as possible. Sava and Guitton (2003) and Alvarez et. al. (2004) used the tangent-squared approximation of Biondi and Symes (2004) assuming that the residual moveout of the multiples is the same as that of primaries migrated with faster velocity. The tangent-squared approximation, however, is a straight ray approximation that is appropriate for events, such as primaries, whose migration velocity is likely to be close to the actual propagation velocity. Multiples, on the other hand, given their large difference in velocity with respect to that of the primaries, are likely to be severely over-migrated and the straight ray approximation is not appropriate for them.

Primaries are migrated to zero subsurface offsets in SODCIGs and with flat moveout in ADCIGs (Biondi, 2006). I show that 2D specular water-bottom multiples, even from dipping water-bottom, are focused by wave-equation migration similar to primaries. Hence, if migrated with constant water velocity, they too are mapped to zero subsurface-offset in SODCIGs and with flat moveout in ADCIGs. When migrated with the velocity of the primaries, specular water-bottom multiples are over-migrated and thus do not map to zero subsurface offsets. For off-end geometry, they are mapped to subsurface offsets with the opposite sign to that of their surface offsets. I derive the moveout curve of these multiples in SODCIGs and ADCIGs. I then take the special case of the residual moveout of a specular multiple from flat water-bottom in ADCIGs and use it to design a Radon transform that accounts for ray-bending of the multiple raypath at the multiple-generating interface. This Radon transform improves the separation of primaries and multiples in the Radon domain compared with a Radon transform based on the tangent-squared approximation.

Water-bottom diffracted multiples do not migrate as primary reflections. That is, they do not focus to zero subsurface offset even if migrated with constant water velocity (Alvarez, 2005). These multiples migrate to both positive and negative subsurface offsets in SODCIGs depending on the relative position of the diffractor with respect to the receiver (for receiver-side diffracted multiples). In ADCIGs, these multiples have their apex at non-zero aperture angle, similar to their behavior in data space (CMP gathers) (Alvarez, 2005). I propose to attenuate these multiples with an apex-shifted Radon transform similar to that used by Alvarez et. al. (2004) but replacing the tangent-squared Radon kernel with the new equation that I derive in this chapter for the residual moveout of the multiples in ADCIGS. Apex-shifted Radon Apex-shifted transforms were introduced for data interpolation by Trad (2003) and for attenuation of diffracted multiples in data space by Hargreaves (2003).

In this chapter I limit the application of the method to 2D data. In Chapter 4 I show the extension of the method to 3D data using the methodology developed by Biondi and Tisserant (2004) to compute 3D ADCIGs. Unlike the 2D ADCIGs used here, the 3D ADCIGs are a function not only of the aperture angle but also the reflection azimuth angle. More important, 3D specular multiples have their apex shifted shifted away from zero aperture angle if the water-bottom or the multiple-generating interface have crossline dip. These multiple,

therefore, behave as diffracted multiples and can be attenuated with a modified version of the apex-shifted Radon transform presented in this chapter.

## KINEMATICS OF 2D MULTIPLES IN IMAGE SPACE

In this section I give the equations that map first-order water-bottom multiple reflections from data space (CMP gathers) to image space (SODCIGs and ADCIGs) and study in detail the special case of a specular multiple from a flat water-bottom. The equation that I derive for the residual moveout of the multiples in ADCIGs for this special case will be the basis for the attenuation of the multiples in the Radon domain. Alvarez (2005) gives parametric equations for other simple cases: specular multiple from a dipping water-bottom and diffracted multiples from flat and dipping water-bottom.

### General formulation

The propagation path of a first-order water-bottom multiple generated by a planar dipping reflector, as shown in Figure 2.1, consists of four segments, such that the total travel-time for the multiple is given by

$$t_m = t_{s_1} + t_{s_2} + t_{r_2} + t_{r_1}, \tag{2.1}$$

where the subscript $s$ refers to the source-side rays and the subscript $r$ refers to the receiver-side rays. The data space coordinates are $(m_D, h_D, t_m)$ where $m_D$ is the horizontal position of the common-midpoint (CMP) gather and $h_D$ is the half-offset between the source and the receiver.

Wave-equation migration maps the CMP gathers to SODCIGs with coordinates $(m_\xi, h_\xi, z_\xi)$ where $m_\xi$ is the horizontal position of the image gather, and $h_\xi$ and $z_\xi$ are the half subsurface-offset and the depth of the image, respectively. As illustrated in the sketch of Figure 2.2, at any given depth the spatial coordinates of the downward-continued source and receiver rays

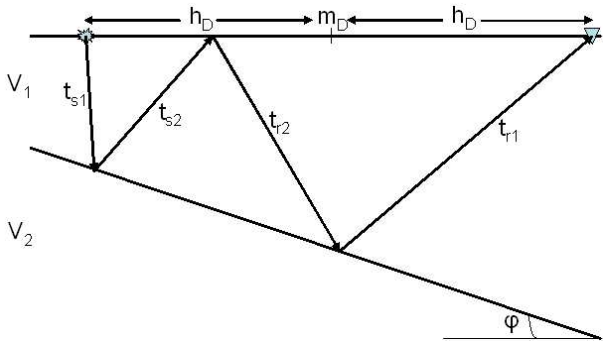


Figure 2.1: Water-bottom multiple. The subscript $s$ refers to the source and the subscript $r$ to the receiver. 2d-mul_sktch1 [NR]

are given by:

$$x_{s_\xi} = m_D - h_D + V_1(t_{s_1}\sin\alpha_s + \rho\tilde{t}_{s_2}\sin\beta_s), \quad (2.2)$$

$$x_{r_\xi} = m_D + h_D - V_1(t_{r_1}\sin\alpha_r + \rho\tilde{t}_{r_2}\sin\beta_r), \quad (2.3)$$

where $V_1$ is the water velocity, $\rho = V_2/V_1$ with $V_2$ the sediment velocity, $\alpha_s$, $\alpha_r$ are the takeoff angles of the source and receiver rays with respect to the vertical and $\beta_s$ and $\beta_r$ are the angles of the refracted source and receiver rays, respectively. The coordinates of the migrated multiple in the image space are given by:

$$h_\xi = \frac{x_{r_\xi} - x_{s_\xi}}{2} = h_D - \frac{V_1}{2}\left[t_{s_1}\sin\alpha_s + t_{r_1}\sin\alpha_r + \rho(\tilde{t}_{s_2}\sin\beta_s + \tilde{t}_{r_2}\sin\beta_r)\right], \quad (2.4)$$

$$z_\xi = V_1(t_{s_1}\cos\alpha_s + \rho\tilde{t}_{s_2}\cos\beta_s) = V_1(t_{r_1}\cos\alpha_r + \rho\tilde{t}_{r_2}\cos\beta_r), \quad (2.5)$$

$$m_\xi = \frac{x_{r_\xi} + x_{s_\xi}}{2} = m_D + \frac{V_1}{2}\left(t_{s_1}\sin\alpha_s - t_{r_1}\sin\alpha_r + \rho(\tilde{t}_{s_2}\sin\beta_s - \tilde{t}_{r_2}\sin\beta_r)\right), \quad (2.6)$$

The traveltime of the refracted ray segments $\tilde{t}_{s_2}$ and $\tilde{t}_{r_2}$ can be computed from the two imaging conditions: (1) at the image point the depth of both rays has to be the same (since we are computing horizontal subsurface offset gathers) and (2) $t_{s_2} + t_{r_2} = \tilde{t}_{s_2} + \tilde{t}_{r_2}$ which follows immediately from equation 2.1 since at the image point the total extrapolated time equals the traveltime of the multiple. As shown in Appendix A, the traveltimes of the refracted rays are

given by

$$\tilde{t}_{s_2} = \frac{t_{r_1}\cos\alpha_r - t_{s_1}\cos\alpha_s + \rho(t_{s_2}+t_{r_2})\cos\beta_r}{\rho(\cos\beta_s+\cos\beta_r)}, \tag{2.7}$$

$$\tilde{t}_{r_2} = \frac{t_{s_1}\cos\alpha_s - t_{r_1}\cos\alpha_r + \rho(t_{s_2}+t_{r_2})\cos\beta_s}{\rho(\cos\beta_s+\cos\beta_r)}. \tag{2.8}$$

The refracted angles are related to the takeoff angles by Snell's law: $\sin(\beta_s+\varphi)=\rho\sin(\alpha_s+\varphi)$ and $\sin(\beta_r-\varphi)=\rho\sin(\alpha_r-\varphi)$, from which we get

$$\sin\beta_s = \rho\sin(\alpha_s+\varphi)\cos\varphi - \sqrt{1-\rho^2\sin^2(\alpha_s+\varphi)}\sin\varphi, \tag{2.9}$$

$$\sin\beta_r = \rho\sin(\alpha_r-\varphi)\cos\varphi + \sqrt{1-\rho^2\sin^2(\alpha_r-\varphi)}\sin\varphi, \tag{2.10}$$

$$\cos\beta_s = \sqrt{1-\rho^2\sin^2(\alpha_s+\varphi)}\cos\varphi + \rho\sin(\alpha_s+\varphi)\sin\varphi, \tag{2.11}$$

$$\cos\beta_r = \sqrt{1-\rho^2\sin^2(\alpha_r-\varphi)}\cos\varphi - \rho\sin(\alpha_r-\varphi)\sin\varphi. \tag{2.12}$$

In ADCIGs, the mapping of the multiples can be directly related to the previous equations by the geometry shown in Figure 2.2. The half-aperture angle is given by

$$\gamma = \frac{\beta_r+\beta_s}{2}, \tag{2.13}$$

which is the same equation derived for converted waves by Rosales and Biondi (2005). The depth of the image point in ADCIGs ($z_{\xi_\gamma}$) is given by (Appendix B)

$$z_{\xi_\gamma} = z_\xi - h_\xi\tan\gamma. \tag{2.14}$$

Equations 2.4–2.6 describe the transformation performed by wave-equation migration between CMP gathers $(m_D, h_D, t)$ and SODCIGs $(m_\xi, h_\xi, z_\xi)$. Equations 2.7–2.12 relate the traveltimes and angles of the refracted segments to parameters that can in principle be computed from the data (traveltimes, takeoff angles, reflector dips and velocities). Equations 2.13 and 2.14 provide the transformation from SODCIGs to ADCIGs. These equations are valid for any first-order water-bottom multiple, whether from a flat or dipping water-bottom. They even describe the migration of source- or receiver-side diffracted multiples with the diffractor at

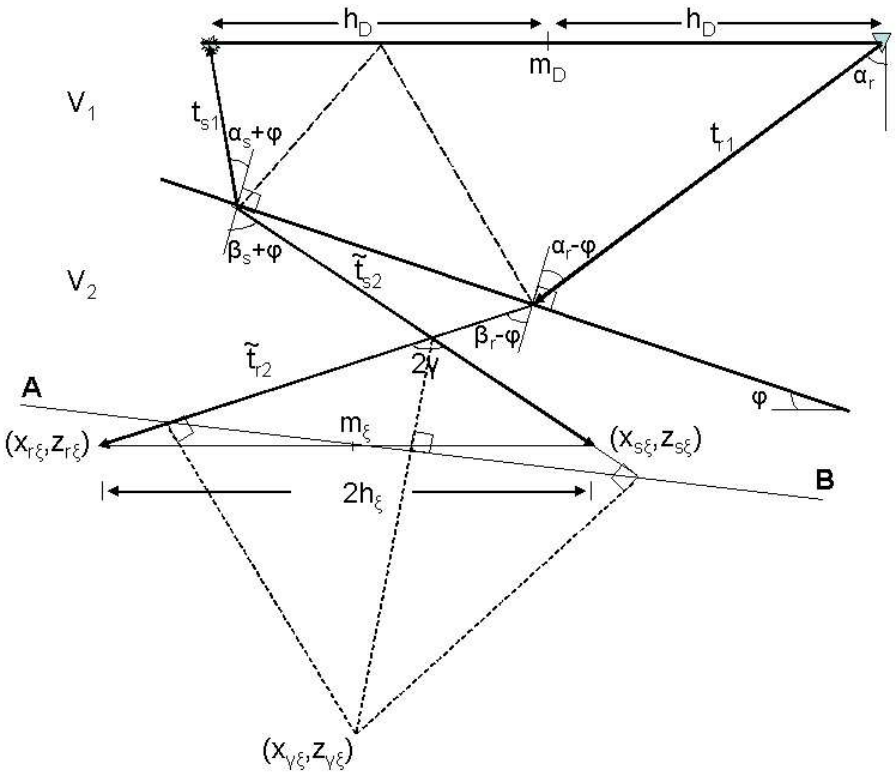


Figure 2.2: Imaging of water-bottom multiple in SODCIG and ADCIG. The subscript $D$ refers to the data space while the subscript $\xi$ refers to the image space. The points $(x_{r\xi}, z_{r\xi})$ and $(x_{s\xi}, z_{s\xi})$ represent the end points of the source and receiver ray after migration and must be at the same depth at the image point (for horizontal ADCIGs). The coordinates $(m_\xi, \gamma_\xi, z_{\gamma\xi})$ correspond to the image point in the angle domain. The coordinates $(m_\xi, h_\xi, z_{r\xi})$ correspond to the image point in the subsurface offset gather. The line AB represents the apparent reflector at the image point. 2d-mul_sktch3 [NR]

the water bottom, since no assumption has been made relating $\alpha_r$ and $\alpha_s$ or the individual traveltime segments. These equations, however, are of little practical use unless we can relate the individual traveltime segments ($t_{s_1}$, $t_{s_2}$, $t_{r_2}$, $t_{r_1}$), and the angles $\alpha_s$ and $\alpha_r$ to the known data space coordinates ($m_D$, $h_D$, $t_m$) and the model parameters ($V_1$, $\varphi$ and $\rho$). This may not be easy or even possible analytically for all situations, but it is for the simple but important case of a specular multiple from a flat water-bottom.

**Specular multiple from flat water-bottom**

The traveltime of the first-order water-bottom multiple is given by

$$t_m = \frac{4}{V_1}\sqrt{\left(\frac{h_D}{2}\right)^2 + Z_{wb}^2} = \sqrt{t_m^2(0) + \left(\frac{2h_D}{V_1}\right)^2}, \tag{2.15}$$

which is simply the traveltime of a primary at twice the depth of the water-bottom $Z_{wb} = \frac{V_1 t_m(0)}{4}$.

From the symmetry of the problem, $t_{s_1} = t_{s_2} = t_{r_1} = t_{r_2} = t_m/4$ and $\alpha_s = \alpha_r$, which in turn means $\beta_s = \beta_r$. Furthermore, from Equations 2.7 and 2.8 it immediately follows that $\tilde{t}_{s_2} = t_{s_2}$ and $\tilde{t}_{r_2} = t_{r_2}$ which says that the traveltimes of the refracted rays are equal to the traveltimes of the corresponding segments of the multiple. Equation 2.4 thus simplifies to

$$h_\xi = \frac{h_D}{2}(1-\rho^2), \tag{2.16}$$

which indicates that the subsurface offset at the image point of a trace with half surface offset $h_D$ depends only on the velocity contrast between the water and the sediments. In particular, if the trace is migrated with the water velocity, *i.e.* $\rho = 1$, then $h_\xi = 0$ which proves the property that the multiple is imaged exactly as a primary. It should also be noted that, since usually sediment velocity is faster than water velocity, then $\rho^2 > 1$ and therefore the multiples are mapped to subsurface offsets with the opposite sign to that of the surface offset $h_D$ when migrated with sediment velocity.

From Equation 2.5, the depth of the image point can be easily computed as

$$z_\xi = Z_{wb} + \frac{\rho}{2}\sqrt{h_D^2(1-\rho^2)+4Z_{wb}^2}, \tag{2.17}$$

which for migration with the water velocity reduces to $z_\xi = 2Z_{wb}$, showing that the multiple is migrated as a primary at twice the water depth as is intuitively obvious. Finally, from Equation 2.6, the horizontal position of the image point reduces to

$$m_\xi = m_D. \tag{2.18}$$

This result shows that the multiple is mapped in the image space to the same horizontal position as the corresponding CMP even if migrated with sediment velocity. This result is a direct consequence of the symmetry of the raypaths of the multiple reflection in this case. For dipping water bottom or for diffracted multiples this is not the case (Alvarez, 2005).

Equations 2.16–2.18 give the image space coordinates in terms of the data space coordinates. An important issue is the functional relationship between the subsurface offset and the image depth, since it determines the moveout of the multiples in the subsurface-offset-domain common-image-gathers (SODCIGs). Replacing $h_D = 2h_\xi/(1-\rho^2)$ and $Z_{wb} = z_\xi(0)/(1+\rho)$ in Equation 2.17 we get

$$z_\xi = \frac{z_\xi(0)}{1+\rho} + \rho\sqrt{\left(\frac{z_\xi(0)}{1+\rho}\right)^2 + \frac{h_\xi^2}{1-\rho^2}} \qquad (\rho \neq 1) \tag{2.19}$$

which shows that the moveout is a hyperbola (actually, for off-end geometry, half of a hyperbola, since we already established that $h_\xi \leq 0$ if $h_D \geq 0$).

Figure 2.3 shows an SODCIG for a specular water-bottom multiple from a flat water-bottom 500 m deep. The data was migrated with a two-layer velocity model: the water layer of 1500 m/s and a sediment layer of velocity 2500 m/s. Larger subsurface offsets (which according to Equation 2.16 correspond to larger surface offsets) map to shallower depths for the usual situation of $\rho > 1$, as we should expect since the rays are refracted to increasingly larger angles until the critical reflection angle is reached. Also notice that the hyperbola is shifted down by a factor $(1+\rho)$ with respect to its image point when migrated with water

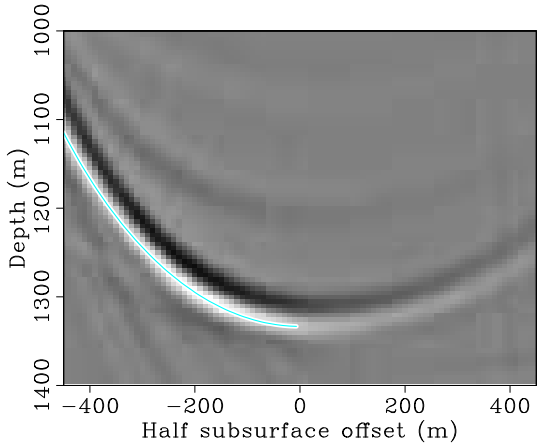


Figure 2.3: Subsurface offset domain common image gather of a water-bottom multiple from a flat water-bottom. Water velocity is 1500 m/s, water depth 500 m, sediment velocity 2500 m/s and surface offsets from 0 to 2000 m. Overlaid is the residual moveout curve computed with Equation 2.19. 2d-odcig1 [CR]

velocity.

In angle-domain common-image-gathers (ADCIGs), the half-aperture angle reduces to $\gamma = \beta_s = \beta_r$, which in terms of the data space coordinates is given by

$$\gamma = \sin^{-1}\left[\frac{2\rho h_D}{V_1 t_m}\right]. \tag{2.20}$$

The depth of the image can be easily computed from Equation 2.14. In particular, if the data are migrated with the velocity of the water, then $\rho = 1$, and therefore $z_{\xi\gamma} = 2Z_{wb}$, which means a horizontal line in the $(z_{\xi_\gamma}, \gamma)$ plane at twice the depth of the water-bottom. Equivalently, we can say that the residual moveout in the $(z_{\xi_\gamma}, \gamma)$ plane is zero, once again corroborating that the water-bottom multiple is migrated as a primary if $\rho = 1$. Equation 2.14 can be expressed in terms of the data space coordinates using Equations 2.16 and 2.17 and noting that

$$\tan\gamma = \tan\beta_s = \frac{\rho\sin\alpha_s}{\sqrt{1-\rho^2\sin^2\alpha_s}} = \frac{\rho h_D}{\sqrt{4Z_{wb}^2 + h_D^2(1-\rho^2)}} \tag{2.21}$$

If $\rho = 1$ this expression simplifies to $\tan\gamma = \frac{h_D}{2Z_{wb}}$, which is the aperture angle of a primary at twice the water-bottom depth.

As I did with the SODCIG, it is important to find the functional relationship between $z_{\xi_\gamma}$ and $\gamma$ since it dictates the residual moveout of the multiple in the ADCIG. Plugging Equations 2.16 and 2.17 into equation 2.14, using Equations 2.15, and 2.20 to eliminate $h_D$ and

simplifying we get

$$z_{\xi_\gamma} = Z_{wb}\left[1+\frac{\cos\gamma(\rho^2-\tan^2\gamma(1-\rho^2))}{\sqrt{\rho^2-\sin^2\gamma}}\right] \tag{2.22}$$

$$= \frac{z_{\xi_\gamma}(0)}{1+\rho}\left[1+\frac{\cos\gamma(\rho^2-\tan^2\gamma(1-\rho^2))}{\sqrt{\rho^2-\sin^2\gamma}}\right]. \tag{2.23}$$

Once again, when the multiple is migrated with the water velocity ($\rho = 1$) we get the expected result $z_{\xi_\gamma} = z_{\xi_\gamma}(0)$, that is, flat moveout (no angular dependence). The residual moveout in ADCIGs is therefore given by

$$\Delta n_{\mathrm{RMO}} = z_{\xi_\gamma}(0) - z_{\xi_\gamma} = \left[\rho - \frac{\cos\gamma(\rho^2-(1-\rho^2)\tan^2\gamma)}{\sqrt{\rho^2-\sin^2\gamma}}\right]\frac{z_0}{1+\rho}. \tag{2.24}$$

This equation reduces to that of Biondi and Symes (2004) when $\gamma$ is small (Appendix C), which is when we can neglect ray bending at the multiple-generating interface. Panel (a) of Figure 2.4 shows the ADCIG corresponding to the SODCIG shown in Figure 2.3. Notice that the migrated depth at zero aperture angle is the same as that for the zero sub-surface offset in Figure 2.3. For larger aperture angles, however, the migrated depth increases as indicated in equation 2.23. The continuous line corresponds to Equation 2.24 whereas the dotted line corresponds to the tangent-squared of Biondi and Symes (2004). For this model, the departure of the straight ray approximation can be more than 5% for large aperture angles as illustrated in panel (b). The relative error represents the different between the two approximations divided by that the more accurate of equation 2.24.

**Specular multiple from dipping water-bottom**

I presented the particular case of flat water bottom case in some detail because it lends itself to the nice closed-form equation for the residual moveout of the multiples in ADCIGs. This equations is the basis for the design of the Radon transform to attenuated the multiples. The specular multiple from a dipping water-bottom has similar characteristics although the

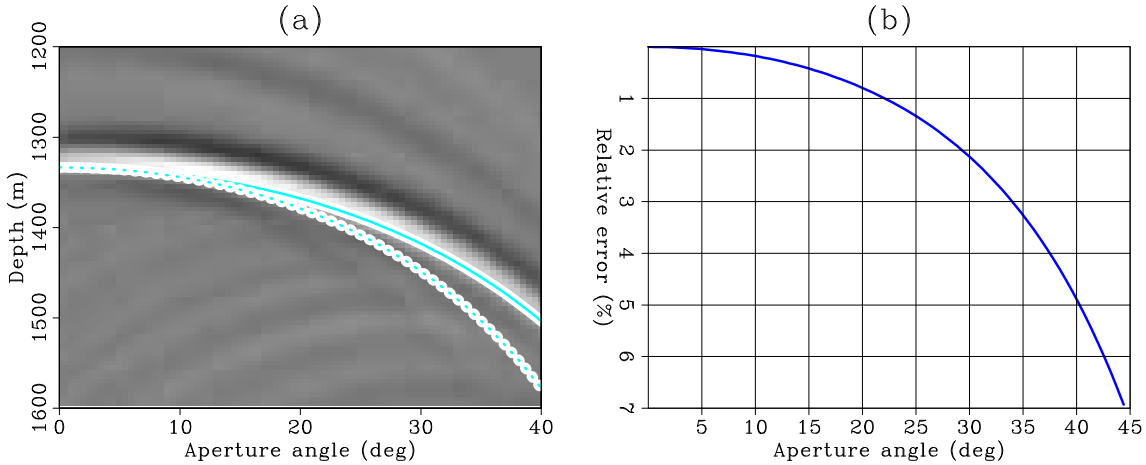


Figure 2.4: Panel (a) is an ADCIG for a water-bottom multiple from a two flat-layer model. The dotted curve corresponds to the straight ray approximation whereas the solid curve corresponds to the ray-bending approximation. Panel (b) is the relative error between the two approximations. 2d-adcig1 [CR]

moveout equations are more involved (Alvarez, 2005) and will not be given here. Instead, I show in Figure 2.5 the zero subsurface offset section, an SODCIG and its corresponding ADCIG. The lines superimposed are the moveout curves computed with the equations in Alvarez (2005). The zero subsurface-offset section corresponds to a reflector with twice the dip of the water-bottom. The ADCIG has its apex at zero aperture angle.

**Diffracted multiple**

The diffracted multiple has very different characteristics compared to the specular multiple. The residual moveout equations are very involved and were presented in Alvarez (2005). Figure 2.6 is a summary of the mapping of this multiple to image space for a diffracted multiple sitting on a dipping water-bottom. The top three panels correspond to subsurface offset sections taken at 0, -200 and 200 m (panels (a) to (c) respectively). Notice that the moveout of the multiples looks like migration "smiles" which is one of the tell-tale indications of diffracted multiples on a migrated angle stack. The middle panels in Figure 2.6 correspond to SODCIGs taken at lateral positions 1800, 2000 and 2200 m. The diffractor is located at 2000 m and the

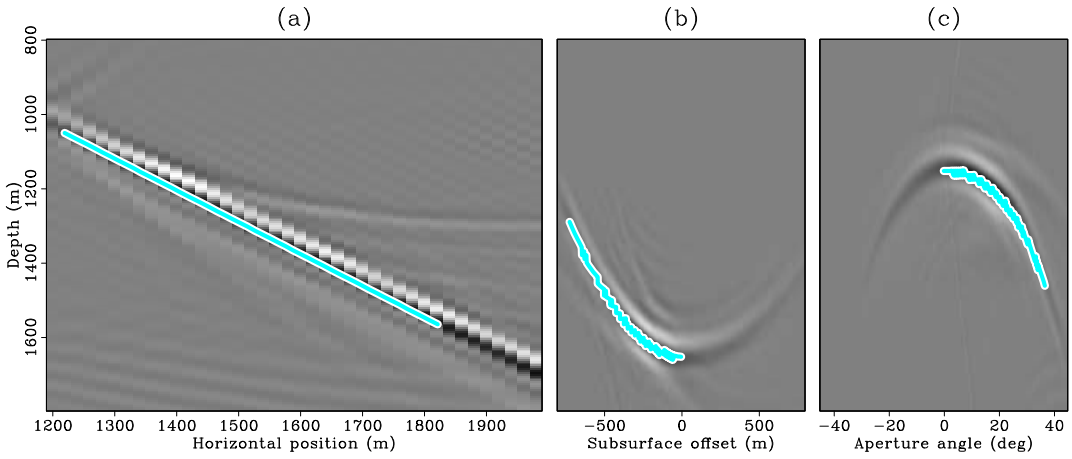


Figure 2.5: Specular multiple from dipping water-bottom. Panel (a) is the zero subsurface-offset section. Panel (b) is an ODCIG and panel (c) is its corresponding ADCIG. The solid lines are the moveout curves computed with the equations given by Alvarez (2005). 2d-wb_dip_moveout [CR]

offsets are positive towards increasing lateral positions. This causes the bottom of the move-out curve to shift away from zero as the SODCIG is taken away from then location of the diffractor (compare panels (b) and (c), for example). Panel (b) corresponds to the location of the diffractor and therefore its bottom is at zero subsurface offset. Finally, the bottom panels are the ADCIGs of the corresponding SODCIGs in the middle panels. Notice that again, the apex of the moveout curve moves away from zero aperture angle as the ADCIG is taken at locations not directly above the diffractor. In all the figures the solid lines are the moveout curves computed with the equations in Alvarez (2005).

## RADON TRANSFORM

In this section I show how to exploit the difference in residual moveout between primaries and multiples in ADCIG's given by Equation 2.24 to design a Radon transform that focuses the primaries and multiples to separate regions of the Radon domain. The general expression for

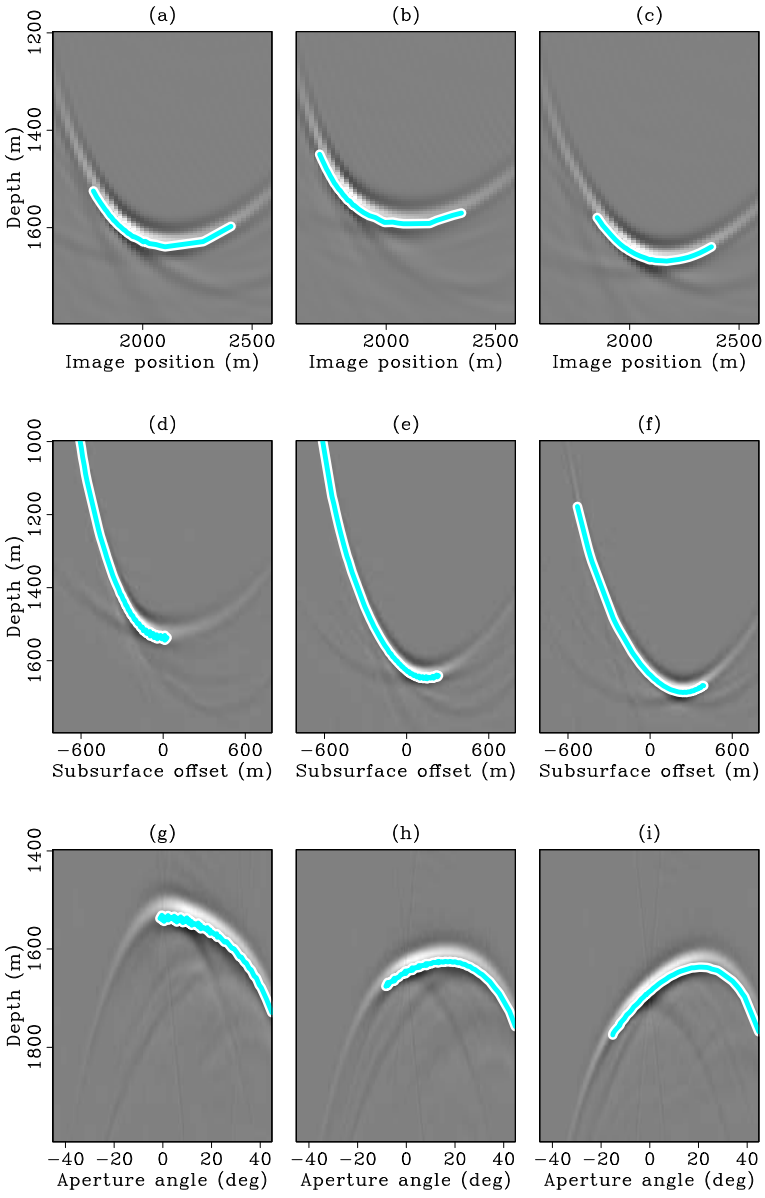


Figure 2.6: Diffracted multiple from dipping water-bottom. Top panels are subsurface offset sections taken at 0, -200 and 200 m (from (a) to (c)). The middle panels are SODCIGs taken at 1800, 2000 and 2200 m horizontal location (panels (d) to (f)). The diffractor is at 2000 m. Bottom panels are the ADCIGs corresponding to the SODCIGs of the middle panels. The solid lines are the moveout curves computed with the equations given by Alvarez (2005). 2d-diffmul_dip_moveout [CR]

the Radon transform in the angle domain is (Sava and Guitton, 2003)

$$z(q,\gamma) = z_0 + q\ g(\gamma). \tag{2.25}$$

where $q$ is a measure of curvature and $g(\gamma)$ is the function that approximates the residual moveout of the multiples as a function of the aperture angle $\gamma$. Sava and Guitton (2005) and Alvarez et. al. (2004) used the tangent-squared approximation of Biondi and Symes (2004)

$$g(\gamma) = \tan^2\gamma, \tag{2.26}$$

but for the focusing of the multiples a more accurate approximation is given by Equation 2.24:

$$g(\gamma) = \frac{1}{1+\rho}\left[\frac{\cos\gamma(\rho^2-(1-\rho^2)\tan^2\gamma)}{\sqrt{\rho^2-\sin^2\gamma}} - \rho\right]. \tag{2.27}$$

This approximation is more accurate because it takes into account ray bending at the multiple-generating interface. This is illustrated in Figure 2.7 which shows a comparison of the Radon transforms defined be equations 2.27 and 2.26 applied to a synthetic ADCIG. Notice that the focusing of the primaries does not change since their moveout is zero. The multiples, on the other hand, are better focused with the new transform (panel (c)) which more closely follows their residual moveout in the ADCIGs. The better focusing of the multiples translates to a better estimation of the multiple model (compare panels (d) and (e) computed from panels (b) and (c), respectively). Notice, however, that this synthetic ADCIG has high aperture angles for which the difference between the two approximations is greater. As the angle coverage decreases, so does this difference. In any event, the better focusing of the multiples helps in separating them from the primaries.

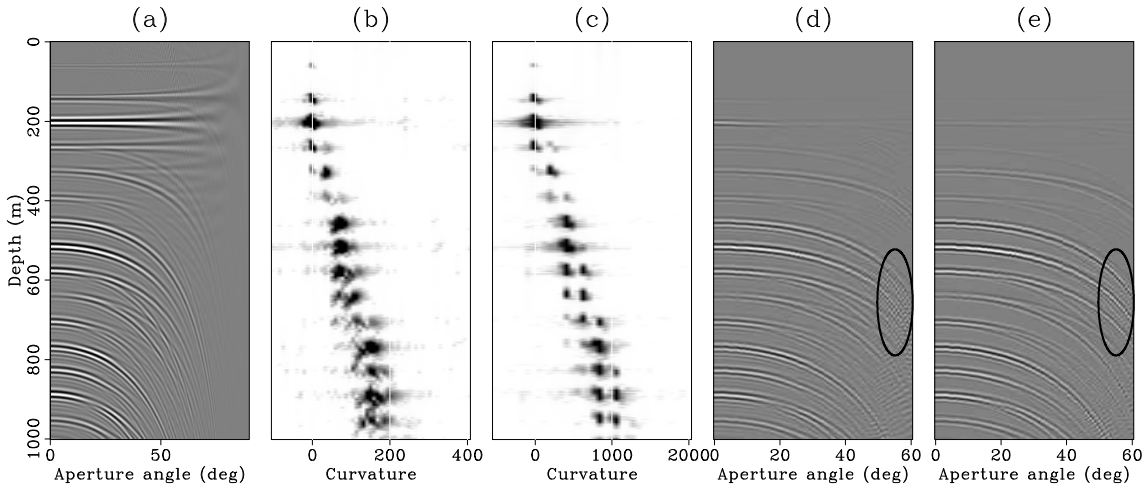


Figure 2.7: Comparison of Radon transforms for a synthetic ADCIG. Panel (a) shows the ADCIG. Panels (b) and (c) correspond to the envelopes of the Radon transform of panel (a) computed with the straight-ray approximation and the ray-bending approximation respectively. Panels (d) and (e) are the multiple models computed from panels (b) and (c). The ovals highlight the improved accuracy afforded by the new transform for the multiple model at the large aperture angles. 2d-synth1 [CR]

### Apex-shifted Radon Transform

The apex of the residual moveout curve of the diffracted multiples in ADCIGs is shifted away from zero aperture angle. Therefore, to attenuate the diffracted multiples, I define the transformation from ADCIGs to model space (Radon-transformed domain) as:

$$m(\Gamma, q, z') = \sum_{\gamma} d(\gamma, z = z' + qg(\gamma - \Gamma)), \tag{2.28}$$

and from model space to data space as

$$d(\gamma, z) = \sum_{q} \sum_{\Gamma} m(\Gamma, q, z' = z - qg(\gamma - \Gamma)), \tag{2.29}$$

where $g(\gamma)$ is given by Equation 2.27 and $\Gamma$ is the lateral apex shift (in units of aperture angle). In this way, I transform the two-dimensional data space of ADCIGs, $d(\gamma, z)$, into a three-dimensional model space, $m(\Gamma, q, z')$.

In the ideal case of migration with the correct velocity, primaries would be perfectly horizontal in the ADCIGs and would thus map in the model space to the zero-curvature ($q = 0$) plane, *i.e.*, a plane of dimensions depth and apex-shift distance ($\Gamma, z'$). Specular multiples would map to the zero apex-shift distance ($\Gamma = 0$) plane, *i.e.*, a plane of dimensions depth and curvature ($q, z'$). Diffracted multiples would map elsewhere in the cube depending on their curvature and apex-shift distance.

### Sparsity Constraint

In order to minimize the number of model space parameters necessary to represent the data in the Radon domain, I implemented the transform given by equations 2.28 and 2.29, with the Radon kernel given by equation 2.27 as a least squares problem with a sparsity constraint. As a linear transformation, the apex-shifted Radon transform can be represented simply as

$$\mathbf{d} = \mathbf{L}\mathbf{m}, \tag{2.30}$$

where $\mathbf{d}$ is the (migrated) data in the angle domain, $\mathbf{m}$ is the model in the Radon domain and $\mathbf{L}$ is the forward apex-shifted Radon transform operator. To find the model $\mathbf{m}$ that best fits the data in a least-squares sense, I minimize the objective function:

$$f(\mathbf{m}) = \|\mathbf{L}\mathbf{m} - \mathbf{d}\|^2 + \epsilon^2 b^2 \sum_{i=1}^{n} \ln\left(1 + \frac{m_i^2}{b^2}\right), \tag{2.31}$$

where the second term is a Cauchy regularization (Guitton and Symes, 2003) that enforces sparseness in the model space. Here $n$ is the size of the model space, and $\epsilon$ and $b$ are two constants chosen a-priori: $\epsilon$ which controls the amount of sparseness in the model space and $b$ which controls the minimum value below which everything in the Radon domain should be zeroed. The least-squares inverse of $\mathbf{m}$ is given by

$$\hat{\mathbf{m}} = \left[\mathbf{L}'\mathbf{L} + \epsilon^2 \mathbf{Q}\right]^{-1} \mathbf{L}'\mathbf{d}, \tag{2.32}$$

where **Q** is a diagonal matrix whose elements are given by (Sacchi and Ulrych, 1995):

$$\left(1+\frac{m_i^2}{b^2}\right)^{-1}. \tag{2.33}$$

Because the model space can be large, I estimate **m** iteratively. Notice that the objective function in equation (2.31) is non-linear because the model appears in the definition of the regularization term. Therefore, I use a limited-memory quasi-Newton method (Guitton and Symes, 2003) to find the minimum of $f(\mathbf{m})$.

## SYNTHETIC DATA EXAMPLE

In this section I introduce a simple 2D synthetic example to illustrate the mapping of a water-bottom and a diffracted multiple from data space to image space. Figure 2.8 shows the velocity model as well as the raypath of the primaries and multiples that were modeled. Figure 2.9 shows the zero offset section and the CMP gather at CMP position 2400 m. The depth of the deep reflector was chosen so that the multiples and the deep primary came at about the same zero-offset time and were imaged at about the same depth. Notice that the apex of the moveout curve of the diffracted multiple is not at zero offset. Moreover, the moveout curve is not well represented by a hyperbola. Therefore, we cannot attenuate the diffracted multiple via a standard data-space Radon transform.

After prestack wave-equation migration, the primaries are well focused at zero subsurface offset as shown in Figure 2.10. Panel (a) is the zero-subsurface offset section whereas panel (b) is the SODCIG taken at CMP location 3800 m. The water-bottom multiple is mapped to the negative subsurface offsets while the diffracted multiple is mapped to both positive and negative subsurface offsets. Notice that in the zero subsurface offset (panel (a)) the water-bottom multiple and the deep primary are imaged at about the same depth. After transformation to ADCIGs, the primaries are now flat whereas the multiples shows the expected over-migrated residual moveout (panel (a) of Figure 2.11). The apex of the diffracted multiple, however, is not at zero aperture angle. Panel (b) of Figure 2.11 shows the Radon plane taken at zero apex shift while panel (c) shows the Radon plane taken at the apex-shift of the multiple (14

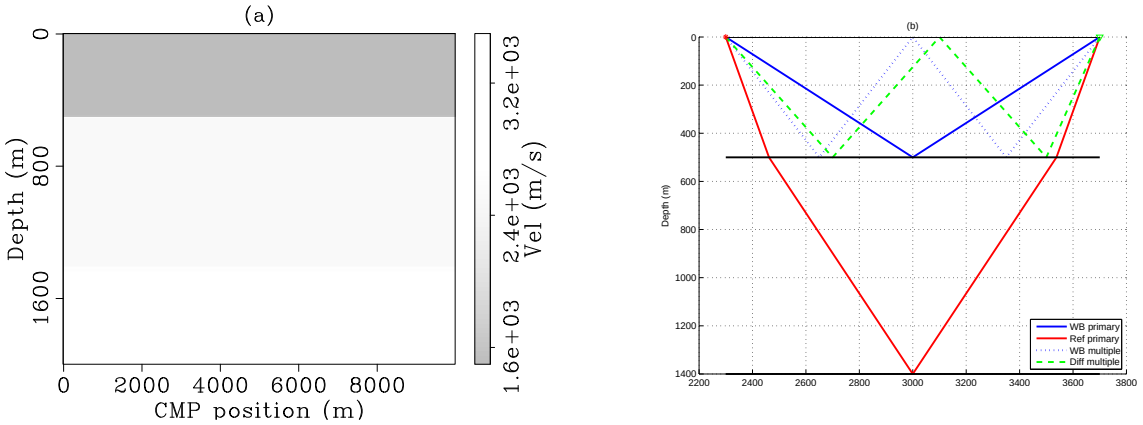


Figure 2.8: Synthetic model. Panel (a): velocity model. Panel (b): raypaths of modeled primaries and multiples. 2d-synth_vels [ER]

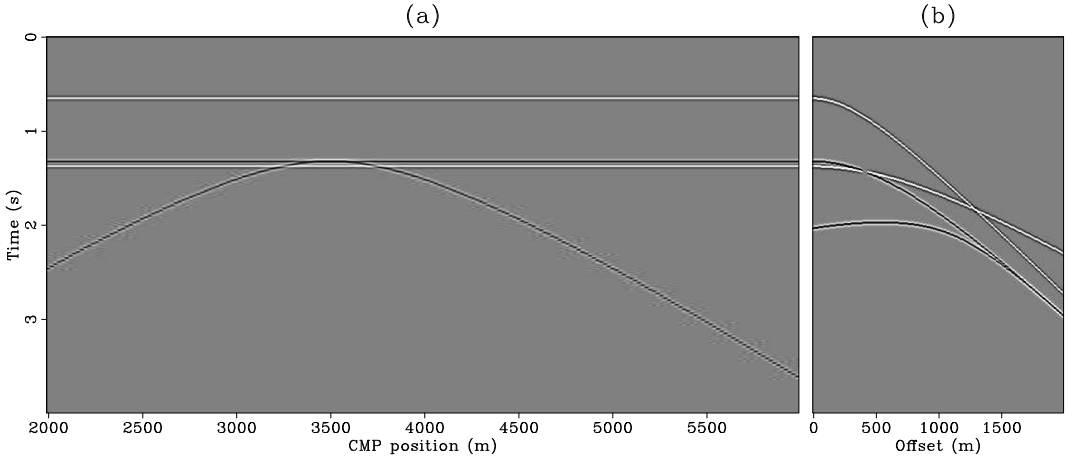


Figure 2.9: Synthetic data: Panel (a): zero-offset section. Panel (b): CMP gather at CMP location 2400 m. 2d-synth_cmps [CR]

degrees). Notice that both the primaries and the water-bottom multiple are well focused in the zero apex-shift plane whereas the diffracted multiple is well focused at its apex-shift plane.

For the sake of comparison, I also applied the non apex-shifted transform to the data and eliminated the primaries with the same mute pattern. After inverse Radon transforming the multiples and subtracting them from the original ADCIG I got the results shown in Figure 2.12. Panel (a) is the original ADCIG. Panel (b) shows the estimated multiples with the apex-shifted transform and panel (c) shows the multiples estimated with the standard transform. The apex-shifted transform was able to recover the diffracted multiple while the standard transform mistook it for a specular multiple and thus produced the wrong multiple moveout. Notice that some primary energy leaked into the estimate of the multiples in panel (b). Figure 2.13 shows the estimated primaries. Panel (a) is the original ADCIG, panel (b) is the difference between panels (a) and (b) in Figure 2.10 and therefore is an estimate of the primaries obtained with the apex-shifted transform. Panel (c) is the corresponding estimate with the standard transform. Some residual multiple energy remains above the deep primary in panel (b) but the primary was recovered. The estimation of the primaries could be improved by adaptively matching the estimated multiples to the multiples in the data (as in SRME), before the subtraction. Finally, panel (c) shows that the poor estimate of the diffracted multiple with the standard transform causes it to leak almost unattenuated into the estimate of the primaries.

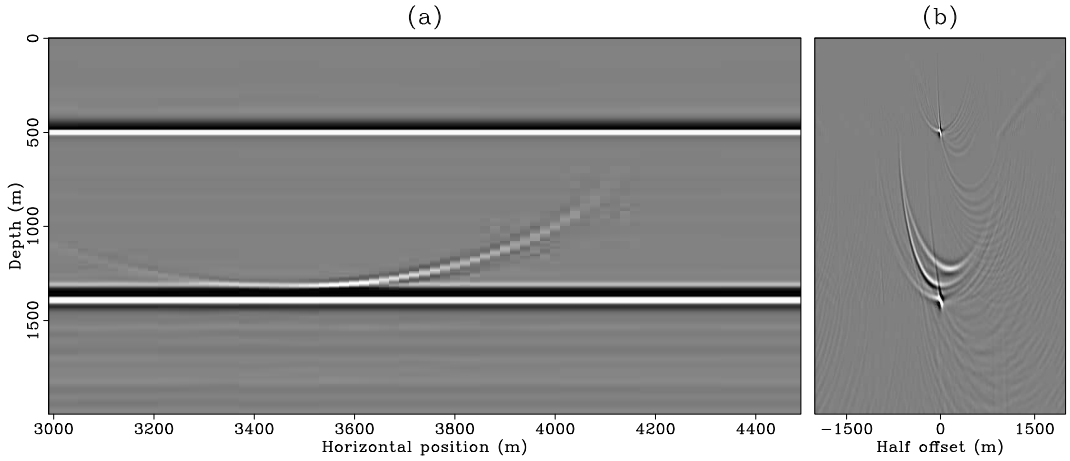


Figure 2.10: Zero-subsurface offset image (a) and SODCIG at surface location 3800 m (b). Notice the residual moveout of the diffracted multiple being mapped to both positive and negative offsets. 2d-mig_cmps [CR]

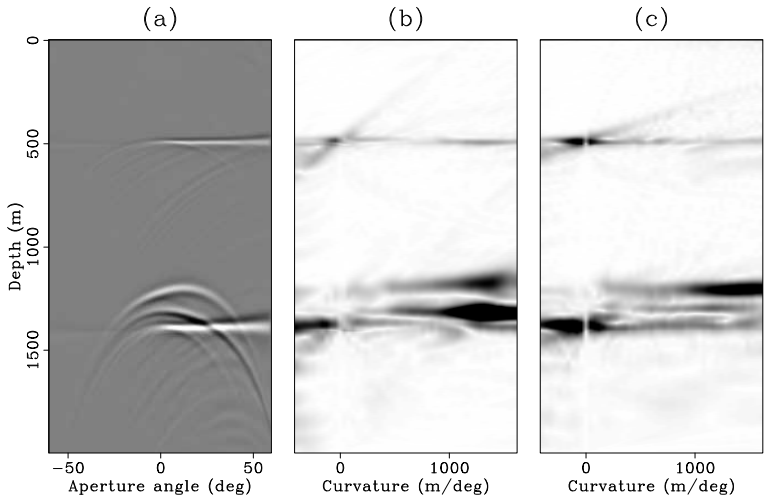


Figure 2.11: (a): ADCIG of the same SODCIG in panel (b) of Figure 2.10; (b): plane taken from the apex-shifted Radon cube at $\Gamma = 0$; (c): plane taken from the apex-shifted Radon cube at $\Gamma = 10$ degrees. 2d-mig_adcig [CR]

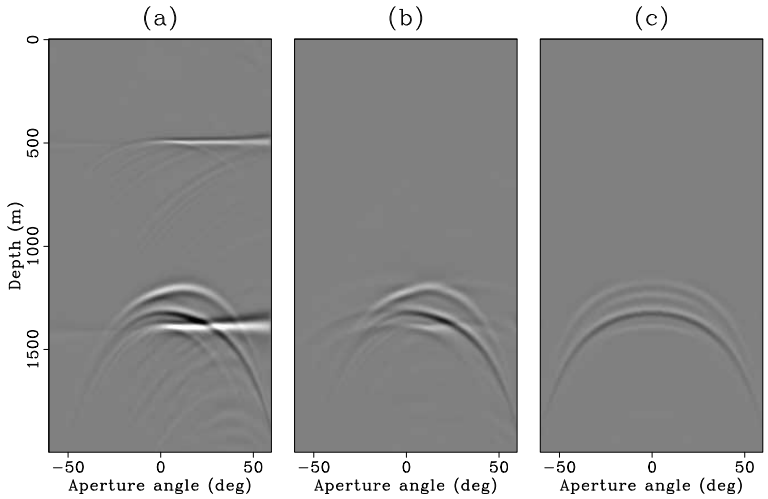


Figure 2.12: (a): original ADCIG; (b): estimated multiples with the apex-shifted transform; (c): estimated multiples with the standard transform. 2d-mig_muls [CR]

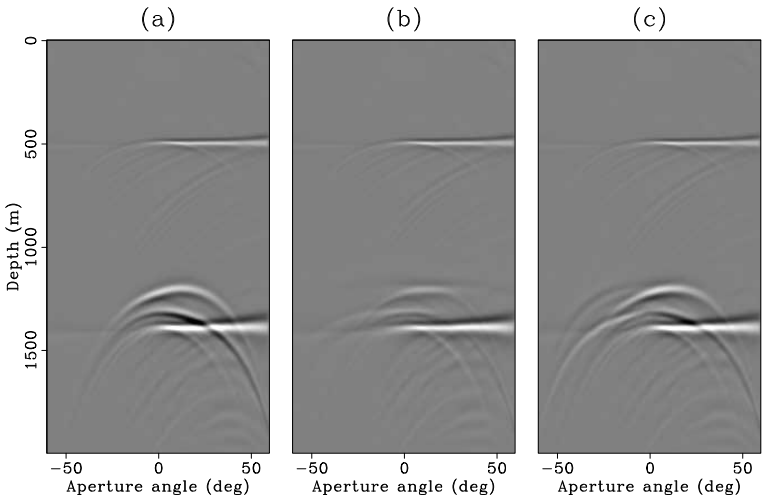


Figure 2.13: (a): original ADCIG; (b): estimated primaries with the apex-shifted transform; (c): estimated primaries with the standard transform. 2d-mig_prims [CR]

## GULF OF MEXICO 2D SEISMIC LINE

In this section I introduce the seismic line I use to test the apex-shifted Radon transform. The line is from the Gulf of Mexico and was shot over a large salt body. The presence of the salt creates a host of multiples that obscure any genuine subsalt reflections, as shown in the angle stack of Figure 2.14. Most multiples are surface-related peg-legs with a leg related to the water bottom, shallow reflectors or the top of salt. Below the edges of the salt we also encounter diffracted multiples (*e.g.*, CMP position 6000 m below 4000 m depth in Figure 2.14).

Figure 2.15 shows four ADCIGs obtained with wave-equation migration as described by Sava and Fomel (2003). Notice that although the data is marine, the ADCIGs show positive and negative aperture angles. I used reciprocity to simulate negative offsets and interpolation to compute the two shortest-offset traces not present in the original data. The CMP gathers were then migrated and converted to angle gathers. The purpose of having both positive and negative aperture angles is to see more clearly the position of the apexes of the diffracted multiples. The top two ADCIGs correspond to lateral positions directly below the edges of the salt body (CMP positions 6744 m and 22056 m in Figure 2.14). Notice how the apexes of the diffracted multiples are shifted away from zero aperture angle (*e.g.*, the seagull-looking event

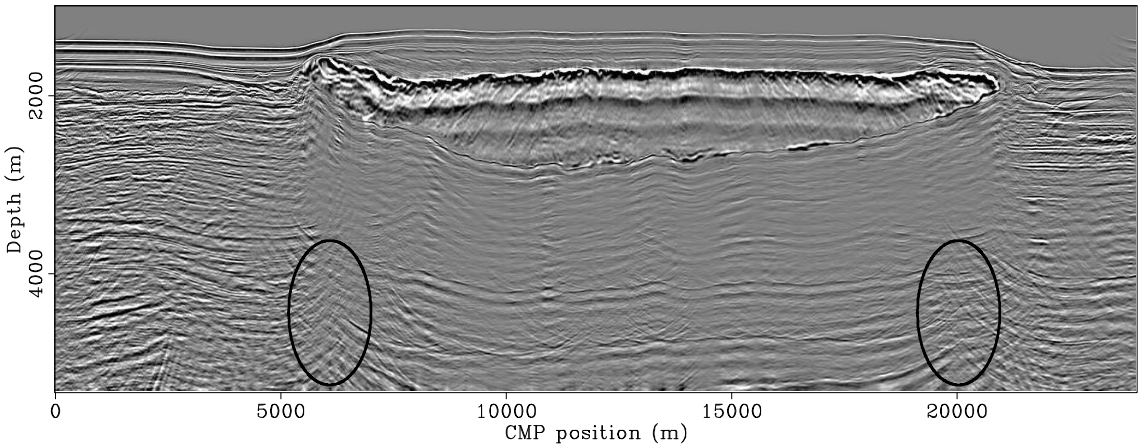


Figure 2.14: Angle stack of migrated ADCIGs of 2D seismic line in the Gulf of Mexico. Notice that multiples below the salt obscure any primary reflections. The ovals highlight diffracted multiples. 2d-angle_stack [CR]

at about 4600 m in panel (a)). For comparison, the bottom panels in Figure 2.15 show two ADCIGs that do not have diffracted multiples. Figure 2.15(c) corresponds to an ADCIG below the sedimentary section (CMP 3040 m in Figure 2.14) and Figure 2.15(d) to an ADCIG below the salt body (CMP position 12000 m in Figure 2.14). In these ADCIGs all the multiples are specularly-reflected and thus have their apexes at zero aperture angle.

## MAPPING TO THE RADON DOMAIN

With ideal data, attenuating both specular and diffracted multiples could, in principle, be accomplished simply by zeroing out (with a suitable taper) all the $q$-planes except $q = 0$ in the model cube $m(z', q, \Gamma)$ and taking the inverse apex-shifted Radon transform. In practice, however, the primaries may not be well-corrected and primary energy may map to a other nearby $q$-planes. Energy from the multiples may also map to those planes and so we have the usual trade-off of primary preservation versus multiple attenuation. The advantage of the apex-shift transform is that the diffracted multiples are well focused to their corresponding $\Gamma$-planes instead of being mapped as unfocused noise that interferes with the primaries.

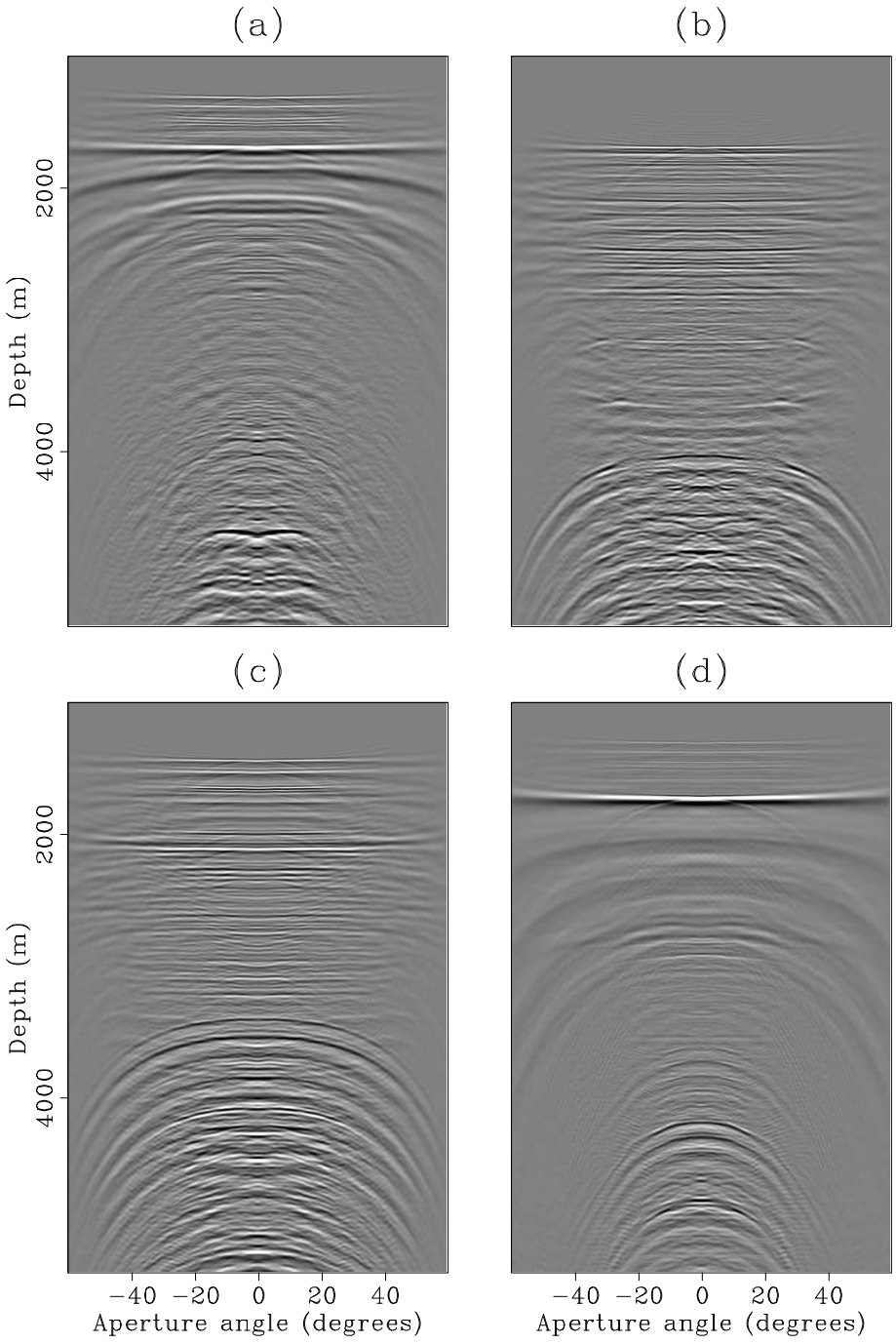


Figure 2.15: Angle domain common image gathers. (a) under the left edge of the salt, CMP at 6744 m; (b) under the right edge of the salt, CMP at 22056 m; (c) below the sedimentary section, CMP at 3040; (d) below the salt body, CMP at 12000 m. 2d-cags [CR]

To illustrate the mapping of the primaries, the specular multiples and the diffracted multiples, between the image space $(z, \gamma)$ and the apex-shifted Radon space $(z', q, \Gamma)$, I chose the ADCIG in Figure 2.15(a). Although this ADCIG shows no discernible primaries below the salt, it nicely shows the apex-shifted moveout of the diffracted multiples. This ADCIG was transformed to the Radon domain with the apex-shifted transform described by equations 2.28 and 2.29. The kernel of the Radon transform is given by equation 2.27 and I applied the Cauchy regularization given in equation 2.31. Figure 2.16 shows envelopes of the data in the Radon domain. Panel (a) shows the $\Gamma = 0$ plane from the $(z', q, \Gamma)$ volume. This plane corresponds to zero apex-shift and therefore this is where the majority of the specular multiples should map. Figure 2.16(b) shows the zero-curvature $q = 0$ plane, that is, the plane where the primaries should map. Notice that since the primaries are flat, they are independent of the apex-shift $\Gamma$ and therefore map as flat lines on this plane. Notice also that there are no significant primaries on the ADCIG below 2000 m. For comparison, Figure 2.16(c) shows the $\Gamma = 8$ deg plane. This corresponds to the apex-shift of the most obvious diffracted multiple and we see its energy mapped on this plane at about 4000 m. Finally, Figure 2.16(d) shows a plane at a large curvature, $q = 7200$ m/deg. Notice the energy from the diffracted multiple at approximately $\Gamma = 8$ deg.

It is important to emphasize the difference between the standard transform and the apex-shifted transform. While the $\Gamma = 0$ plane of the apex-shifted transform is similar to the standard transform, they are not the same, as shown in Figure 2.17. Both panels in this figure are plotted with the exact same plotting parameters. Primaries are mapped near the $q = 0$ line in both planes while specular multiples are mapped to other $q$ values. Notice how in the standard transform Figure 2.17(a), the diffracted-multiple energy is mapped as background noise, especially at the largest positive and negative $q$ values. In the $\Gamma = 0$ plane of the apex-shifted transform (panel (b)), however, the diffracted multiples are not present since their moveout apex is not zero. These multiples, therefore, do not obscure the mapping of the specular multiples. Notice also that the primary energy is much lower than in Figure 2.17(a) since in the apex-shifted transform the primary energy is mapped not only to the $\Gamma = 0$ plane but to other $\Gamma$ planes as well as illustrated previously in Figure 2.16(b).

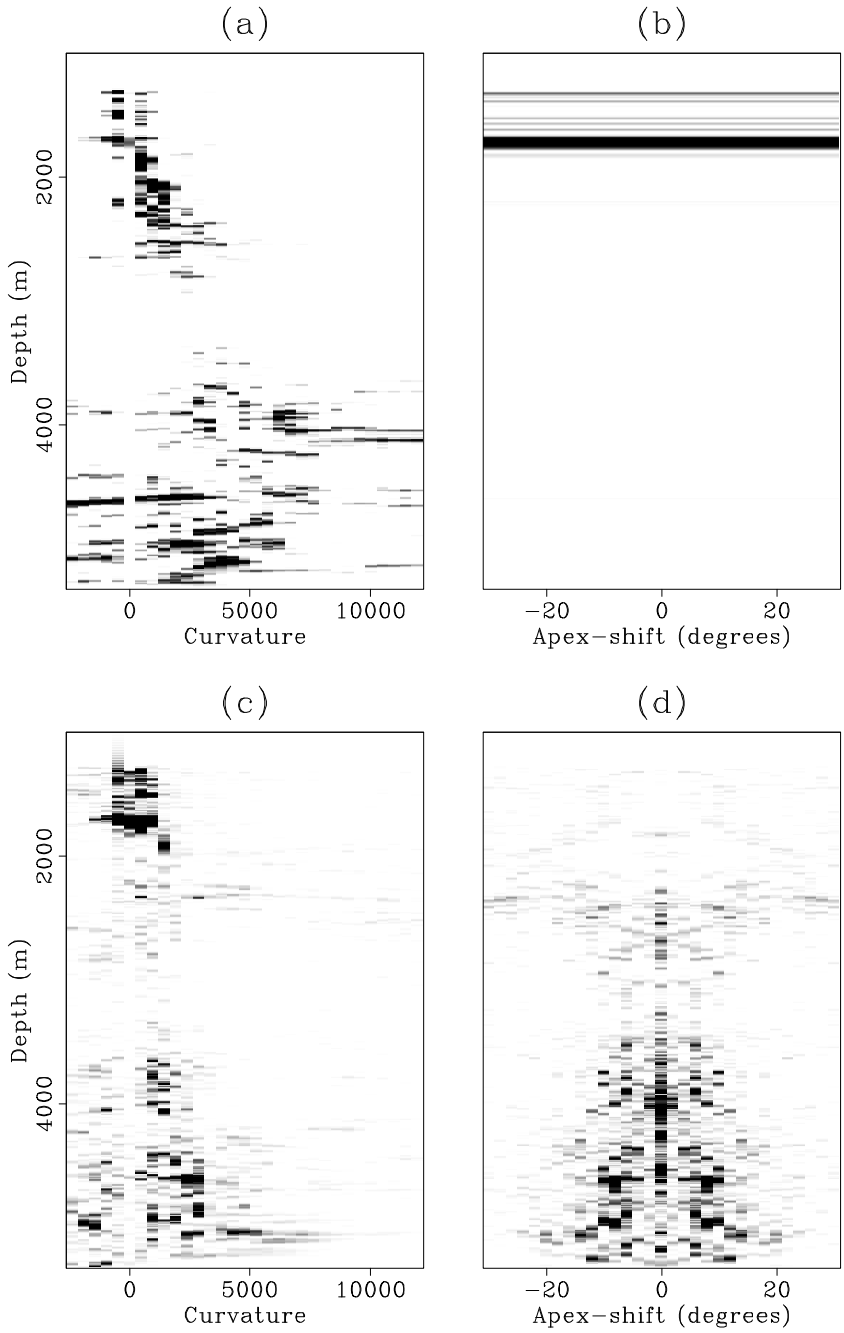


Figure 2.16: Different views from the cube of the apex-shifted transform for the ADCIG at 6744 m. (a): zero apex-shift plane. (b) zero curvature plane. (c): plane at apex shift $\Gamma = 8$ deg and (d): plane at curvature $q = 7200$ m/deg. 2d-envelopes [CR]

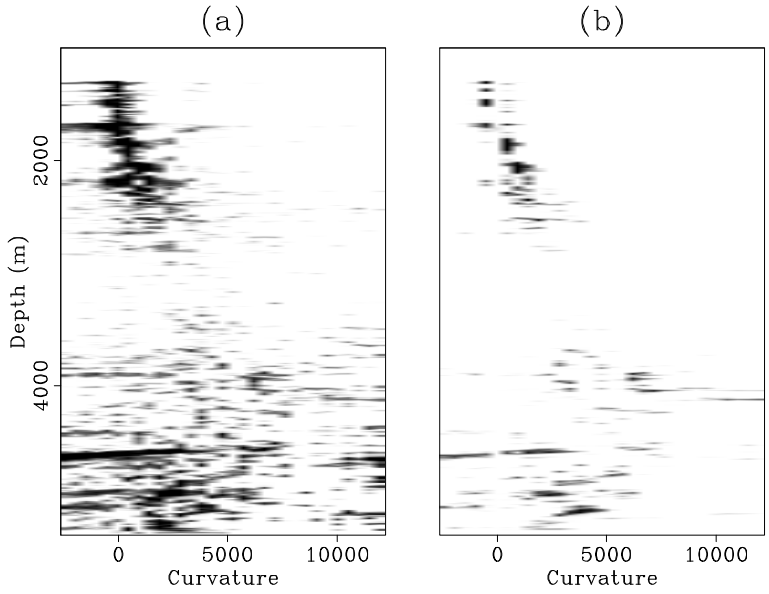


Figure 2.17: Radon transforms of the ADCIG in Figure 2.15b. (a): standard 2D transform. (b): $h = 0$ plane of the apex-shifted 3D transform. Both panels plotted at the exact same clip value. 2d-radon_comp [CR]

## MULTIPLE ATTENUATION RESULTS

Rather than suppressing the multiples in the model domain, I chose to suppress the primaries and inverse transform the multiples to ADCIGs. This is more convenient because the primaries are not "filtered" through the imperfect forward-inverse Radon transform pair. The primaries were then recovered by directly subtracting the multiples from the data. I did not apply adaptive subtraction to obtain the results presented in this chapter. This is such an important issue that I designed a new algorithm for it and will present it in the next chapter. Figure 2.18 shows a close-up comparison of the primaries extracted with the standard 2D Radon transform (Sava and Guitton, 2003) and with the apex-shifted Radon transform for the two ADCIGs at the top in Figure 2.15. The standard transform (Figures 2.18a and 2.18c) was effective in attenuating the specular multiples, but failed at attenuating the diffracted multiples (below 4000 m), which are left as residual multiple energy in the primary data. Again, this is a consequence of the apex shift of these multiples. There appears not to be any subsalt primary reflections in Figures 2.18a and 2.18(b). The flattish reflector at about 4600 m in panel (b) is actually

residual multiple energy (compare with panel (a)). Similarly for Figures 2.18(c) and 2.18(d). Figure 2.19 shows a similar comparison for the extracted multiples. Notice how the diffracted multiples were correctly identified and extracted by the apex-shifted Radon transform, in Figures 2.19(b) and 2.19(d). In contrast, the standard 2D transform misrepresent the diffracted multiples as though they are specular multiples as seen in Figures 2.19(a) and 2.19(c).

In order to assess the effect of the improved attenuation of the diffracted multiples on the angle stack, I processed all ADCIGs. Figure 2.20 shows a close-up view of the stack of the primaries extracted with the standard Radon transform (panel (a)), the stack of the primaries extracted with the apex-shifted Radon transform (panel (b)), and their difference (panel (c)). All panels are plotted with the same plotting parameters. Notice that the diffracted multiple energy below the edge of the salt (5000 m to 7000 m) that appears as steeply-dipping noise with the standard transform, has been somewhat better attenuated with the apex-shifted transform. This is shown in detail in the difference panel in Figure 2.20(c). It is very difficult to identify any primary reflections below the edge of the salt, so it is hard to assess if the primaries have been equally preserved with both transforms. It is known, however, that for this dataset, there are no multiples above a depth of about 3600 m, between CMP positions 3000 m to 5000 m. The fact that the difference panel appears nearly white in that zone shows that the attenuation of the diffracted multiples did not affect the primaries. Of course, this is only true for those primaries that were correctly imaged, so that their moveout in the ADCIGs was nearly flat. Weak subsalt primaries may not have been well-imaged due to inaccuracies in the migration velocity field and 3D effects. These primaries, therefore, may have been attenuated with both the standard and the apex-shifted Radon transforms.

For the sake of completeness, Figure 2.21 shows the extracted multiples with the standard and the apex-shifted Radon transforms. Again, the main difference is largely in the diffracted multiples.

## DISCUSSION

In this section I discuss some important practical aspects of my method. I start, however, with a discussion on the relative merits of attenuating the multiples in image space as opposed to

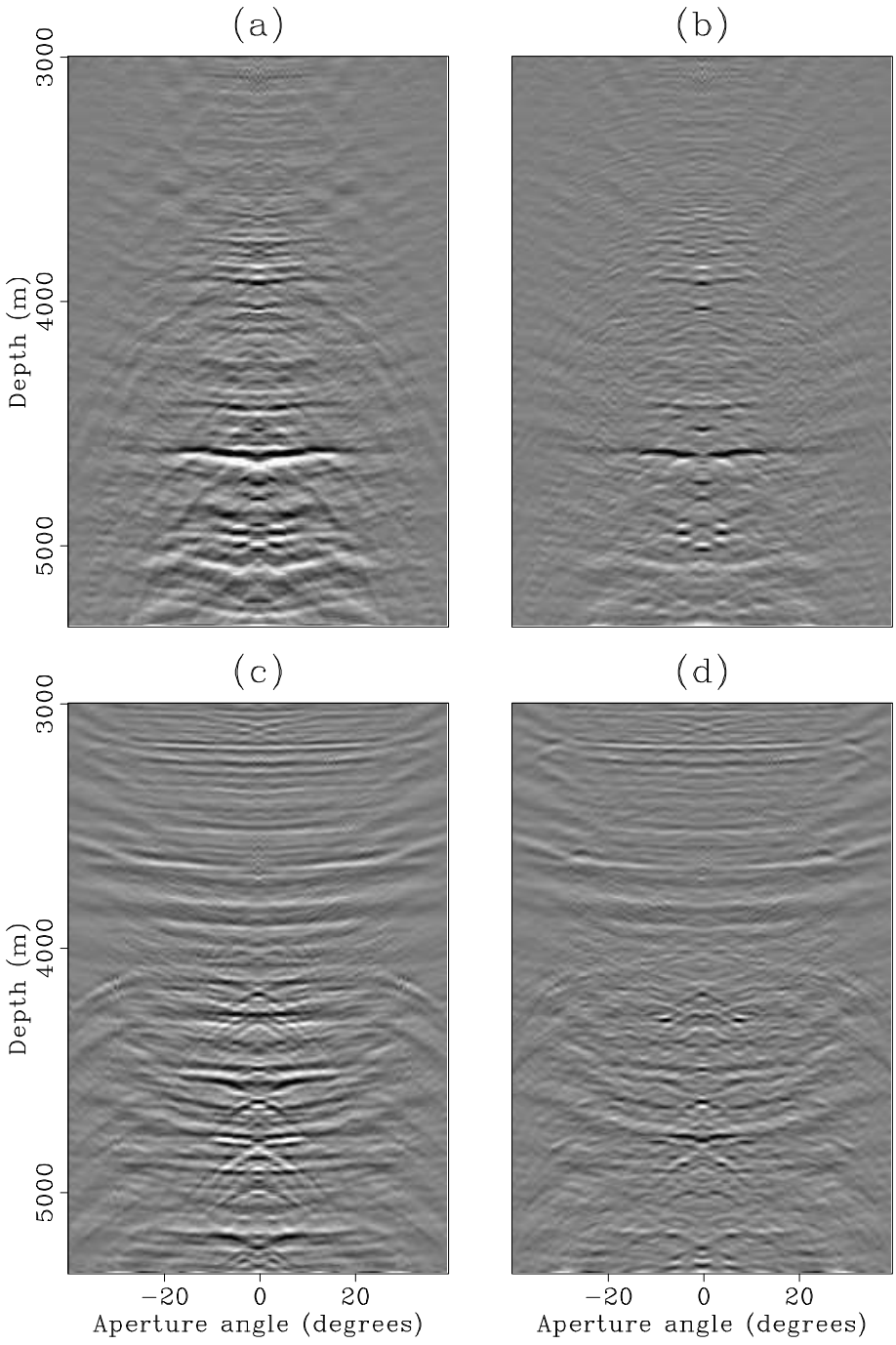


Figure 2.18: Comparison of primaries extracted with the 2D Radon transform (a) and (c) and with the apex-shifted Radon transform (b) and (d). Notice that some of the diffracted multiples remain in the result with the 2D transform. 2d-comp_prim1 [CR]

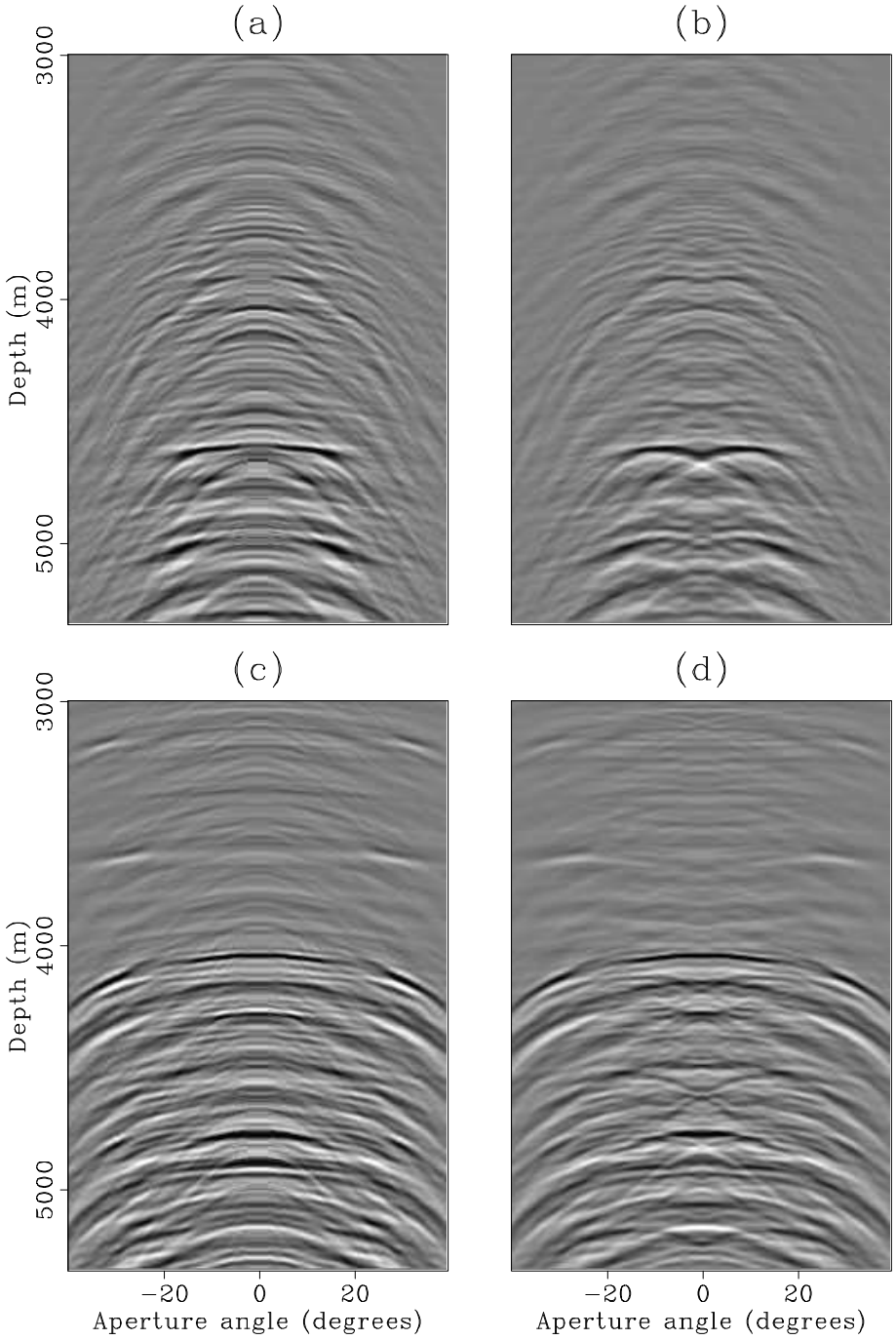


Figure 2.19: Comparison of multiples extracted with the 2D Radon transform (a) and (c) and with the apex-shifted Radon transform (b) and (d). 2d-comp_mult1 [CR]

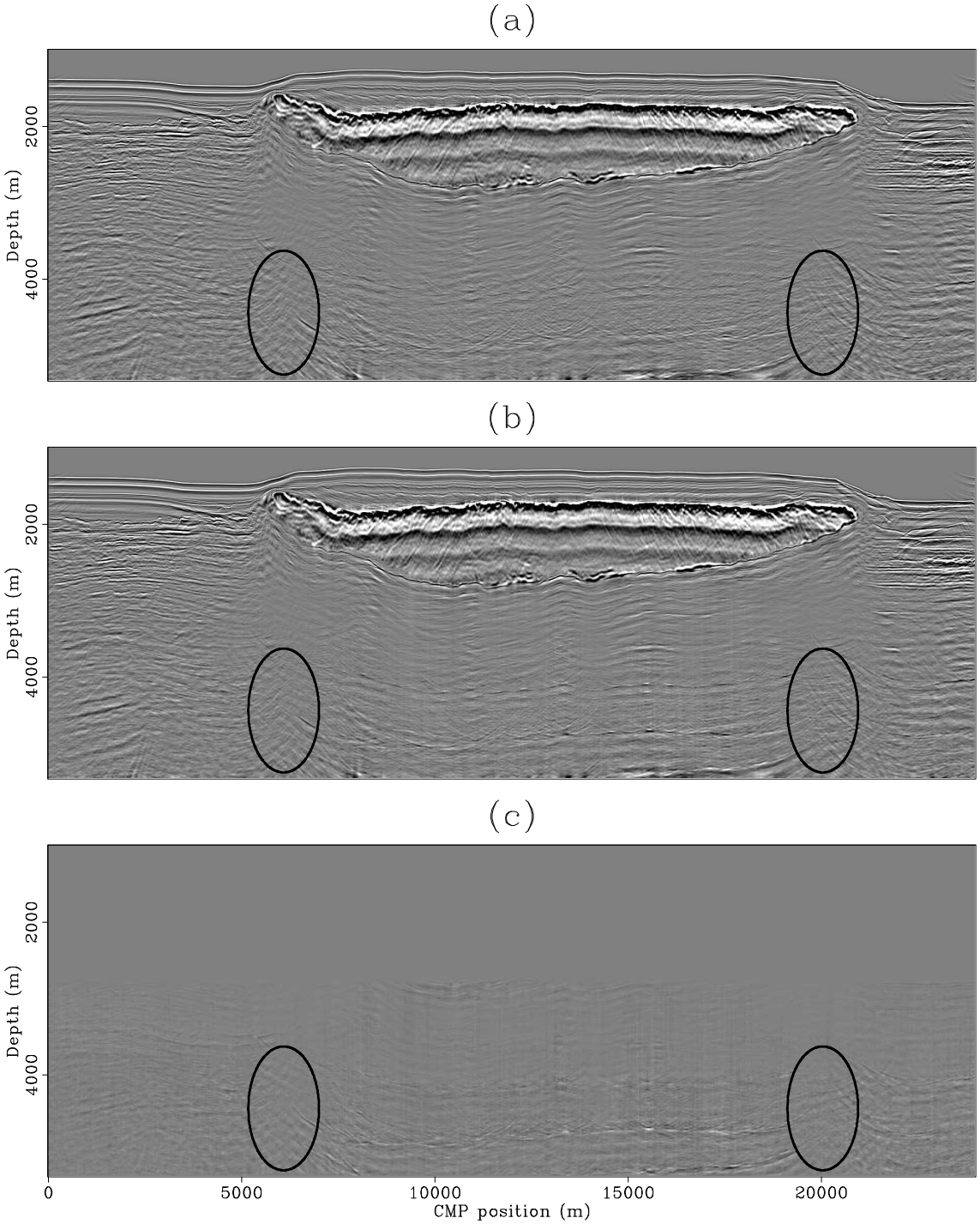


Figure 2.20: Comparison of angle stacks for primaries. Panel (a) corresponds to the primaries obtained with the standard Radon transform. Panel (b) corresponds to the primaries obtained with the apex-shifted Radon transform and panel (c) is the difference between panels (a) and (b). The ovals correspond to the diffracted multiples. 2d-comp_prim1_stack [CR]

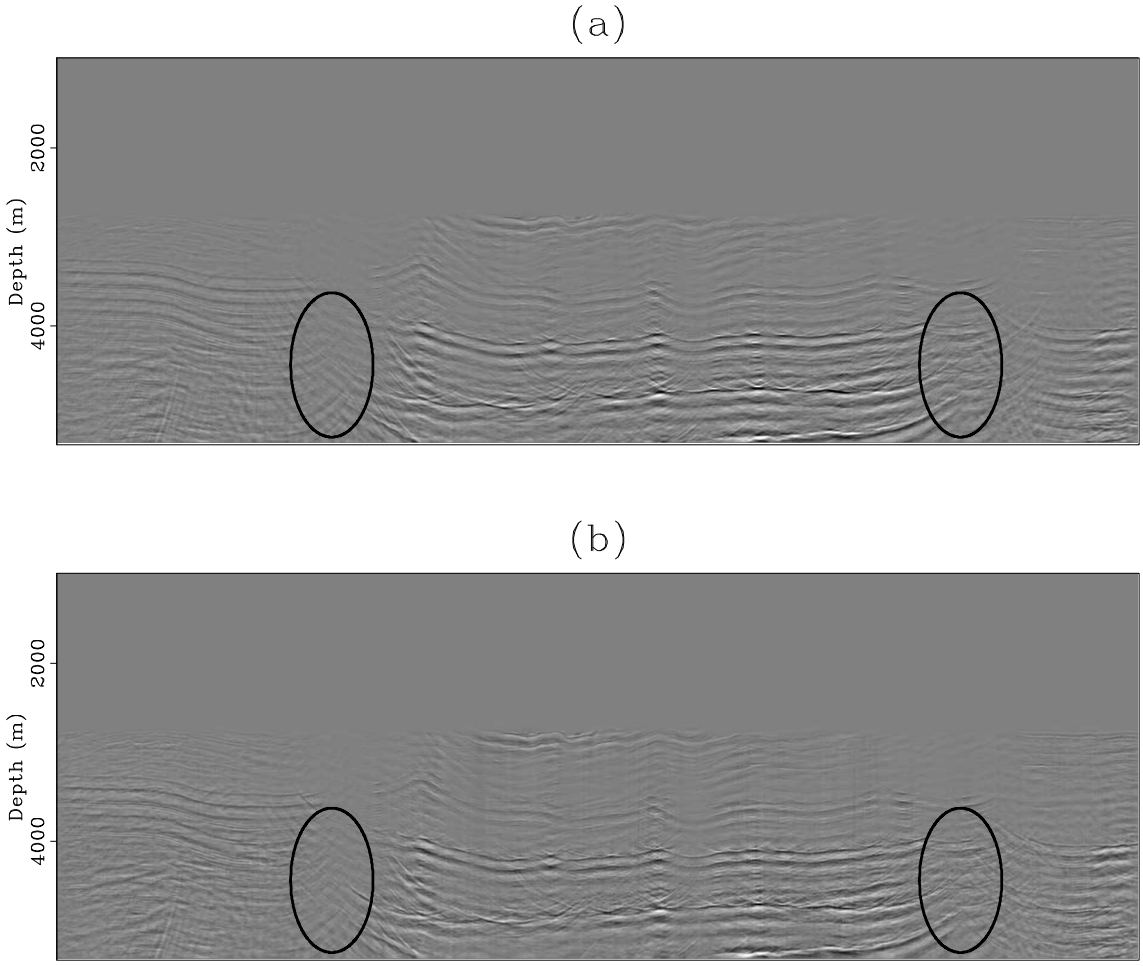


Figure 2.21: Comparison of angle stacks for multiples. Panel (a) corresponds to the multiple model computed with the standard Radon transform. Panel (b) corresponds to the multiple model computed with the apex-shifted Radon transform. Notice the difference in the attenuation of the diffracted multiples. The ovals correspond to the diffracted multiples. 2d-comp_mult1_stack [CR]

the industry standard of attenuating them in data space.

**Image space vs. Data space**

In principle, attenuating the multiples in data space has the important advantage that the estimation of the migration velocity field is not affected by the presence of the multiples. This is only true, however, provided that the level of attenuation is such that no significant residual multiple energy remains (that could be mistaken as primaries) and that the primaries are unaffected by the attenuation of the multiples. As discussed before, this is unlikely to be the case for data-space Radon filtering when the subsurface is complex. Furthermore, any residual multiple energy will distort the imaging of the primaries resulting in a deficient final image.

SRME can effectively attenuate all multiples with a bounce at the water surface, but only if all necessary data is collected. Virtually in all instances of real 3D data acquisition, the cross-line sampling is too coarse, the cross-line aperture is too small, the short offsets are missing, and acquisition obstacles and cable feathering produce irregular geometry. The data need to be interpolated and extrapolated to satisfy the requirements of 3D SRME. This is not a trivial endeavor and the performance of SRME greatly depends on it. Moreover, diffracted multiples and specular multiples from an interface with steep cross-line dip, may have bounce points well outside the cross-line aperture making them hard or impossible to predict.

Attenuating the multiples in image space solves the problem of the complex wave propagation of primaries and multiples. Prestack wave-equation migration takes care of the complexity of the wavefield propagation and makes the primaries very likely to be flat in ADCIGs and therefore more easily separable from the multiples in the Radon domain. No data interpolation or extrapolation is necessary because no multiples are predicted. Since very accurate migration velocities are always necessary to get a good depth image, however, postponing the multiple attenuation step until after migration does not come without a price. Computation of an accurate migration velocity field may be compromised by the presence of the multiples.

**Sensitivity to errors in migration velocities**

From the point of view of the attenuation of the multiples, it is important that the migration velocities be accurate enough for the primaries to be flat and the multiples to exhibit residual moveout in ADCIGs. This is likely to be the case for water-bottom and peg-leg multiples since water velocity is very different from sediment velocity, but may not be so for internal multiples. Therefore, the method is likely to be successful in attenuating water-bottoms and peg-leg multiples even if there are small errors in the estimation of the migration velocity field. Attenuation of internal multiples will require more accurate migration velocities.

**Radon transform parameters**

The performance of the Radon transform to focus the primaries and multiples to separate regions of the transformed domain, depends on the choice of curvature parameters and apex-shift values. In particular, curvatures should range from small negative values to allow for the possibility of slightly under-migrated primaries, to large enough values to accommodate the maximum curvatures of the over-migrated multiples. I have found that these are not particularly critical parameters as long as the curvature sampling is fine enough to avoid aliasing in the Radon domain. Similarly for the apex-shift parameters. They are not critical, since their role is only to provide room for the mapping of the diffracted multiples, thus preventing them from interfering with the primaries and the specular multiples that map to the zero apex-shift plane. A critical step is the design of the mute pattern to eliminate the primaries and keep the multiples. There are several ways that this could be implemented. I constructed a mask of ones for the multiple regions and zeros for the primary region, smoothed it laterally and in depth and multiplied it by the transformed data.

An important, and somewhat difficult parameter to estimate, is the one that controls the Cauchy regularization (parameter $b$ in equation 2.33). We want the data in the ADCIG to be explained in the Radon domain by as few parameters as possible but avoiding the risk of attenuating the contribution from weak subsalt primaries. This is a trial and error parameter and it requires some testing to get a satisfactory value.

### Comment on diffracted multiples

The results shown in the previous section demonstrate that with the apex-shifted Radon transform it is possible to attenuate, although not completely remove, the diffracted multiples. It should be noted, however, that in our seismic section it is very difficult to find a legitimate primary reflection below the salt and in particular below the edge of the salt, where the contamination by the diffracted multiples is stronger. It is somewhat disappointing that the attenuation of the diffracted multiples did not help in uncovering any meaningful primary reflections in our example. I expect the situation to be different with other datasets. I should also emphasize that adding the extra dimension to deal with the diffracted multiples does not in itself resolve the usual trade-off between primary preservation and multiple attenuation. We saw this limitation in this case, which forced us to let some residual multiple energy leak into the extracted primaries. The flatter the primaries are in the ADCIGs, and the more accurately the kernel of the Radon transform approximates the residual moveout of the multiples, the better are our chances of reducing the residual multiple energy.

### Extension to 3D data

With 3D data, the ADCIGs are function of the reflection azimuth as well as the aperture angle (Biondi and Tisserant, 2004). The ADCIGs, therefore, are three dimensional and even for the specular multiples the Radon transform will also be three-dimensional. For the diffracted multiples, the apex shift is a function of both the aperture angle and the reflection azimuth and the Radon transform would be more complicated. This issue will be addressed in Chapter 4.

## CONCLUSIONS

To attenuate multiples in the image space via filtering in the Radon domain, we need an accurate representation of their residual moveouts in either SODCIGs or ADCIGs. Accounting for ray-bending at the multiple-generating interface increases the focusing power of the Radon transform and therefore the separation between primaries and multiples.

The apex-shifted Radon transform in ADCIGs to map from $(z, \gamma)$ to $(z', q, h)$ has proven to be effective in attenuating specular and diffracted multiples in 2D marine data. The residual moveout of both multiples in ADCIGs is well-behaved and the extra dimension provided by the apex-shift allows the attenuation of the multiples without compromising the integrity of the primaries.

## ACKNOWLEDGMENTS

I thank WesternGeco for providing the dataset.

# Chapter 3

# Simultaneous adaptive matching of primaries and multiples


**SUMMARY**

In this chapter, I develop a method to match estimates of primaries and multiples to data containing both. The method works with prestack or poststack data in either data space or image space and addresses the issue of cross-talk (leakage) between the estimates of the primaries and the estimates multiples. I pose the problem as a non-linear optimization in which non-stationary filters are computed in micro-patches to simultaneously match the estimates of the primaries and the multiples to the data, in a least-squares sense. I apply the method iteratively by updating the estimates of the primaries and the multiples after the least-squares solution is found. Only a few of these iterations are needed. The computer cost is a negligible fraction of the cost of computing the estimate of the multiples with convolutional methods such as SRME. I show, with several synthetic and real data examples, that the matched estimates of both primaries and multiples have little cross-talk. I also apply the method to the separation of spatially-aliased ground-roll and body waves and show that most residual ground-roll contaminating the estimate of the body waves can be eliminated. This method is applied in chapter 6 to adaptively match and subtract the multiple estimate from a 3D real dataset from the Gulf of Mexico.

## INTRODUCTION

Most methods to attenuate multiples perform, in one way or another, two complementary but clearly distinguishable steps: first, estimate a model for the multiples, and second, adaptively match and subtract the estimate of the multiples from the data to get the estimate of the primaries. As described in chapter 1, Surface Related Multiple Elimination (Berkhout and Verschuur, 1997; Verschuur and Berkhout, 1997; Weglein et al., 1997; Dragoset and Jericevic, 1998; Dragoset, 1999) uses the auto-convolution of the data to estimate the multiples whereas moveout-based methods use filtering in either the frequency-wavenumber or a Radon-transform domain (Hampson, 1986; Sava and Fomel, 2003; Alvarez et al., 2004) to estimate the multiple model. Whatever the method, the estimate of the multiples is likely to be contaminated with residual primary energy and to have errors in amplitude, phase and frequency content. After adaptive subtraction, the estimated primaries are likely to suffer from undesired residual multiple energy, or weakened primaries, or both (Guitton, 2005a).

In this chapter I assume that the multiple model has already been estimated by some method and concentrate on the adaptive subtraction step to get the estimated-matched primaries. I present a new adaptive matching algorithm that simultaneously matches estimates of the primaries and the multiples to the data. In contrast, the most standard algorithms adaptively match the multiples only. Matching also the estimate of the primaries help constrain the matching of the multiples thus reducing the leak of residual multiples (so-called cross-talk) on the estimated primaries.

The new adaptive-matching algorithm estimates, in the least-squares sense, non-stationary filters (Rickett et al., 2001) that simultaneously match both the estimates of the primaries and the multiples to the data. These filters act on micro-patches *i.e* small, overlapping pieces of data (Claerbout and Fomel, 2002) and can handle inaccuracies in the estimated multiples in terms of both amplitudes and kinematics. Once the solution to the least-squares problem is computed, I iteratively re-estimate the multiple and primary models until the residual (the sum of the matched primaries and multiples minus the data) is close to zero. In my experience, as few as three to five iterations of the least-squares inversion ("outer" iterations) seem sufficient.

I apply this new method to two synthetic datasets contaminated with multiples. In the

first test, I match kinematically perfect estimates of primaries and multiples contaminated with 40% of cross-talk and show that for this simple case the method produces a cross-talk-free result. Then I apply the method to an inaccurate estimate of both the primaries and the multiples obtained via migration-demigration as described in Alvarez (2006). Even with a poor initial estimate of both primaries and multiples, with strong cross-talk on both, the matched results are very good, with little cross-talk. To illustrate the method with stacked data, I apply it to a migrated section of the Sigsbee model. Here the multiples were estimated with an image space version of SRME (Artman and Matson, 2006). The results show that the method attenuated most of the multiples and produced a largely multiple-free estimate of the primaries.

The method performs well with real data, as I demonstrate by applying it to match the estimated multiples computed in the previous chapter. I adaptively matched and subtracted the multiple estimate of each individual ADCIGs and then stacked the estimated primaries to form an angle stack of primaries only. The method performed very well and the multiples were nicely attenuated in the angle stack.

Finally, to illustrate that the method may have applications beyond the matching of primaries and multiples, I apply it to a different problem, namely the separation of ground-roll and body-waves. I use a shot gather from a land dataset contaminated with strong, spatially-aliased, ground-roll and show that most of the residual ground-roll can be attenuated in the final estimate of the body waves. In a way, this is a more challenging problem because the non-stationarity characteristics of the ground-roll and the body waves are different. The requirements of filter lengths and patch sizes to match the data are therefore different for the ground-roll and the body-waves. I chose to preserve the body waves even if that meant allowing some residual ground-roll.

## DESCRIPTION OF THE METHOD

Conceptually, the first step of the new method is to form the convolutional matrices of both the estimated multiples $\mathbf{M}$ and the estimated primaries $\mathbf{P}$. In practice, these are huge matrices that are not explicitly formed but are replaced by equivalent linear operators (Claerbout and Fomel,

2002). Next, I compute non-stationary filters in micro-patches (that is, filters that act locally on overlapping two-dimensional partitions of the data) to match the estimated multiples and the estimated primaries, to the data containing both. I compute the filters by solving the following linear least-squares inverse problem:

$$\begin{bmatrix} \mathbf{M} & \mu\mathbf{P} \end{bmatrix} \begin{bmatrix} \mathbf{f_m} \\ \mathbf{f_p} \end{bmatrix} \approx \mathbf{d} \tag{3.1}$$

$$\epsilon\mathbf{A} \begin{bmatrix} \mathbf{f_m} \\ \mathbf{f_p} \end{bmatrix} \approx \mathbf{0} \tag{3.2}$$

where $\mathbf{f_m}$ and $\mathbf{f_p}$ are the matching filters for the multiples and primaries respectively, $\mu$ is a parameter to balance the relative importance of the two components of the fitting goal (Guitton, 2005b), $\mathbf{d}$ is the data (primaries and multiples), $\mathbf{A}$ is a regularization operator, (in my implementation a Laplacian operator), and $\epsilon$ is the usual parameter to control the level of regularization.

Once convergence is achieved, each filter is applied to its corresponding convolutional matrix, and new estimates for $\mathbf{M}$ and $\mathbf{P}$ are computed:

$$\mathbf{M}_{i+1} \leftarrow \mathbf{M}_i \mathbf{f}_{\mathbf{m}i} \tag{3.3}$$

$$\mathbf{P}_{i+1} \leftarrow \mu\mathbf{P}_i \mathbf{f}_{\mathbf{p}_i}. \tag{3.4}$$

Here $i$ represents the index of the outer iteration of the linear problem described by Equations 3.1 and 3.2. Notice that I hold $\mu$ constant although it could be changed from iteration $i$ to iteration $i+1$. Also notice that the regularization operator $A$ and the regularization parameter $\epsilon$ in Equation 3.2 could be different for $\mathbf{f_m}$ and $\mathbf{f_p}$. I have chosen to keep them the same to limit the number of adjustable parameters. This choice worked very well in all my tests. The updated versions of the convolutional matrices $\mathbf{M}_{i+1}$ and $\mathbf{P}_{i+1}$ are plugged into equations 3.1 and 3.2 and the process repeated until the cross-talk has been eliminated or significantly attenuated.

## EXAMPLES WITH SYNTHETIC DATA

As a first example, I will consider the synthetic dataset shown in panel (a) of Figure 3.1. There are two primaries (black) and four multiples (white). The traveltimes of both primaries and multiples were computed analytically from a three flat-layer model: water layer, a sedimentary layer and a half space. The estimates of the multiples (b) and primaries (c) were computed by adding 40% of the primaries to the multiples and 40% of the multiples to the primaries, respectively. The goal is to simulate a situation in which the kinematics of the estimates of primaries and multiples are both correct but there is strong cross-talk (leakage) between them.

Figure 3.2 shows the estimated multiples after one, two and three outer iterations of the algorithm. The corresponding results for the estimated primaries are shown in Figure 3.3. In both figures we see that the cross-talk is substantially reduced after the first outer iteration and is completely eliminated after the third. Notice the hole in the top multiple and the bottom primary in the final estimates. This is actually present in the data (panel (a) in Figure 3.1) and is an artifact because both primaries and multiples were modeled with the same amplitude and opposite polarity.

Consider now the more realistic situation of kinematic and offset-dependent amplitude errors in the original estimates of both primaries and multiples, as well as noise as shown in Figure 3.4. The multiple and primary estimates were obtained via migration-demigration as described in Alvarez (2006). These are imperfect estimates with cross-talk on primaries and multiples and other noises.

Panel (a) of Figures 3.5 and 3.6 show the results after one outer iteration, whereas panels (b) and (c) of the same figures show the results after three and five outer iterations respectively. There is still some localized cross-talk from the multiples into the primaries.

The next example uses the well-known Sigsbee model (Paffenholz et al., 2002) to illustrate the method in the image space. For this example, therefore, “data” means the migrated image with primaries and multiples. This dataset has the advantage that, along with the modeled data (primaries and multiples), there exists a related dataset without the free surface multiples (http://www.delphi.tudelft.nl/SMAART/S2Breadme.htm). Panel (a) of Figure 3.7 shows the

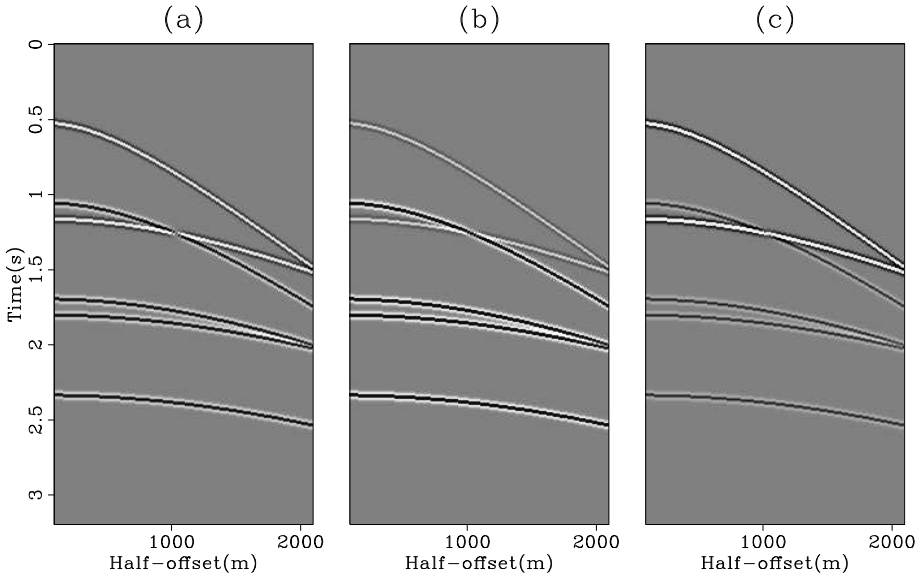


Figure 3.1: Synthetic CMP gather (a) showing two primaries (black) and four multiples (white) from a three flat-layer model. The initial estimates of multiples (b) and primaries (c) are contaminated with 40% cross-talk. adaptive-syn1_estimates1 [ER]

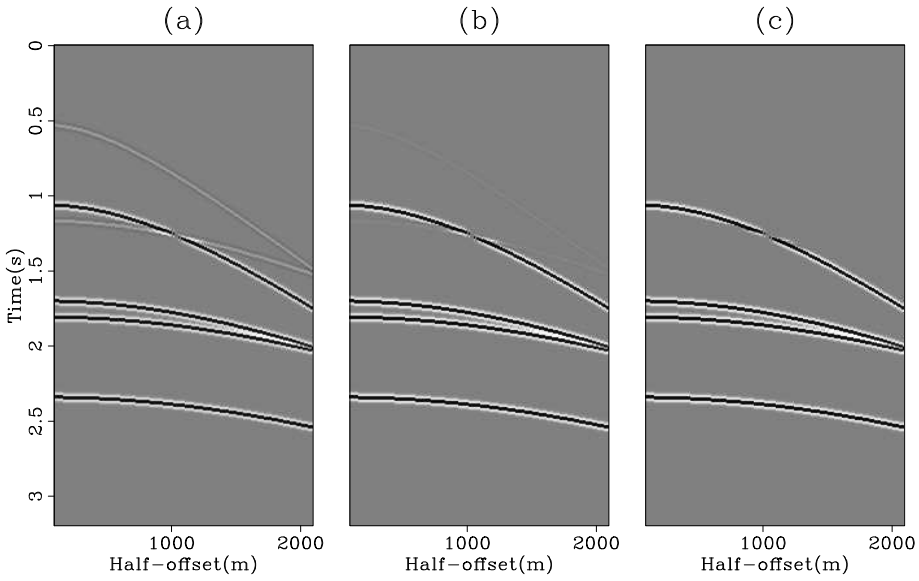


Figure 3.2: Matched estimates of multiples after one (a), two (b) and three (c) outer iterations of the algorithm. adaptive-syn1_matched_muls [ER]

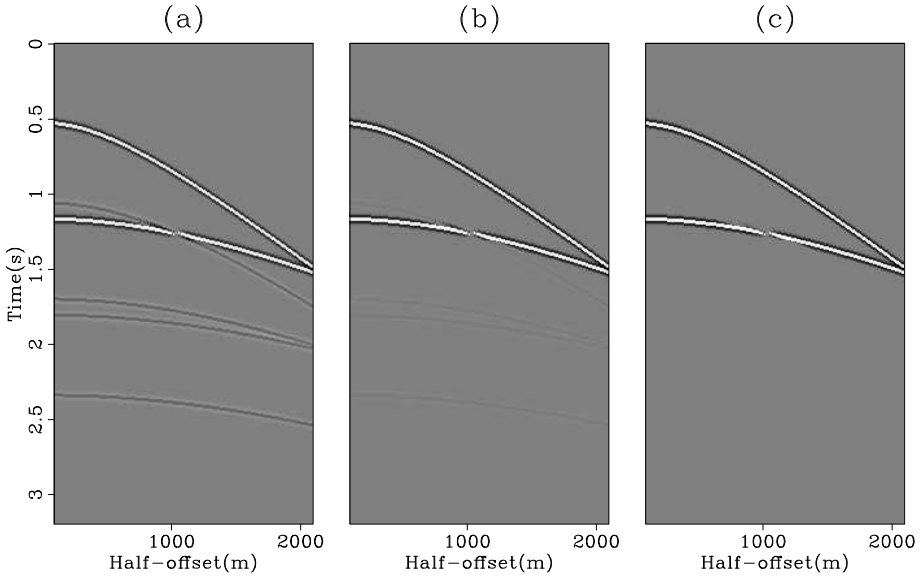


Figure 3.3: Matched estimates of primaries after one (a), two (b) and three (c) outer iterations of the algorithm. adaptive-syn1_matched_prims [ER]

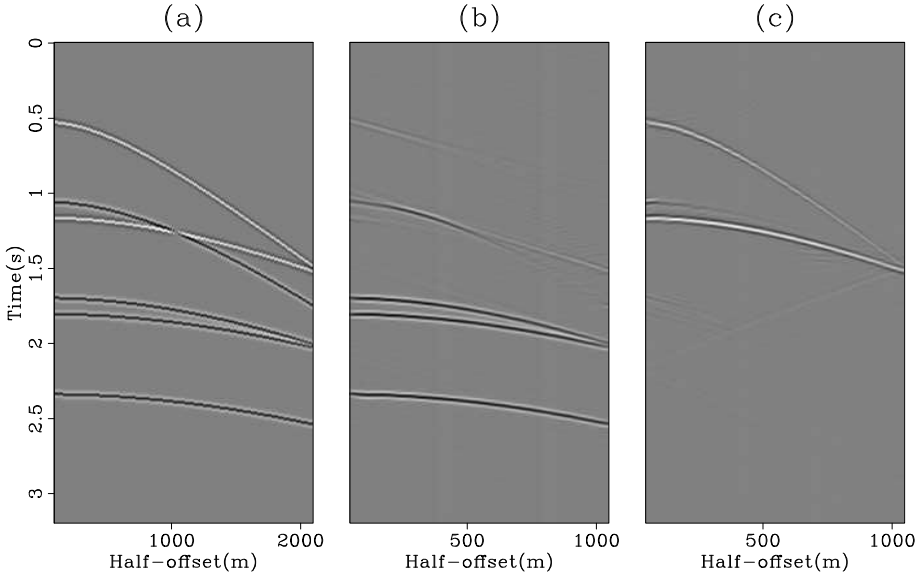


Figure 3.4: Original CMP gather (a), initial estimate of the multiples (b) and initial estimate of the primaries (c). adaptive-syn2_estimates1 [CR]

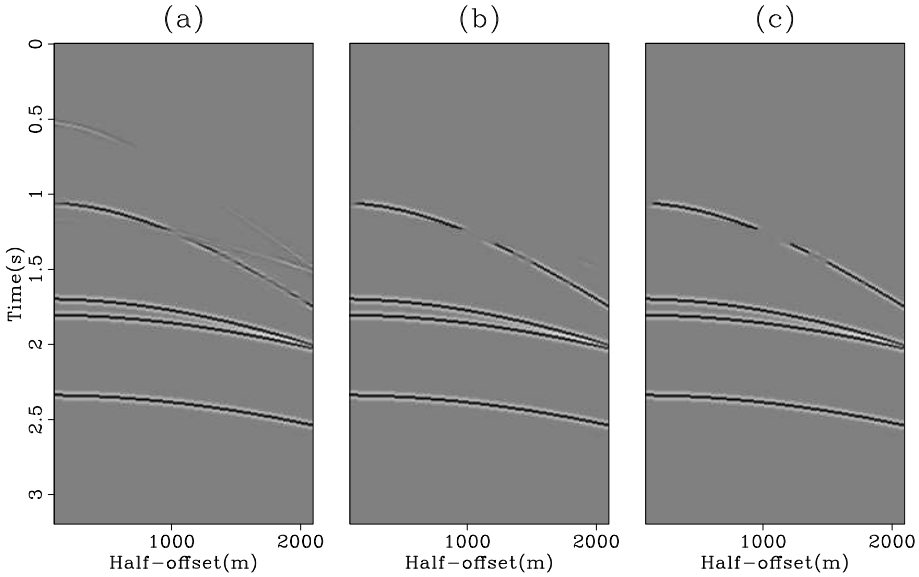


Figure 3.5: Matched estimates of multiples after one (a), three (b) and five (c) outer iterations of the algorithm. adaptive-syn2_matched_muls [CR]

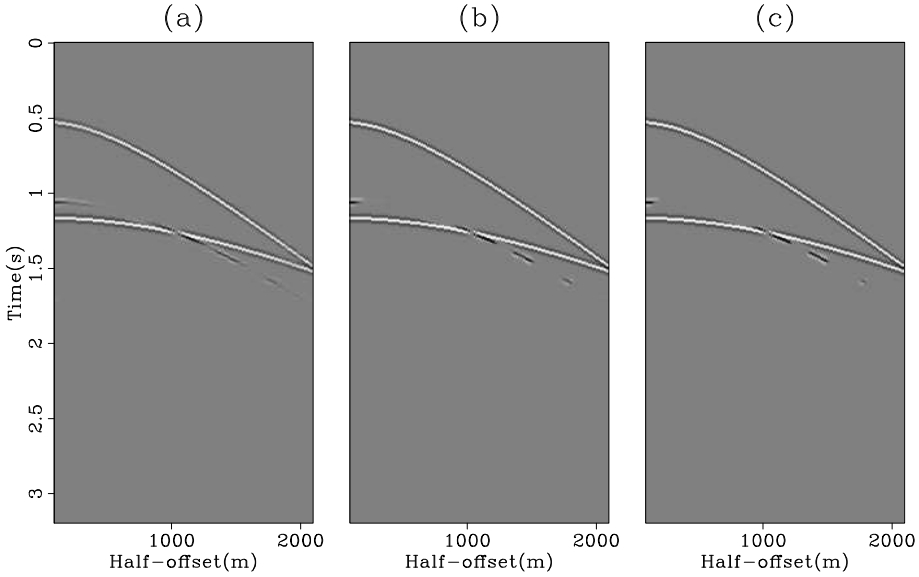


Figure 3.6: Matched estimates of primaries after one (a), three (b) and five (c) outer iterations of the algorithm. adaptive-syn2_matched_prims [CR]

modeled data, panel (b) the data without free surface multiples (b), and panel (c) the estimated free surface multiples in the image space computed with an image space version of SRME (Artman and Matson, 2006). All panels are plotted at the exact same clip value. Notice that the estimate of the multiples is accurate only in kinematics, not in amplitudes or frequency content. The estimate of the multiples was computed with an image space version of SRME (Artman and Matson, 2006).

In contrast with the previous examples, in this case I do not have an independent initial estimate of the primaries. I could subtract the estimate of the multiples from the data, but the corresponding estimate of the primaries is too distorted. Using such a poor primary estimate actually hurts the chances of matching the multiples to the data. Another option is to use the data itself as the initial estimate of the primaries. I found, however, that a better alternative is to do a first iteration setting $\mu = 0$, meaning only the multiples need to be matched. Once matched, the multiples are subtracted from the data to get the estimate of the primaries for the next iteration.

Figures 3.8 and 3.9 show a close-up view of the matched primaries and multiples, respectively, after one, two and three outer iterations. After the first iteration, the most obvious multiples contaminating the estimate of the primaries have been attenuated (compare panels (a) of Figures 3.7 and 3.8) but strong residual multiple energy remains. The second iteration helps attenuate the multiples further, although it is hard to appreciate in these small figures. See, for example the multiple inside the salt and in the bottom right corner of panel (b). The third iteration cleans up most of the noise, although it also weakens the subsalt primaries.

On the estimate of the multiples, again the first iteration extracts the most significant multiples and the second iteration locally corrects the amplitudes. The third iteration actually hurts the estimate of the multiples because the effect of the regularization term becomes significant as the match of both the primaries and the multiples to the data improves. The net result is an estimate of the primaries that is close to the primaries in the original image. Because of the need for regularization, the estimate of the multiples, however, is weaker than it should.

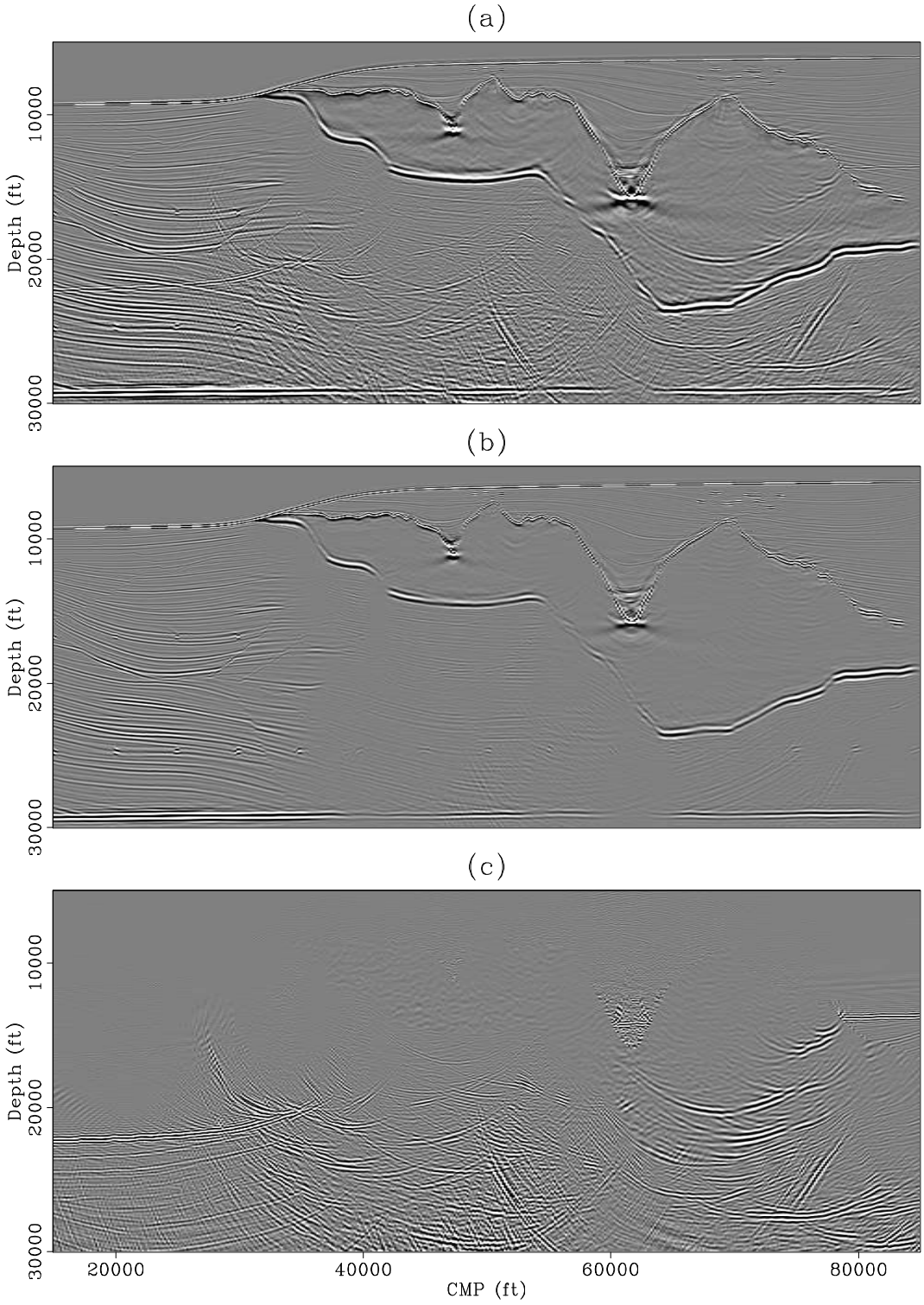


Figure 3.7: Sigsbee migrated dataset. Data (a), migrated model without surface multiples (b) and initial estimates of multiples (c). adaptive-sgsb_estimates1 [CR]

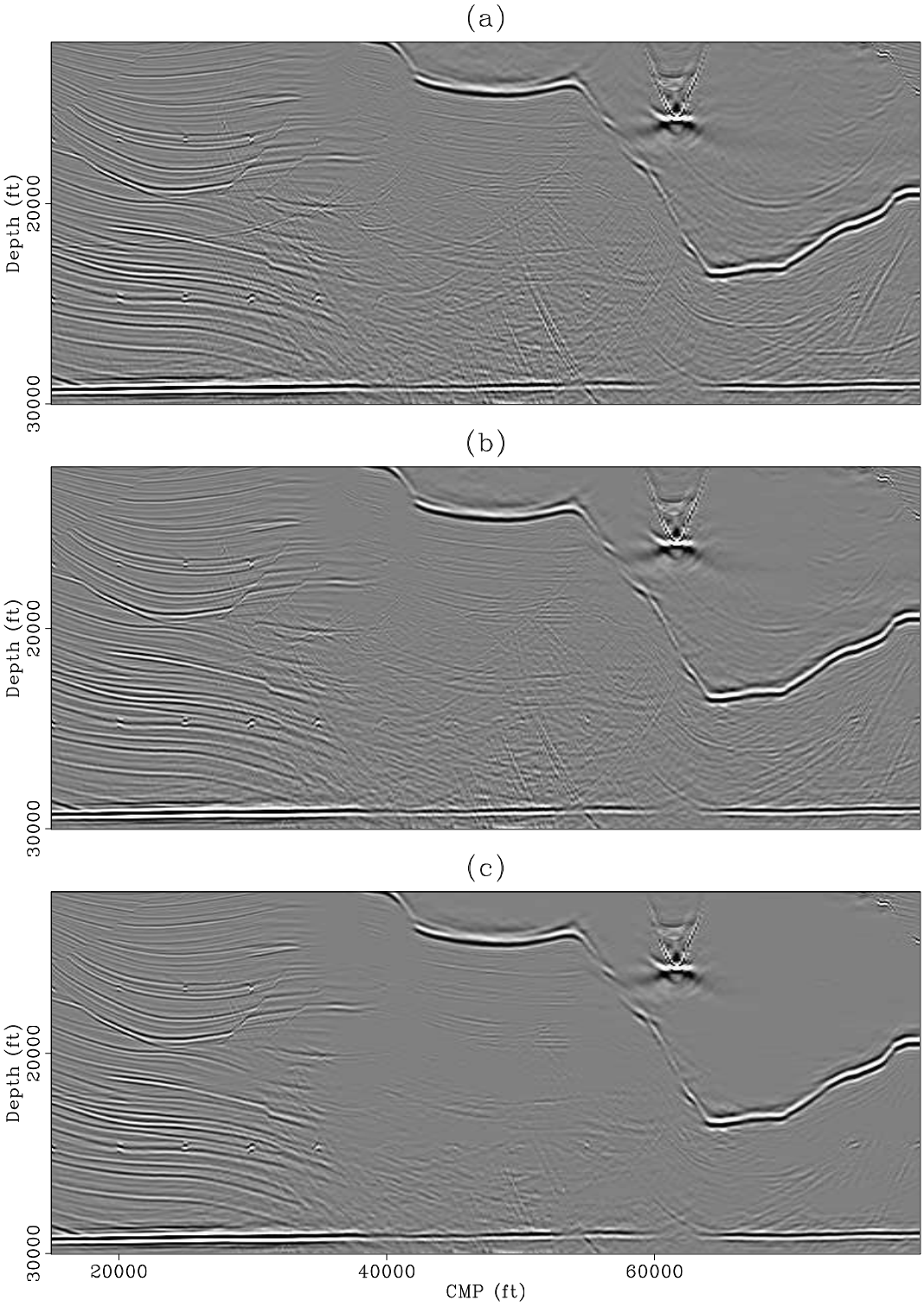


Figure 3.8: Estimated primaries after one (a), two (b) and three (c) outer iterations of the algorithm. adaptive-sgsb_matched_prims [CR]

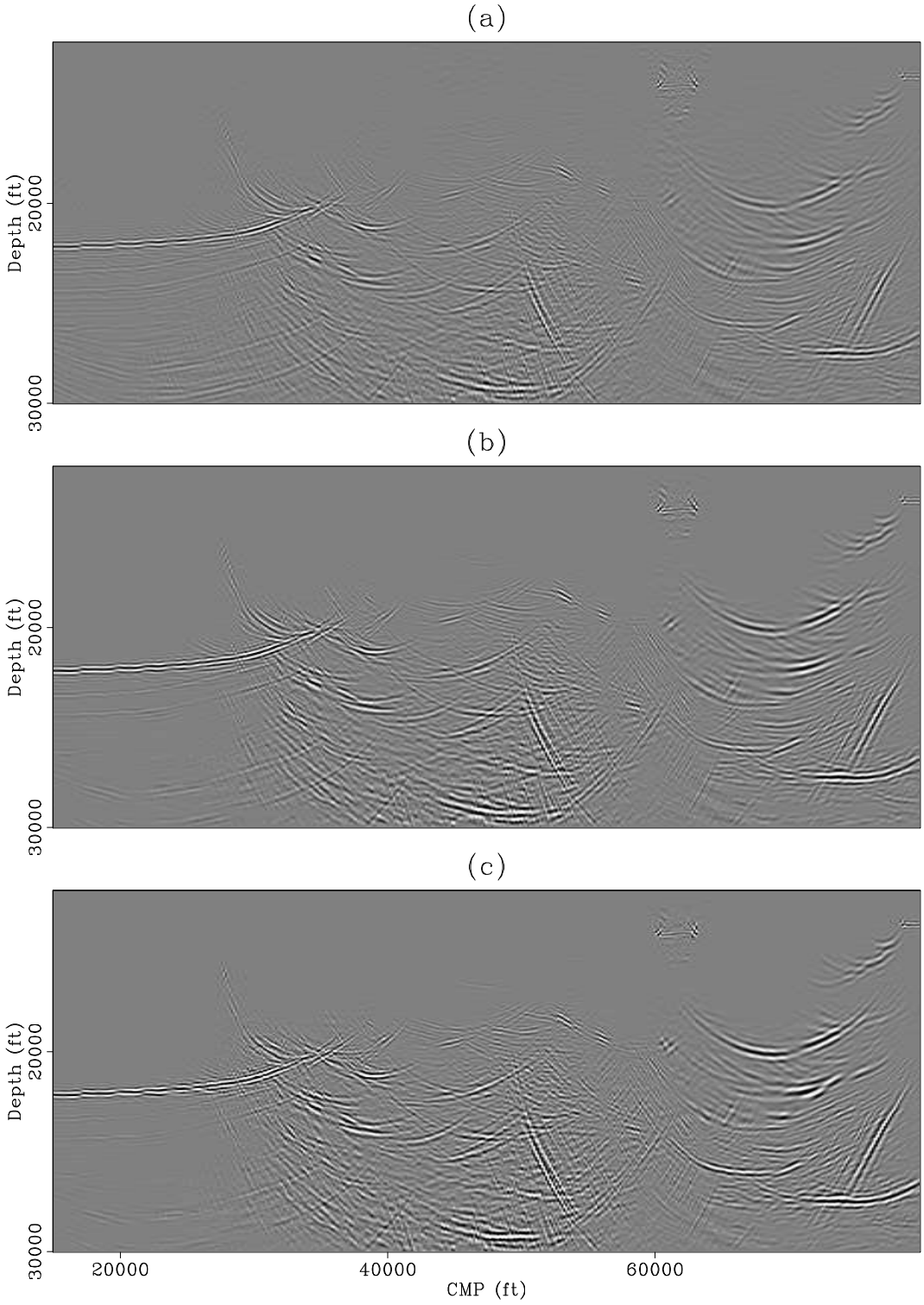


Figure 3.9: Estimated multiples after one (a), two (b) and three (c) outer iterations of the algorithm. adaptive-sgsb_matched_muls [CR]

## EXAMPLES WITH REAL DATA

I will now illustrate the method with real data. First, I will match and subtract the multiple model for the real dataset from the Gulf of Mexico introduced in Chapter 2 and then I will show an example of attenuating spatially-aliased ground-roll.

### Gulf of Mexico data

I start with the Angle-Domain Common-Image Gather (ADCIG) shown in Figure 3.10. Panel (a) is the initial data, panel (b) the estimated multiples and panel (c) the estimated primaries.

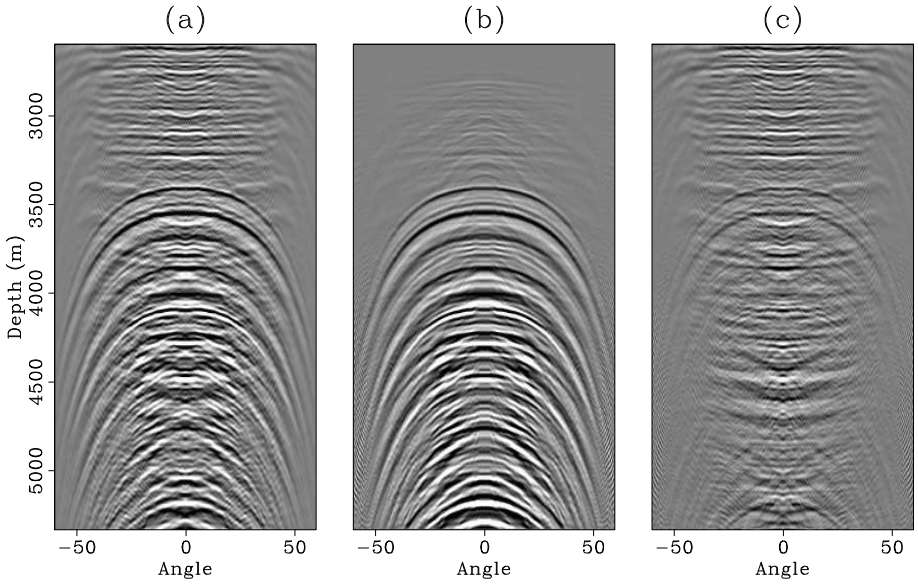


Figure 3.10: ADCIG from the Gulf of Mexico line of chapter 2 (a), initial estimate of the multiples (b), and the primaries (c). Note the crosstalk on both panels. adaptive-adcig1_estimates1 [CR]

The estimate of the multiples was obtained with Radon transform in the image space presented in chapter 2 (without the apex-shift) and the estimate of the primaries was obtained simply by subtracting it from the data. Notice the residual primary energy just below 3000 m in the estimate of the primaries. Note also the residual energy from the multiples in the estimate of the primaries.

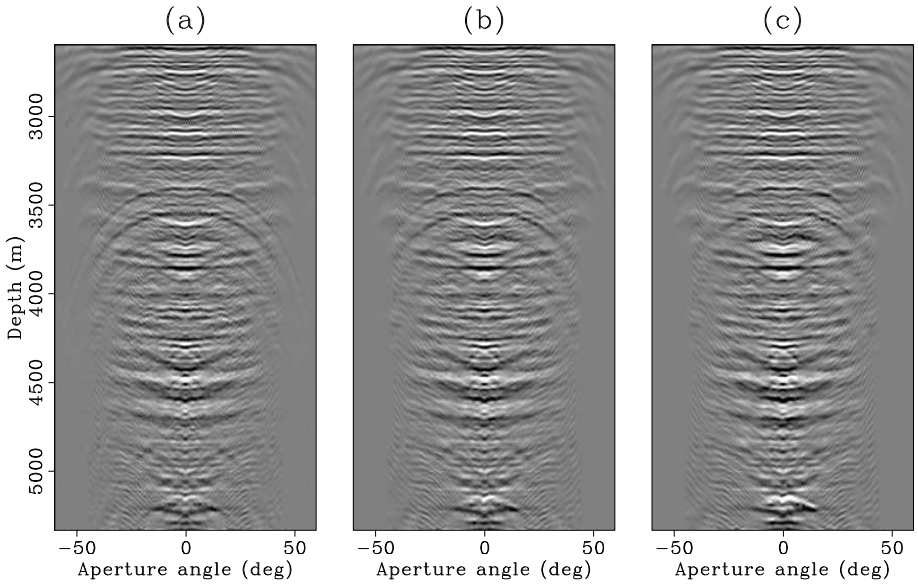


Figure 3.11: Estimated primaries after one (a), five (b) and ten (c) outer iterations. Notice how the residual multiples decrease with the outer iterations although are not completely eliminated. adaptive-adcig1_matched_prims [CR]

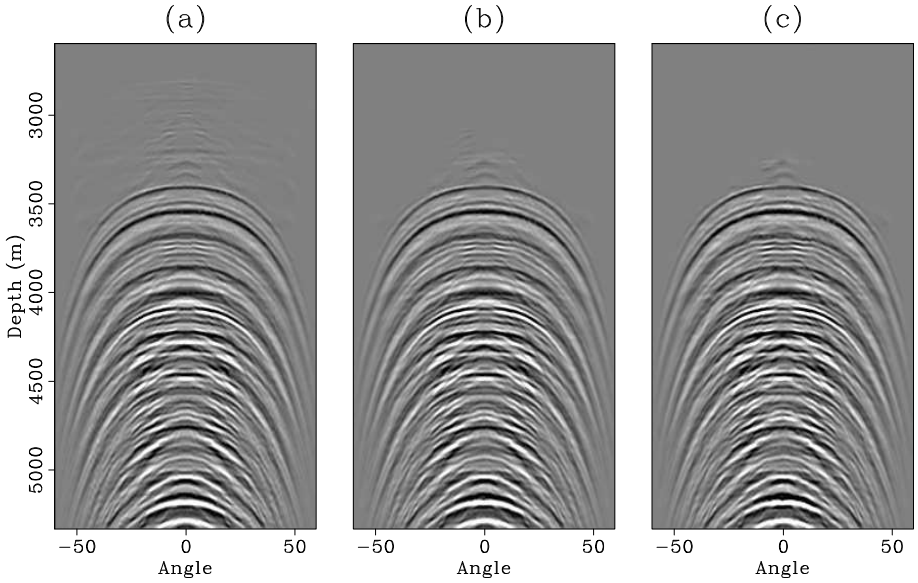


Figure 3.12: Estimated multiples after one (a), five (b) and ten (c) outer iterations. Here too, the residual primaries decrease and almost disappear after the 10th outer iteration. adaptive-adcig1_matched_muls [CR]

Figure 3.11 shows the ADCIG after one, five and ten outer iterations. The first iteration attenuates the strongest residual multiples (compare panel (a) of Figure 3.11 with panel (c) of Figure 3.10). Subsequent iterations further reduce the residual multiples. Also, although hard to see in the hard copy, the primary energy that contaminated the estimate of multiples below 3000 m has been mapped back to the primaries. Figure 3.12 shows the corresponding results for the multiples. Notice again that the residual primary energy has been severely attenuated.

To show the impact of the better matching of the multiples in the angle stack, I applied the same steps to all the 900 ADCIGs in the seismic line. Figure 3.13 shows the angle stack of the data (primaries and multiples) and the angle stack of the initial estimates of the multiples and the primaries. Recall that this initial estimate of the primaries was obtained by direct subtraction of the estimate of the multiples from the data (without adaptive subtraction). All the panels are plot at the exact same clip value. Note that although most multiples have been attenuated some multiple energy remain below the salt body.

In order to concentrate the comparison of the different estimates of the multiples and primaries to the region where the multiples are present, I windowed the data to below 2600 m. Figure 3.14 shows the comparison between the initial estimate of the multiples (a windowed version of panel (c) in Figure 3.13) plot at a lower clip (panel (a)) and the results of applying the matching algorithm after one and five outer iterations (panels (b) and (c) respectively). The first outer iteration didn't improve much, but after five outer iterations the result is much better with the specular multiples largely reduced in amplitude. The diffracted multiples still remain because the Radon filtering did not account for the apex-shift in this example.

**Ground-roll**

As a final example, consider the problem of separating spatially-aliased ground-roll from body waves in land data. This a more challenging application of the algorithm because the body waves have curvature that changes rapidly with both offset and time so to match it I need small filters in relatively small patches. The ground-roll, on the other hand, has little global curvature (although it may have strong local curvature due to aliasing) and matching it is more successful with large filters in large patches. A refinement to the method could use

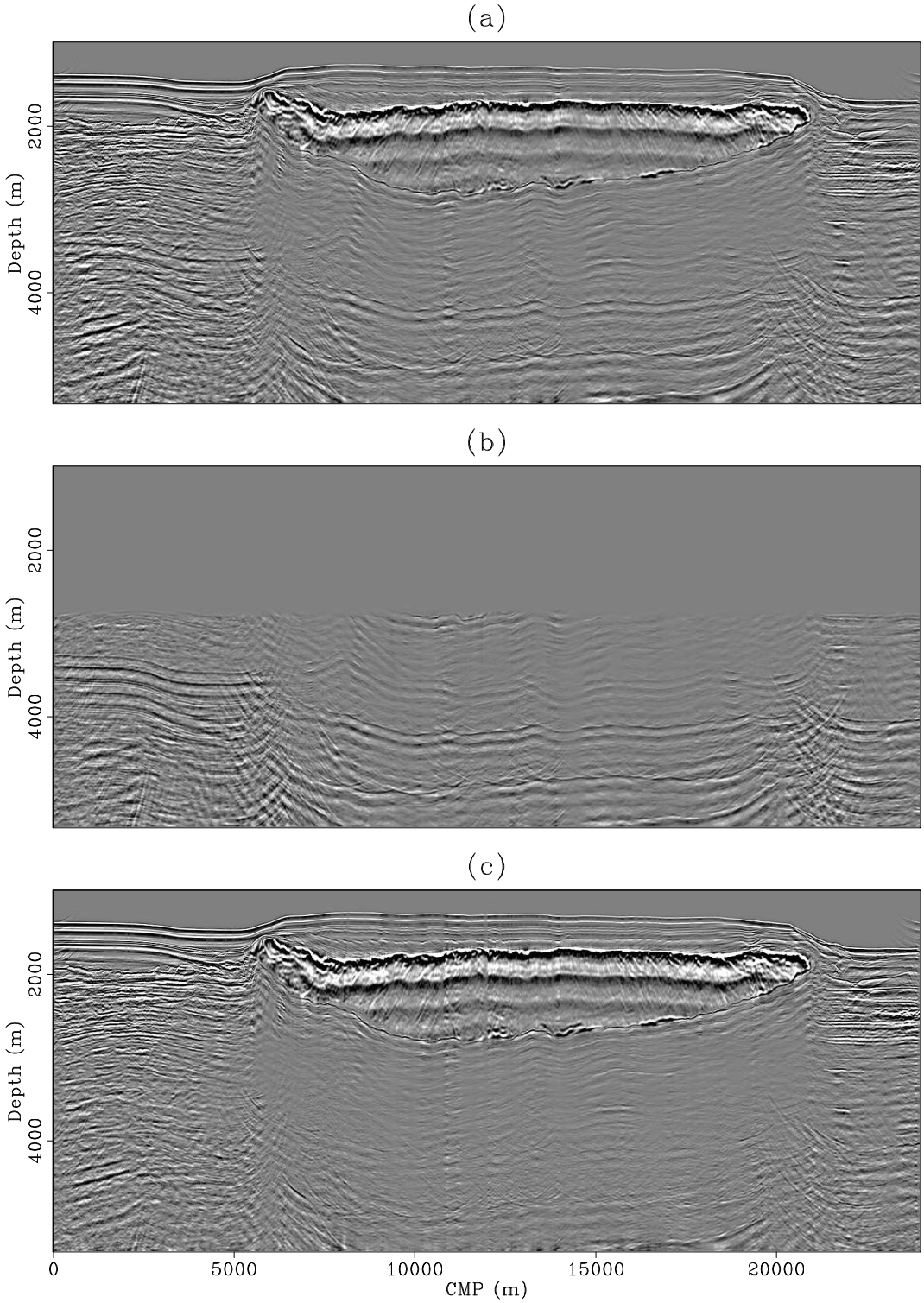


Figure 3.13: Comparison of angle stacks for the data (panel (a)), the initial estimate of the multiples (panel (b)) and the initial estimate of the primaries (panel (c)). adaptive-initial_stacks [CR]

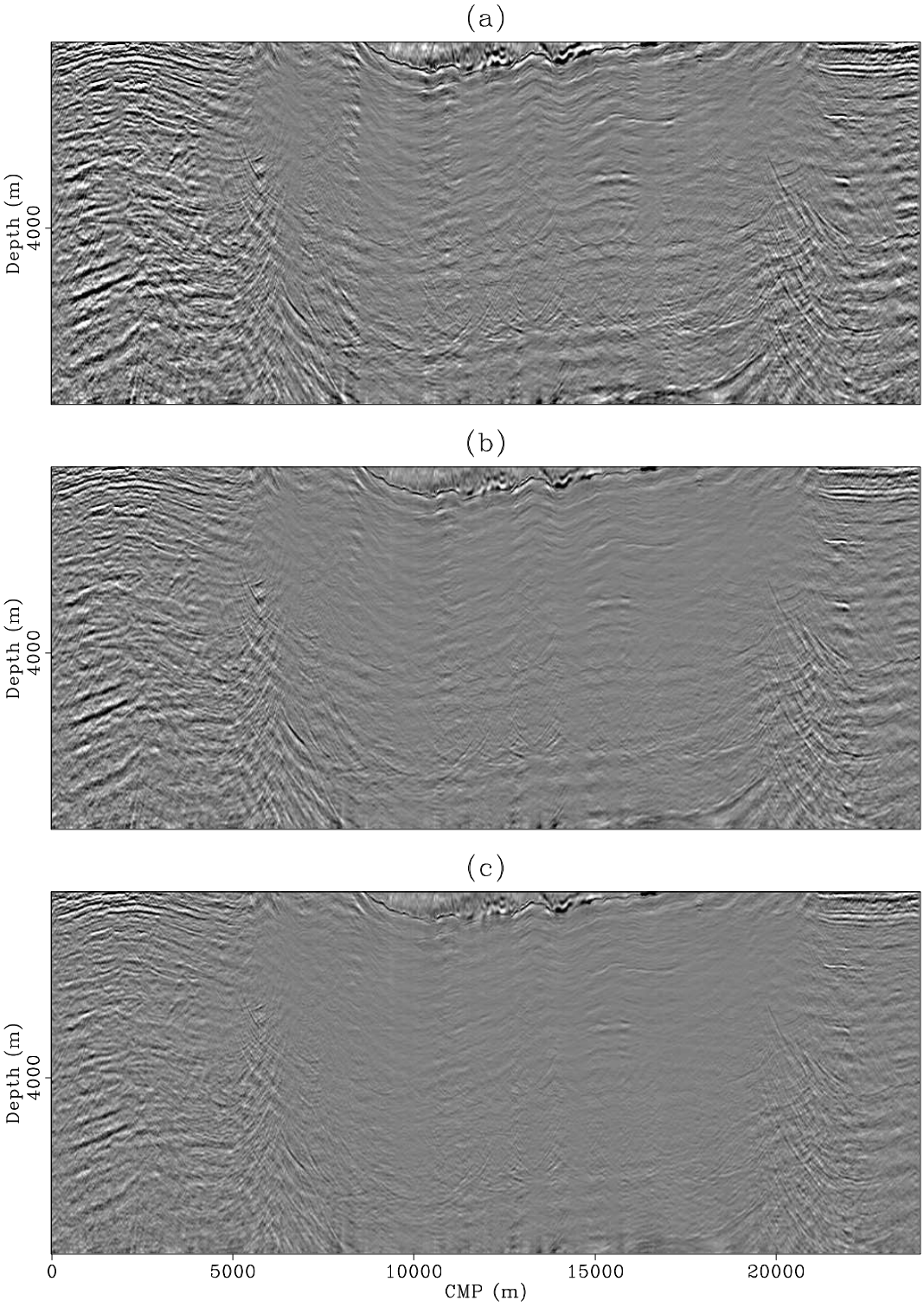


Figure 3.14: Comparison of windowed angle stacks for the initial estimate of the primaries (panel (a)), the estimate of the primaries after one outer iteration (panel (b)) and after five outer iterations (panel (c)). adaptive-matched_prim_stacks [CR]

different regularization operators or at least different regularization parameters $\epsilon$ on the non-stationary filters for the primaries and the multiples. For the sake of simplicity, I used the same regularization for both.

Figure 3.15 shows the original shot as well as the initial estimates of the body waves and the ground-roll. The ground-roll estimate was computed simply by high-cut filtering the data to 24 Hz using a Butterworth filter with six poles. I allowed significant energy from the body waves to leak into the estimate of the ground-roll to illustrate the problem described in the previous paragraph. Similarly, the estimate of the body waves was computed by low-cut filtering the data to 18 Hz also with a Butterworth filter with 6 poles. Since I don't want to reduce the low frequency components of the signal too much, I allowed strong ground-roll to leak into the estimate of the body waves. The purpose is to eliminate this ground-roll without hurting the signal and ideally, mapping back some of the body-waves from the estimate of the ground-roll.

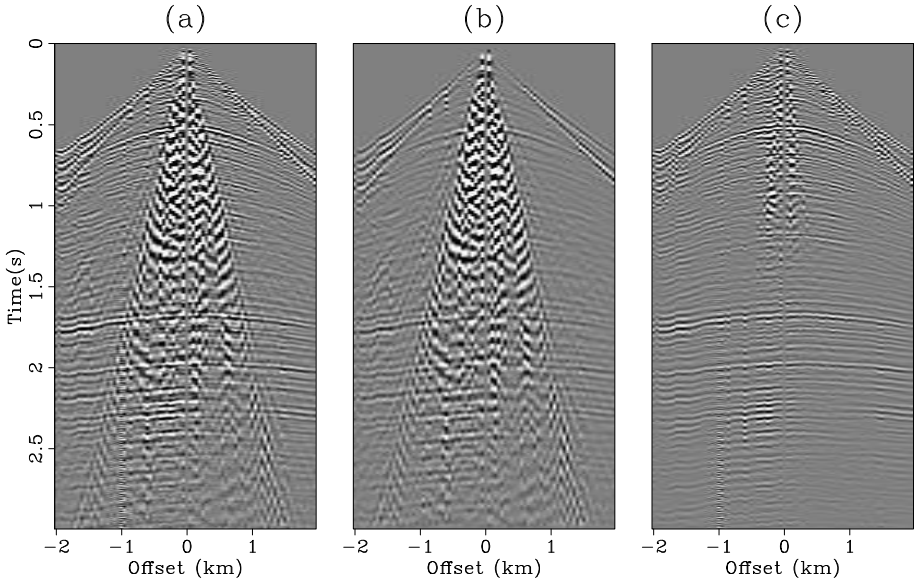


Figure 3.15: Land shot gather with strong ground-roll (a), initial estimate of ground-roll (b), and body waves (c). adaptive-shot1_estimates1 [ER]

Figure 3.16 shows the estimate of the body-waves after one, five and 10 outer iterations of the proposed algorithm. Even after just the first iteration, most of the ground-roll has been

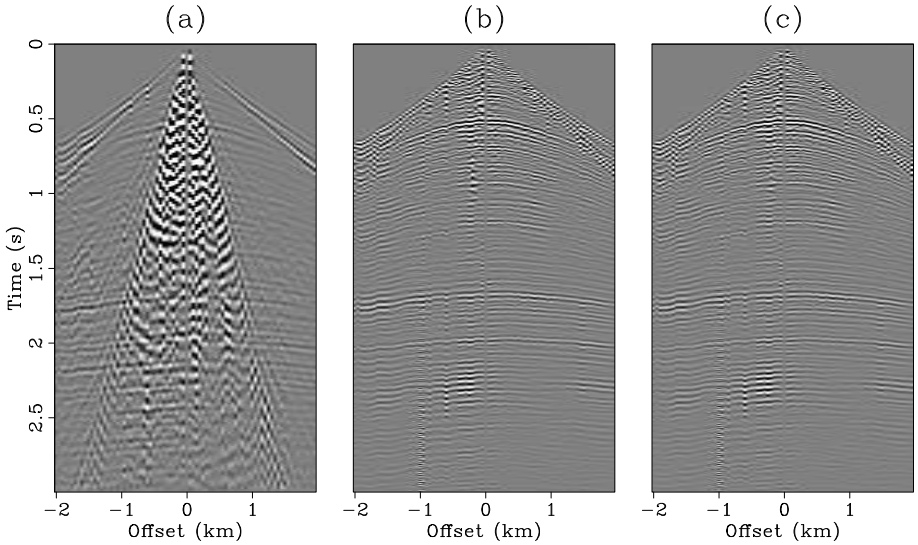


Figure 3.16: Estimate of body waves after one outer iteration (a), after 5 outer iterations (b) and after 10 outer iterations (c). Notice how after the fifth iteration the ground-roll is essentially gone. adaptive-shot1_matched_bw [ER]

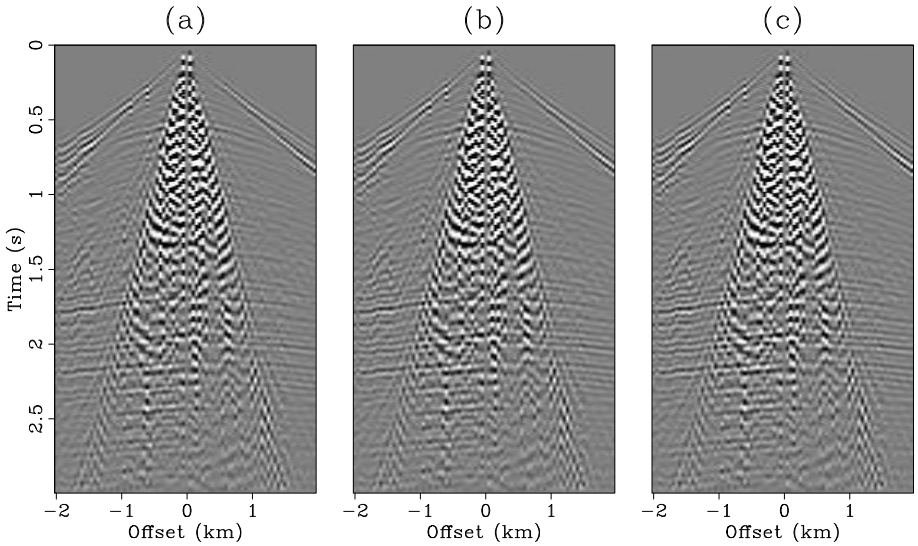


Figure 3.17: Estimate of ground-roll after one outer iteration (a), after 5 outer iterations (b) and after 10 outer iterations (c). Some of the body waves have been removed in panel (c) but much still remains. adaptive-shot1_matched_gr [ER]

eliminated and after five iterations it is almost gone. For this example I used just two patches in time and one in offset. Figure 3.17 shows similar results for the ground-roll. Since the patches were so large, the energy of the leaked body-waves were only slightly attenuated (see the reflector at about 1.7 secs). This energy was mapped back to the estimate of the body-waves.

## DISCUSSION AND CONCLUSIONS

The standard approach to match the estimated multiples directly to the data and obtain the primaries by subtraction of the matched multiples often leads to weakened primaries and/or contamination with residual multiples. By exploiting the estimates of both, multiples and primaries, we prevent the matching algorithm from attempting to match weak residual primaries along with the multiples. Furthermore, we obtain simultaneous estimates of both the primaries and the multiples that are guaranteed to be consistent with the original data.

As with most inversions, the performance of the algorithm depends critically on the choice of the inversion parameters. There are no guaranteed combinations of parameters that work in every case, but we now discuss the most important:

### Patch size

The size of the overlapping patches is a function of the non-stationarity of the data. Smaller patches represent rapidly changing data better but are more expensive and likely to match small patterns of correlated noise. For the examples on multiples we used patches that were just a few samples long (less than 10 in all axes). For the ground-roll example, we used patches 200 samples long in the time axis and 80 samples long in the offset axis.

### Non-stationary filter lengths

The length of the filter depends on the character of the noise model and the size of the patch. We found that, for matching the multiples, short filters (2 to 4 samples in each axes) worked

well but for the ground-roll example a longer filter gave better results (27 samples in time and 2 in offset) because the nature of the noise and the signal were so different.

### Balancing primaries and multiples

The parameter $\mu$ in Equation 3.1 can be used to give more relative weight to the estimates of the primaries or the multiples. In particular, setting it to zero reduces the algorithm to the more standard multiples-only matching. We found that this is not a critical parameter and a value of one works well and was used in all the examples in this paper.

### Regularization

As with any inversion problem, the choice of regularization is important to impose constraints of the admissible models. For the multiple matching problem, since the character of both the primaries and the multiples is similar, it is best to use the same regularization for estimating the primary and multiple non-stationary filters. In an example like the ground-roll attenuation, where the character of the signal and the noise is so different, it may be better to use different regularization operator $A$ (or at least a different level of regularization $\epsilon$) for the estimate of the two filter banks. We used the same regularization for the noise and the signal in all of our examples.

### Number of outer iterations

The algorithm tends to converge rather quickly, so only a few outer iterations are required (two or three) to get close to a reasonably good answer. For the ground-roll example 10 outer iterations were used.

It should be emphasized that the algorithm, as presented, is independent of the method employed to obtain the initial estimates of the multiples and the primaries. It should also be stressed that the algorithm does not rely on explicit knowledge of the moveouts of the primaries or the multiples. It only relies on the fact that the data is the sum of the multiples

and the primaries. The method can be used not only to match primaries and multiples but in general to match estimates of noise and signal to data containing both. I showed an example with the separation of ground-roll and body-waves with land data, but other applications may also be possible.

## ACKNOWLEDGEMENTS

I thank WesternGeco for providing the Gulf of Mexico dataset and the SMAART-JV consortium for providing the sigsbee model data.

# Chapter 4

# Mapping of 3D multiples to image space: Theory and synthetic data example.


**SUMMARY**

In Chapter 2 I showed that in 2D, specularly-reflected multiples, when migrated with the velocity of the primaries, map to subsurface offsets with the opposite sign to that of their surface offset in Subsurface-Offset-Domain Common-Image Gathers (SODCIGs). In Angle-Domain Common-Image Gathers (ADCIGs) they map with curvature towards increasing depths. In this chapter I extend these ideas to 3D and show, with a 3D synthetic prestack dataset, that specularly-reflected multiples in 3D have a similar behavior with an interesting addition: in 3D ADCIGs, the primaries and multiples exhibit different azimuth dependence as a function of the dip of the reflecting interface generating the multiple. This attribute is used to discriminate between primaries and multiples in 3D ADCIGs and therefore help in the attenuation of the multiples.

## INTRODUCTION

Given the relative simplicity of the Radon method applied in the image space, as shown in chapter 2, extending its application to account for the effect of crossline offset seems attractive. The first step in that direction is to understand the moveout of the multiples on 3D Subsurface-Offset-Domain Common-Image Gathers (SODCIGs) and Angle Domain Common Image Gathers (ADCIGs). In 3D, the ADCIGs are function of the aperture angle and the reflection azimuth (Biondi and Tisserant, 2004).

I show in this chapter that the residual moveout equation of a 3D specular water-bottom multiple from a flat water-bottom in 3D ADCIGs is a direct extension of the 2D equation presented in Chapter 2 after a simple rotation of coordinates to account for the source-receiver azimuth. The raypath of the specular water-bottom multiple in this case is confined to one vertical plane and is therefore essentially a 2D multiple. For a water-bottom that dips in the inline direction only, the raypath of the multiple is contained in a vertical plane only if the source-receiver azimuth is in the inline direction. For other directions, and for all directions if the water-bottom dips in the crossline direction, however, the propagation of the multiple is not contained in a plane.

In this chapter I concentrate on the mapping of the multiples to image space and leave their attenuation for later chapters. I will illustrate the mapping of the water-bottom multiple from a water-bottom dipping in the crossline direction using a very simple 3-D synthetic prestack dataset provided by ExxonMobil.

## 3D ADCIGS

The mathematical formalism and the methodology for computing 3D ADCIGs as a function of the aperture angle $\gamma$ and the reflection azimuth $\phi$ was given by Biondi and Tisserant (2004). They showed that for the primaries the ADCIGs as a function of the aperture angle, for a fixed reflection azimuth, is flat only for those aperture angles that illuminate the reflector at that reflection azimuth and appear to have curvature at other aperture angles even if the migration was carried out with the correct migration velocity field. I will show that for the multiples the

3D ADCIGs are not flat as a function of aperture angle for fixed azimuth angles. Instead, they exhibit a residual moveout curve similar to that of 2D multiples that I showed in Chapter 2.

## KINEMATICS OF 3D MULTIPLES IN IMAGE SPACE

I will first consider the simplest case of a flat water bottom. The residual moveout equations for both SODCIGs and ADCIGs will be the basis for the design of the Radon kernel in the same way as for the 2D case in Chapter 2.

### Flat water-bottom

Figure 4.1 shows a sketch of a specular water-bottom multiple from a flat water-bottom. The inline direction is oriented in the $x$ direction and the crossline direction in the $y$ direction. Because both the surface and the water-bottom are flat, the multiple reflection happens entirely in the vertical plane directly below the source-receiver line as is intuitively obvious. Following the discussion in chapter 2, the inline and crossline subsurface offsets of the multiple ($h_{\xi_y}$ and $h_{\xi_y}$) are, respectively:

$$\begin{aligned} h_{\xi_x} &= (1-\rho^2)\frac{h_{D_x}}{2} = (1-\rho^2)\frac{h_D\cos\phi}{2} \\ h_{\xi_y} &= (1-\rho^2)\frac{h_{D_y}}{2} = (1-\rho^2)\frac{h_D\sin\phi}{2} \end{aligned}$$

where $h_{D_x}$ and $h_{D_y}$ are the components of the surface offset vector in the inline and crossline directions, and $\phi$ is the azimuth of the source-receiver line with respect to the inline direction.

The travelpath of the multiple itself is azimuthally invariant and so the depth of the image point $z_\xi$ and its location are the same as in chapter 2 (equations 2.17 and 2.18). The residual moveout equations of the multiple in the inline and crossline directions are given by slightly

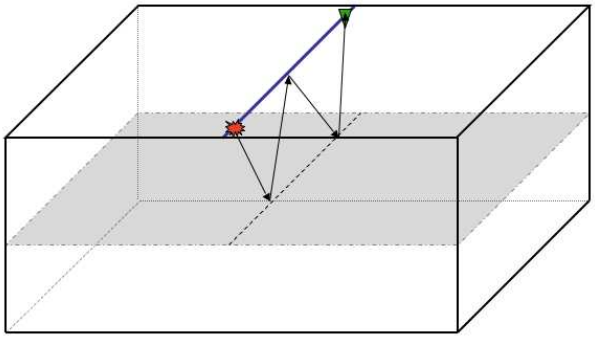

Figure 4.1: Raypath for a 3D Water-bottom multiple from a flat water-bottom. The multiple propagation is entirely contained in a vertical plane. 3dsynth-3d_mul_sktch1 [NR]

modified versions of equation 2.19:

$$z_{\xi_x} = \frac{z_\xi(0)}{1+\rho} + \rho\sqrt{\left(\frac{z_\xi(0)}{1+\rho}\right)^2 + \frac{h_{\xi_x}^2}{(1-\rho^2)\cos^2\phi}} \tag{4.1}$$

$$z_{\xi_y} = \frac{z_\xi(0)}{1+\rho} + \rho\sqrt{\left(\frac{z_\xi(0)}{1+\rho}\right)^2 + \frac{h_{\xi_y}^2}{(1-\rho^2)\sin^2\phi}}. \tag{4.2}$$

Notice that the azimuthal invariance of the depth and spatial location of the image means that, in terms of the subsurface offset magnitude and reflection azimuth (which for a flat reflector equals the surface azimuth), the residual moveout of the multiple in the SODCIG is exactly the same as in the 2D case of chapter 2. Figure 4.2 shows the inline SODCIG (panel (a)) taken at zero crossline offset and the crossline SODCIG (panel (b)) taken at zero inline offset. The data was modeled directly in CMP gathers and therefore is completely regular in inline and crossline surface offsets. I modeled both positive and negative crossline surface offset and hence the residual moveout of the multiple spans both positive and negative subsurface offsets.

**Dipping water-bottom**

In the previous section I discussed the simple model of a flat water-bottom. The extension of the residual moveout equations of the water-bottom multiple from 2D to 3D was trivial in that case. But what happens when the water-bottom has dip? Consider first the simpler case of dip in the inline direction only. The propagation of the water-bottom multiple is contained in the vertical $(x,z)$ plane (recall that in my convention the crossline direction is along the $y$ axis)

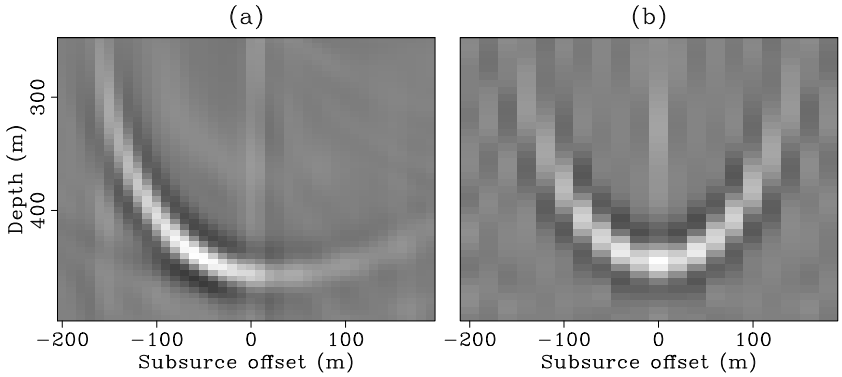


Figure 4.2: SODCIG for a water-bottom multiple from a flat water-bottom. Panel (a) is the inline subsurface offset gather at zero crossline subsurface offset and panel (b) is the crossline subsurface offset gather at zero inline subsurface offset. 3dsynth-sodcig [CR]

only for those source-receiver combinations whose azimuth is along the $x$ direction as shown in Figure 4.3.

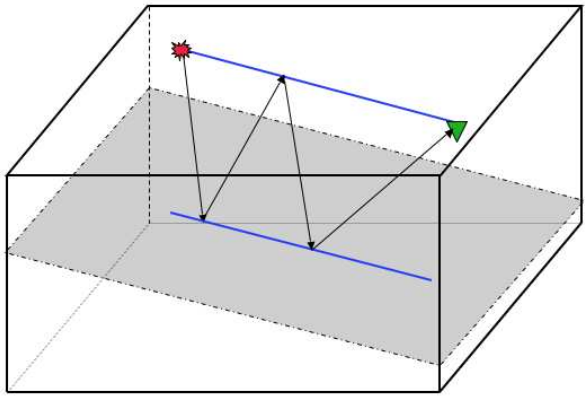

Figure 4.3: Raypath for a 3D water-bottom multiple from a water-bottom dipping in the inline direction only. The multiple propagation is entirely contained in a vertical plane only when the source-receiver azimuth is along the inline direction. 3dsynth-3d_mul_sktch2 [NR]

For all other source-receiver azimuths and for water-bottom with crossline dip, the multiple reflection path can no longer be considered a simple extension of the 2D case via a rotation of coordinates. The ray from the source to the reflector to the surface is contained in the plane normal to the reflector as required by Snell's law. On the other hand, the ray from the bounce point at the surface to the reflector to the receiver cannot be contained in the same plane since the surface is flat and therefore its normal is vertical. This reflection has to be contained in a vertical plane. This means that the surface bounce cannot lie in the line that joins the source

and the receiver (see Figure 4.4). The coordinates of the bounce point at the surface, the coordinates of the reflection points on the water-bottom and the traveltime of the multiple can be computed with the equations given by Ross et al (1999).

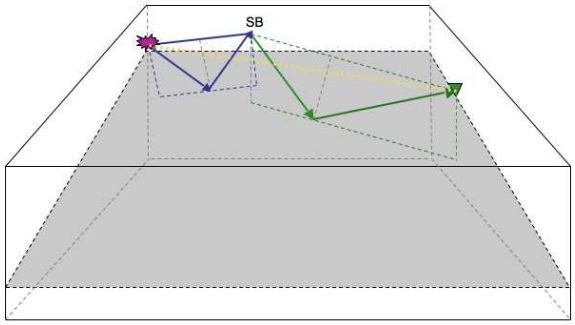


Figure 4.4: Raypath for a 3D Water-bottom multiple from a water-bottom dipping in the crossline direction only. The multiple propagation is not entirely contained in one plane. The ray from the source to the reflector to the surface bounce (SB) define one plane while the ray from the surface bounce to the reflector to the receiver is contained in a different plane. 3dsynth-3d_mul_sktch3 [NR]

Rather than attempting to derive convoluted equations for the residual moveout of the 3D multiples in SODCIGs or ADCIGs that could never be used in any reasonably practical Radon kernel, I will use the simpler equations for the flat water-bottom as I did for the 2D case in Chapter 2. In order to analyze the mapping of a crossline-dipping water-bottom multiple to image space, I will use a 3D prestack synthetic dataset provided by ExxonMobil.

## DESCRIPTION OF THE SYNTHETIC DATA

The velocity model used to generate the synthetic data is shown in Figure 4.5. The water bottom is deep, flat in the inline direction and dipping at 15 degrees in the crossline direction. The only reflector is a plane dipping 3 degrees in the inline direction and 15 degrees in the crossline direction.

The acquisition geometry consists of 10 receiver lines, each with 240 receivers spaced 25 m, with the first receiver at an inline offset of 100 m from the source. The maximum inline offset is therefore 6075 m. The receiver line separation is 100 m and the source is flip-flop with the two sources separated 50 m in the crossline direction and centered between the two

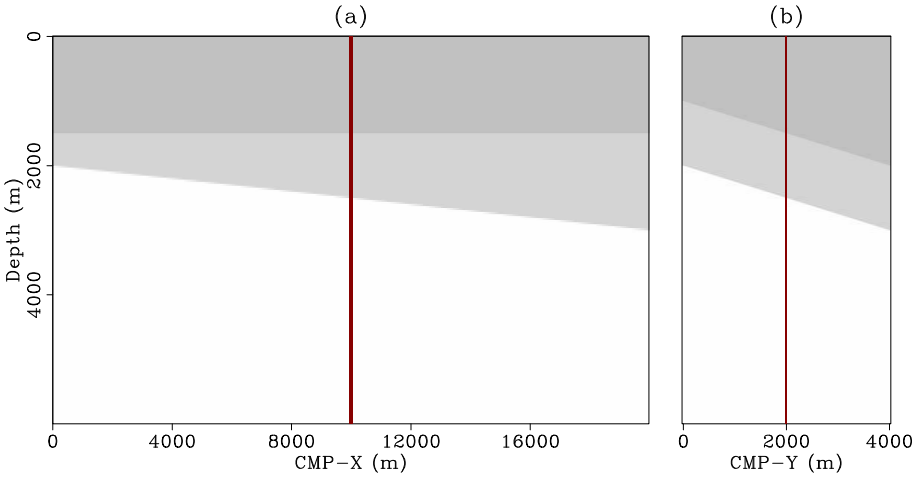


Figure 4.5: 3-D velocity model. Panel (a) is the inline section taken at CMP-X=2000 m and panel (b) is the crossline section taken at CMP-Y=10000 m. The water-bottom dips in the crossline direction only. The reflector dips gently (3 deg) in the inline direction as well. 3dsynth-model_vel [CR]

middle streamers. There are a total of 6 sail lines with each sail line separated from the next by a crossline distance of 450 m. With this arrangement, the crossline fold is just one and the fold in the inline direction is 60. Figure 4.6 shows a schematic of two adjacent sail lines illustrating that there is no overlap between the CMP coverage of each sail line. Figure 4.7 shows the receiver map, the source map, the azimuth-offset distribution and the fold map, all typical of a dual source acquisition.

Figure 4.8 shows a typical common source record with the 10 receiver lines plotted side-by-side. There are four reflections: the water-bottom primary, the deeper reflector primary, the water-bottom multiple and the peg-leg multiple between the water-bottom and the deeper reflection. Notice the change in polarity of the multiples compared to the primaries. Figure 4.9 shows a close up of the wavelet and the wavelet spectrum which shows that the wavelet has a DC component.

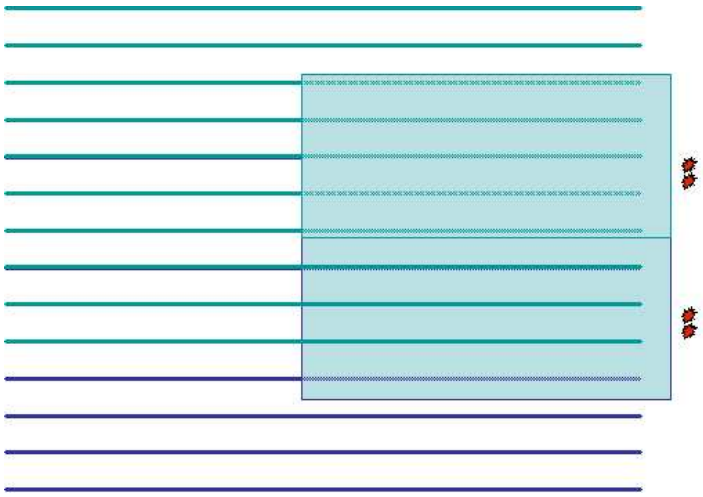

Figure 4.6: Schematic of fold coverage of two adjacent sail lines. 3dsynth-sketch2 [NR]

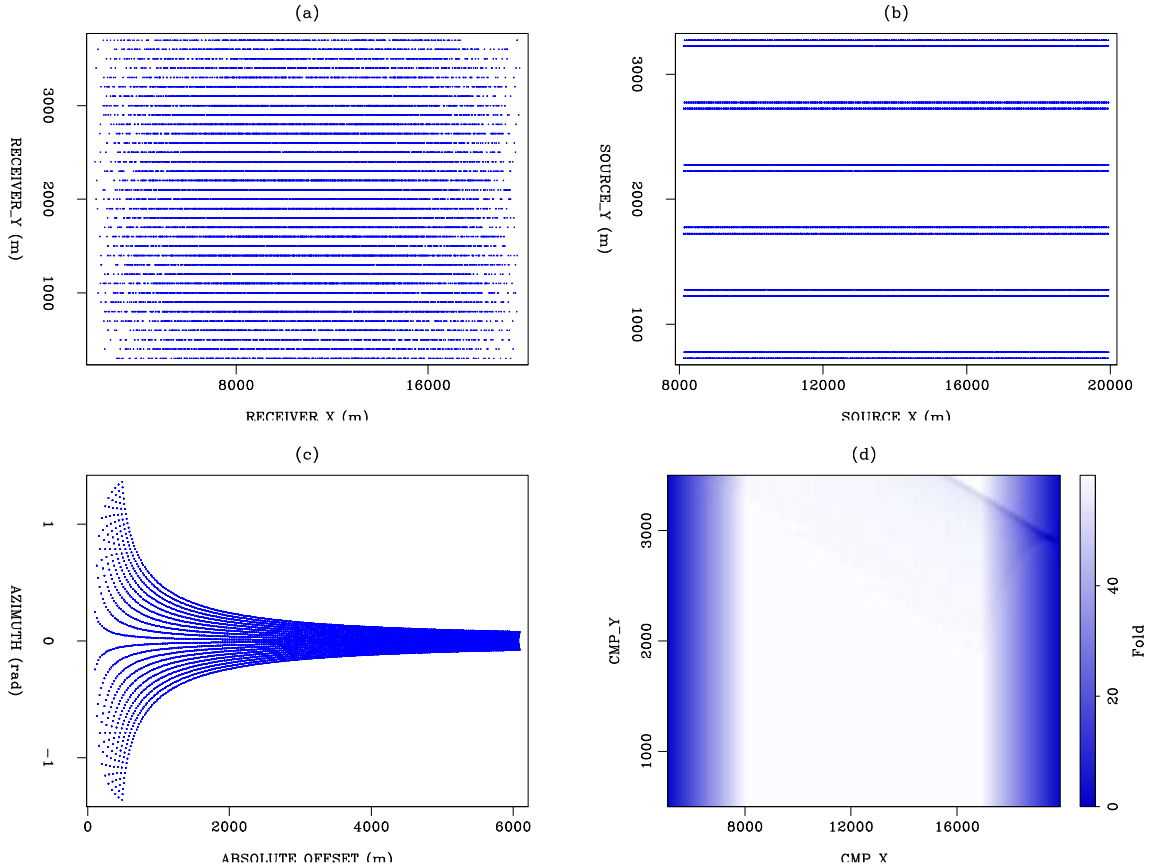


Figure 4.7: Top left: receiver map. Top right: source map. Bottom left: azimuth-offset distribution. Bottom right: fold map. 3dsynth-attributes [CR]

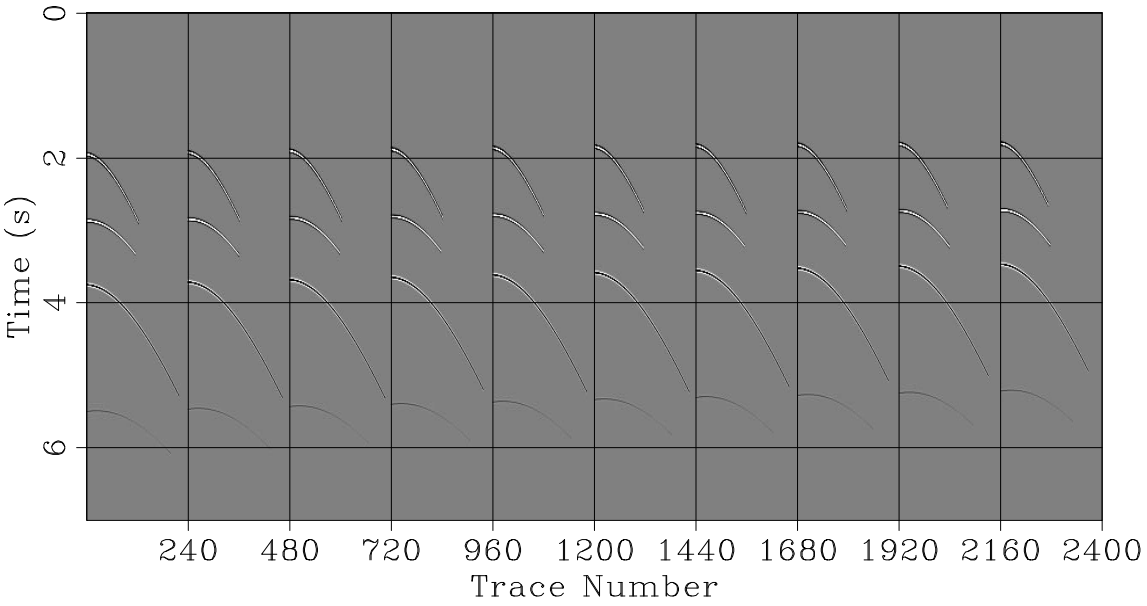


Figure 4.8: A typical "shot" gather showing the 10 receiver lines. Notice the polarity inversion of the multiples. 3dsynth-shot [CR]

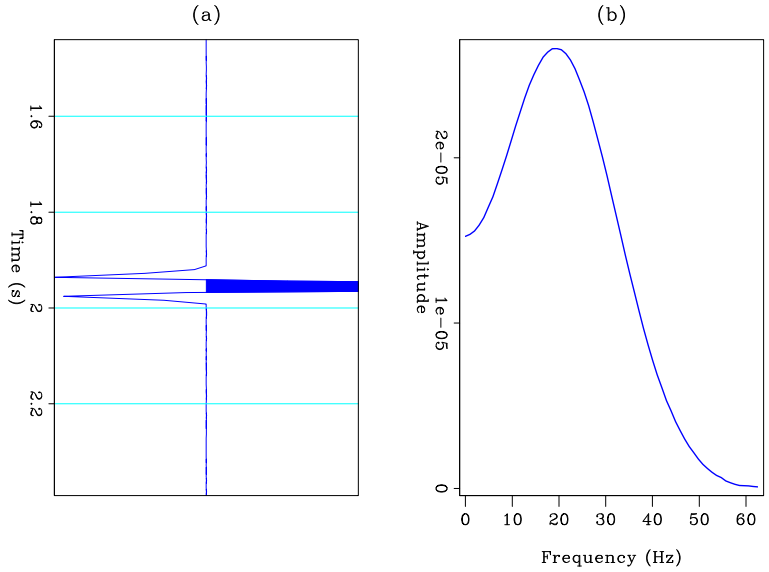


Figure 4.9: Close up of the seismic wavelet (a) and its frequency spectrum (b). Notice the uncharacteristic presence of low frequencies usually absent in field data. 3dsynth-spectrum [CR]

## DATA SUBSET FOR S-R MIGRATION

The original dataset contains 6,764,207 traces (about 44 GB). Choosing a small, meaningful, "complete" five-dimensional subset of data for source-receiver migration is not trivial, because the acquisition geometry makes the offset distribution of adjacent CMPs different in both inline and crossline directions. This is illustrated in Figure 4.10 which shows the offset distribution inline for a few adjacent CMPs. The offset distribution repeats only every fourth CMP. Although not shown, the situation in the crossline direction is worse. There are 20 different crossline offsets (from -475 to 475 m), but for any CMP line taken at a fixed crossline position, all traces correspond to the same crossline offset.

The input to the source-receiver migration algorithm is a regular 5-D cube $D(t, \mathbf{m}, \mathbf{h})$, where $\mathbf{m}$ is the vector of surface position, $\mathbf{h}$ is the vector of surface offsets and $t$ is the traveltime. In order to create such a cube, even for a small dataset, a large number of null traces need to be inserted. For example, for a 4 by 4 km square of full-fold CMP data, we have: 51200 CMPs (at 12.5 by 25 m bin) each with 240 inline offsets (100 to 6075 m at 25 m sampling) and 20 crossline offsets (-475 to 475 m at 25 m sampling) for a total of 440 million traces. Since each trace has 1751 samples (7 seconds at 4 ms sampling interval), this means a dataset of almost 800 GB.

In order to make a more manageable dataset, further data reduction is necessary. Here I am particularly interested in the effect of crossline dip in the moveout of the multiples after migration, therefore I chose to subsample the data in the inline coordinates only. I subsampled the inline CMP axis such that every other CMP was discarded. This has the advantage of not only halving the number of CMPs but also halving the number of inline offsets as can be seen in Figure 4.10 since now the inline offset interval is 50 m rather than 25 m. I also subsampled the time axis to 16 ms, which required that the data be filtered to a maximum frequency of 32 Hz. The original wavelet had frequencies up to about 60 Hz as illustrated in Figure 4.9. High-cut filtering is acceptable in this case because vertical resolution is not critical for my purposes. I also limited the inline offsets to 4000 m which sacrifices the steeper flanks of the moveout of the multiples as shown in Figure 4.8. With these reductions, the dataset size becomes about 70 GB after some padding in all spatial directions to avoid or at least lessen

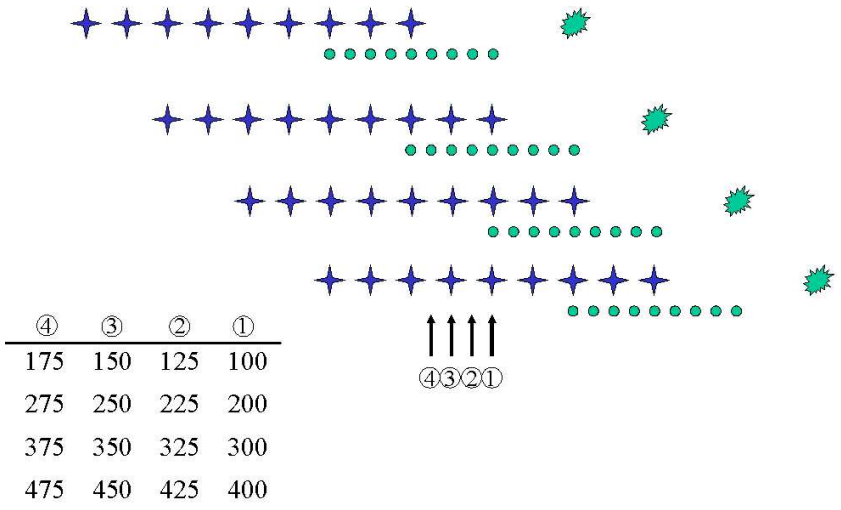


| ④ | ③ | ② | ① |
|---|---|---|---|
| 175 | 150 | 125 | 100 |
| 275 | 250 | 225 | 200 |
| 375 | 350 | 325 | 300 |
| 475 | 450 | 425 | 400 |

Figure 4.10: Schematic showing the unequal inline offset distribution of adjacent inline CMPs. The stars represent the receivers and the small circles represent the CMP positions. The table on the bottom left lists the inline offset distribution of a few traces corresponding to four arbitrary adjacent CMPs numbered 1 to 4 as indicated by the arrows. Notice that the adjacent CMPs have different inline offset distribution. 3dsynth-sketch3 [NR]

migration artifacts.

Figure 4.11 shows a near offset cube of the five-dimensional selected dataset. Notice that there are only six crossline CMPs for a given inline CMP location, corresponding to the six sail lines, and there is no data redundancy in the crossline direction. Similarly, only every other inline CMP position has a trace with a given crossline CMP location because of the dual shot geometry.

Panel (a) of Figure 4.12 shows the inline distribution of offsets for an inline CMP section taken at crossline CMP position 2212.5 and crossline offset of -12.5 m. Here again, note the on-off pattern of the offset distribution due to the dual shot source as indicated in the sketch in Figure 4.10. Similarly, panel (b) of Figure 4.12 shows the distribution of crossline offsets for a CMP section in the crossline direction taken at inline CMP location 8400 and inline offset of 100 m.

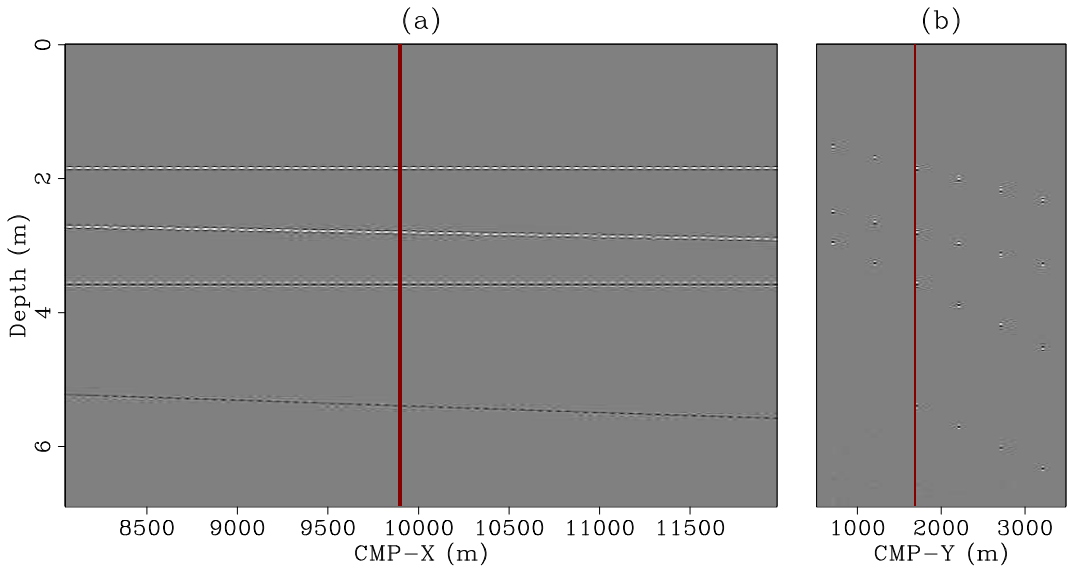


Figure 4.11: Near offset cube (100 m offset inline and -25 m offset crossline). Panel (a) is the inline section at CMP-Y=1712.5 m while panel (b) is the crossline section at CMP-X=9925 m. 3dsynth-zoff1 [CR]

## PREPROCESSING

Before attempting to do the full source-receiver migration on the data, I applied some preprocessing described briefly in this section.

### Data infill

The input data was first bandpass-filtered to remove the DC component and to limit the high frequencies to 32 Hz, and subsampled to 16 ms. It was then infilled with null traces in both offset dimensions, padded to add negative inline offsets (to allow room for the multiples after migration), padded to extend the crossline aperture, and sorted into a five dimensional regular cube of time, offsets and CMP coordinates.

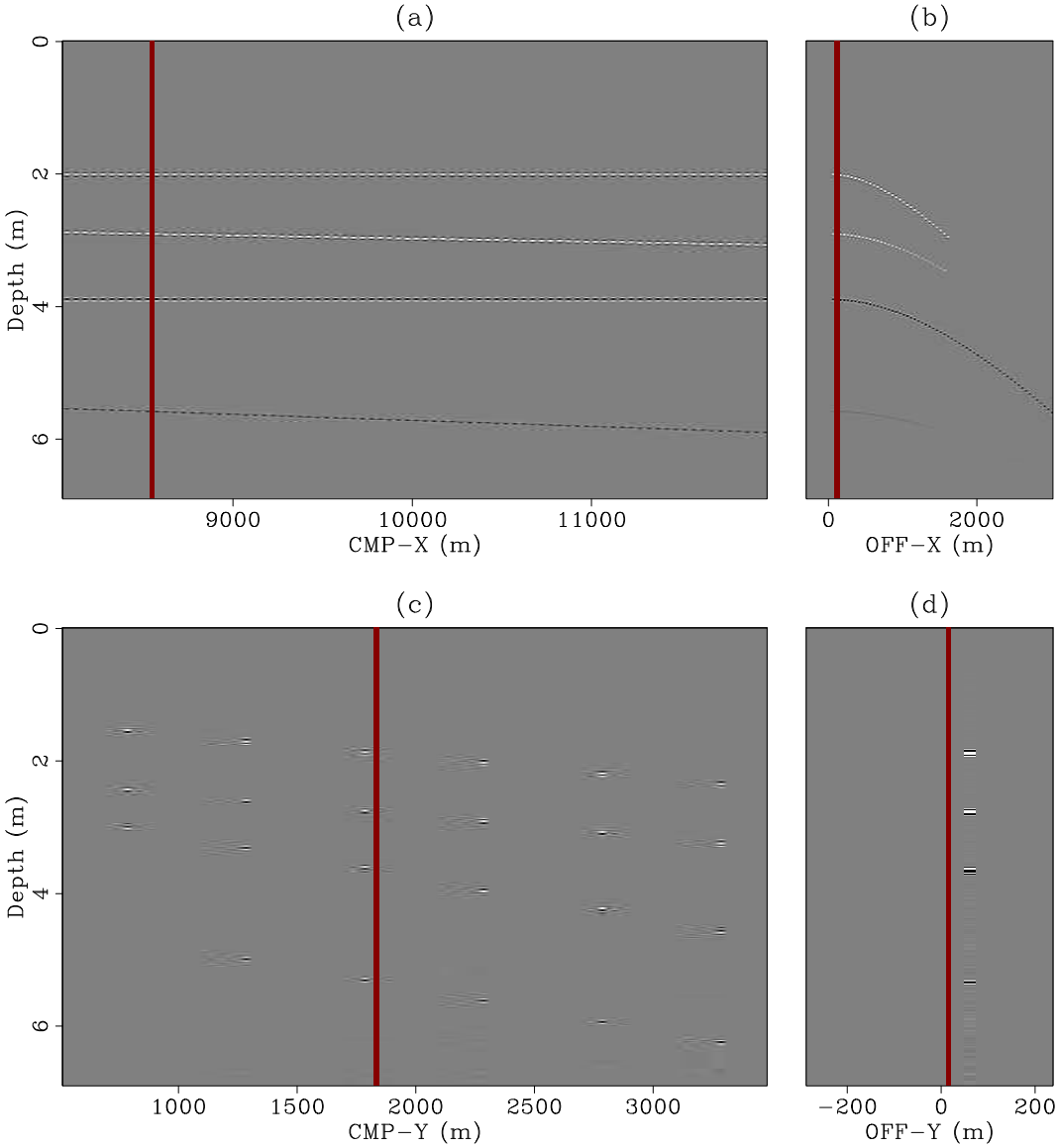


Figure 4.12: 3D data. Panel (a) is the inline section taken at 100 m inline offset, -25 m crossline offset and CMP-Y=-12.5 m. Panel (b) is the inline offset gather at CMP-X=8550 m, CMP-Y=-12.5 m and -25 m crossline offset. Panel (c) is the crossline section at CMP-X=8400 m, 100 m inline offset and 25 m crossline offset. Panel (d) is the crossline offset gather at CMP-X=8400 m, CMP-Y=1837.5 m and 100 m inline offset. Notice the data sparsity, especially in the crossline direction. 3dsynth-inline-xline [CR]

### Datuming

The regular cube was then datumed to just above the water-bottom to avoid spending migration time on downward continuation through the water layer. Figure 4.13 shows a comparison of one CMP 3D gather before (left) and after datuming (right). Notice that datuming not only saves propagation time but also allows a significant reduction of the data to be migrated because the offsets decrease as the recording surface is "moved" closer to the reflectors, making the positions of sources and receivers closer. Notice also that the holes in both offsets and CMPs have been healed by the propagation.

### Common-Azimuth Migration

In order to choose the key migration parameters such as depth step, number of frequencies and especially the minimum amount of padding of negative subsurface offsets needed to accommodate the migration of the multiples, I ran some tests using common-azimuth migration (Biondi and Palacharla, 1996). Figure 4.14 shows the inline dimensions (CMP and offset) of an SODCIG after common-azimuth migration. Notice that the multiples have been mapped to the negative subsurface offsets and to shallower depths, consistent with the results of Chapter 2.

## SOURCE-RECEIVER MIGRATION

After the data reduction afforded by the datuming and appropriate padding in offsets, I input to the source-receiver migration a very small dataset with only 32 CMPs in the inline direction, 144 CMPs in the crossline direction, 120 offsets in the inline direction, 24 offsets in the crossline direction and 200 frequencies. The data was migrated with 600 depth steps at 10 m (starting at the depth of the water-bottom at zero crossline CMP or about 1000 m).

Figure 4.15 shows the inline dimensions of one SODCIG. Again, note that the multiples migrate to the negative subsurface offsets and are well separated from the primaries, which map around zero subsurface offset.

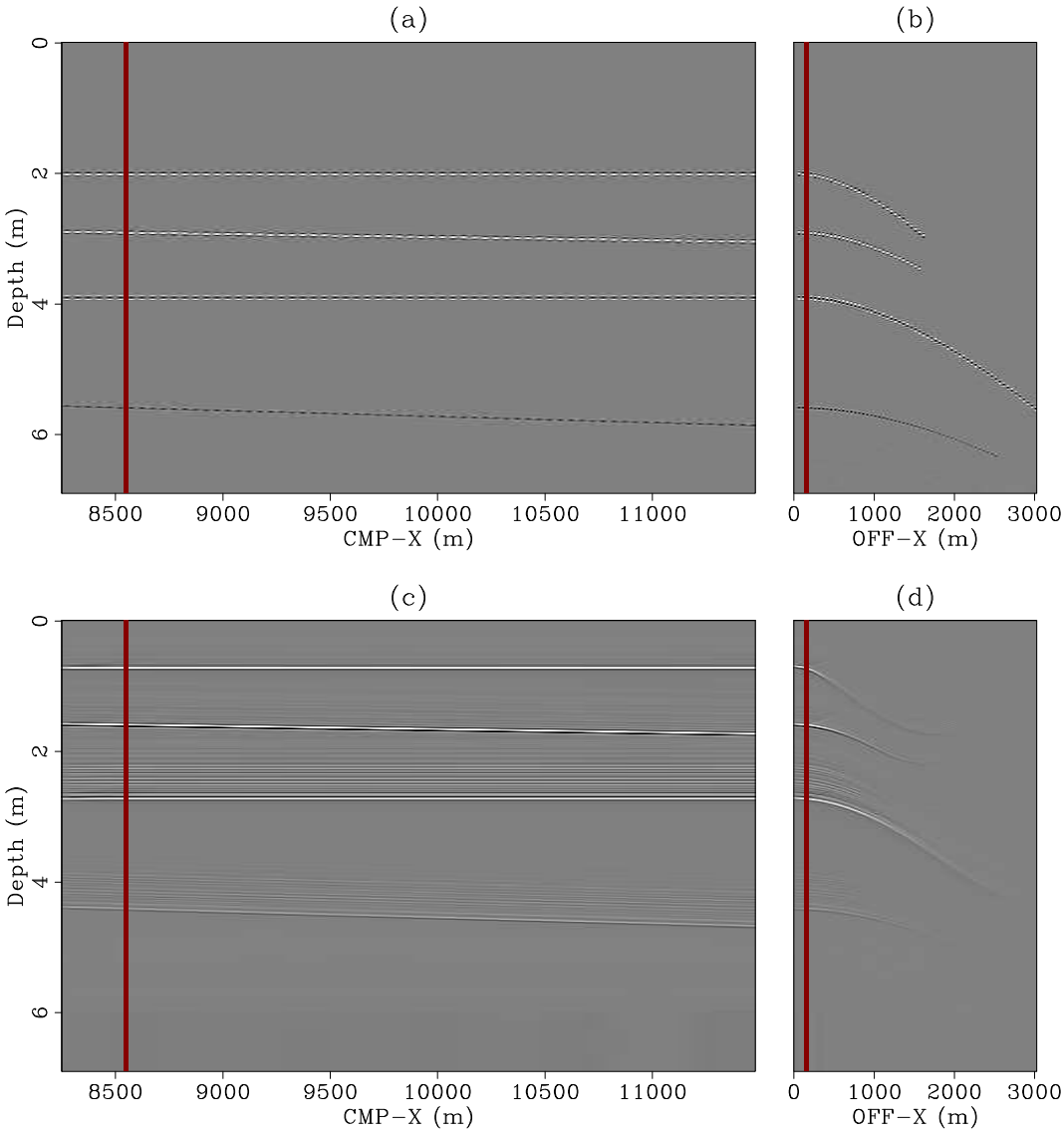


Figure 4.13: Before-after datuming comparison. Panels (a) and (c) correspond to the inline CMP section at CMP-Y=-12.5 m, 150 m inline offset and -25 m crossline offset, before and after datuming, respectively. Panels (b) and (d) correspond to the inline offset gather at CMP-X=8550 m, CMP-Y=-12.5 m and -25 crossline offset, before and after datuming, respectively. Notice that the datuming, besides shifting the data upwards, also healed the holes in the acquisition and reduced the offset coverage. 3dsynth-datum_comp [CR]

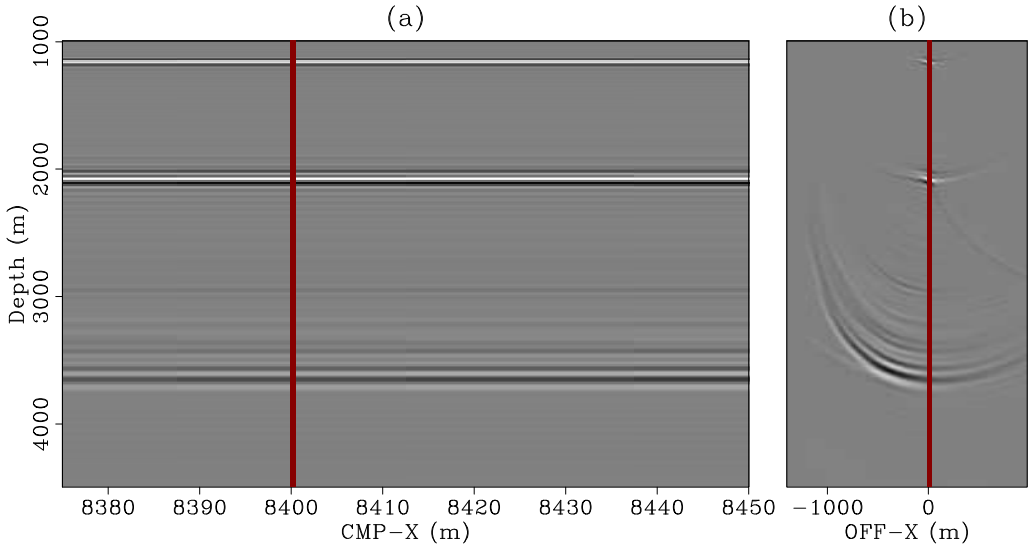


Figure 4.14: Common-azimuth migration. Panel (a) is the migrated inline section at CMP-Y=662.5 m, zero inline subsurface offset and -25 m crossline subsurface offset. Panel (b) is the inline subsurface offset gather at CMP-X=8400 m, CMP-Y=662.5 m and -25 m crossline subsurface offset. Notice in panel (b) how the multiple migrated towards the negative subsurface offsets. 3dsynth-cam1 [CR]

In contrast with the inline direction, the sampling of the crossline offsets and CMPs is very coarse and the results of the migration are not nearly as good. This is illustrated in Figure 4.16 which shows a cube of crossline CMPs as a function of crossline offset. Although the primaries have been relatively focused toward zero subsurface offset, there is still a lot of energy smearing to both positive and negative crossline subsurface offsets. Even worse, the multiple looks almost as focused as the primaries because of the lack of crossline data and insufficient crossline migration aperture.

Figure 4.17 shows a zero subsurface-offset cube of the migrated data. The image is good in the inline direction and somewhat noisy in the crossline direction. The large sparsity of the crossline offsets create migration artifacts.

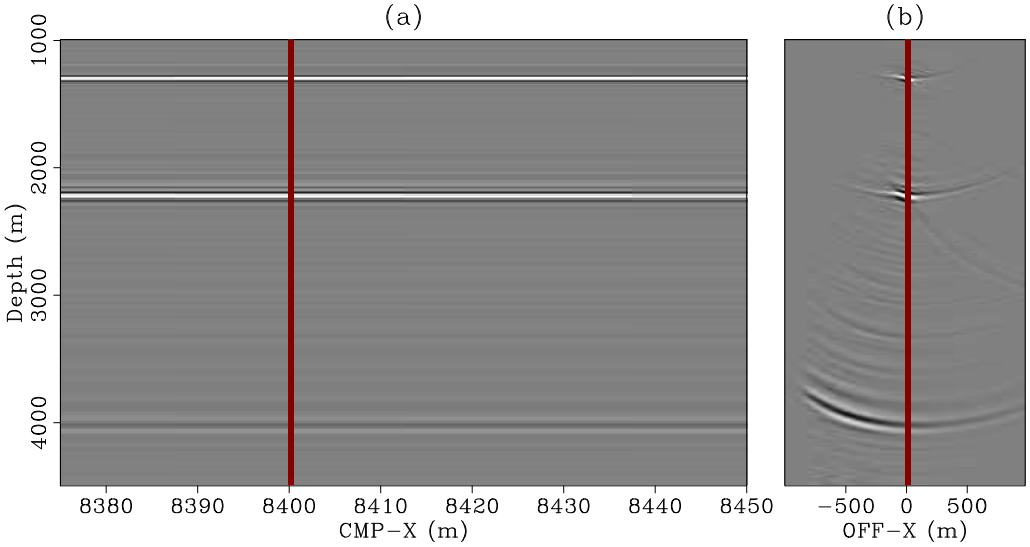


Figure 4.15: Source-receiver migration. Panel (a) is the migrated inline section at CMP-Y=1212.5 m, zero inline subsurface offset and 25 m crossline subsurface offset. Panel (b) is the inline subsurface offset gather taken at CMP-X=8400 m, CMP-Y=1212.5 m and 25 m crossline subsurface offset. Notice again how the multiple migrates toward the negative subsurface offsets. 3dsynth-pre3dmig1 [CR]

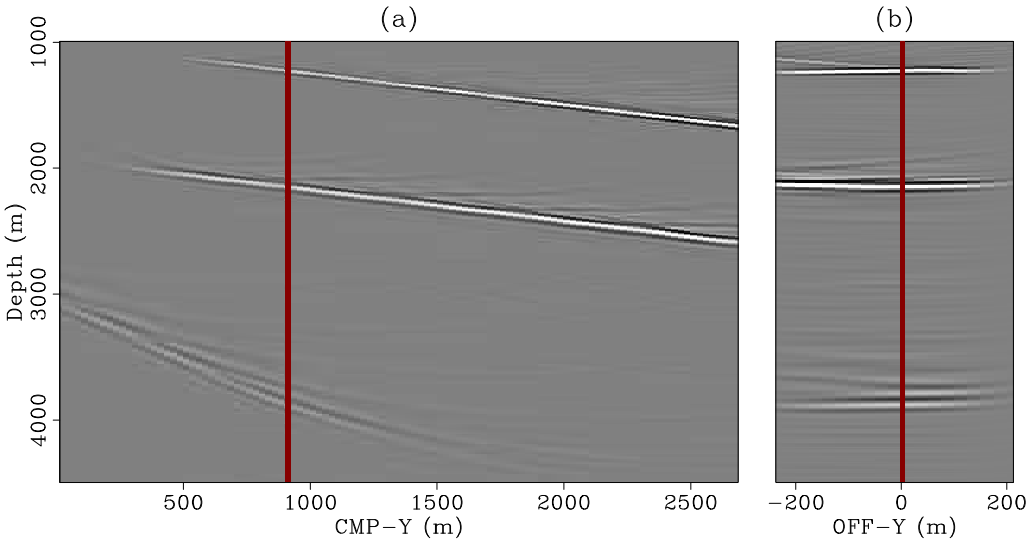


Figure 4.16: Source-receiver migration. Panel (a) is the migrated crossline section at CMP-X=8450 m, zero inline subsurface offset and zero crossline subsurface offset. Panel (b) is the crossline subsurface offset gather taken at CMP-X=8450 m, CMP-Y=912.5 m and zero inline subsurface offset. 3dsynth-pre3dmig3 [CR]

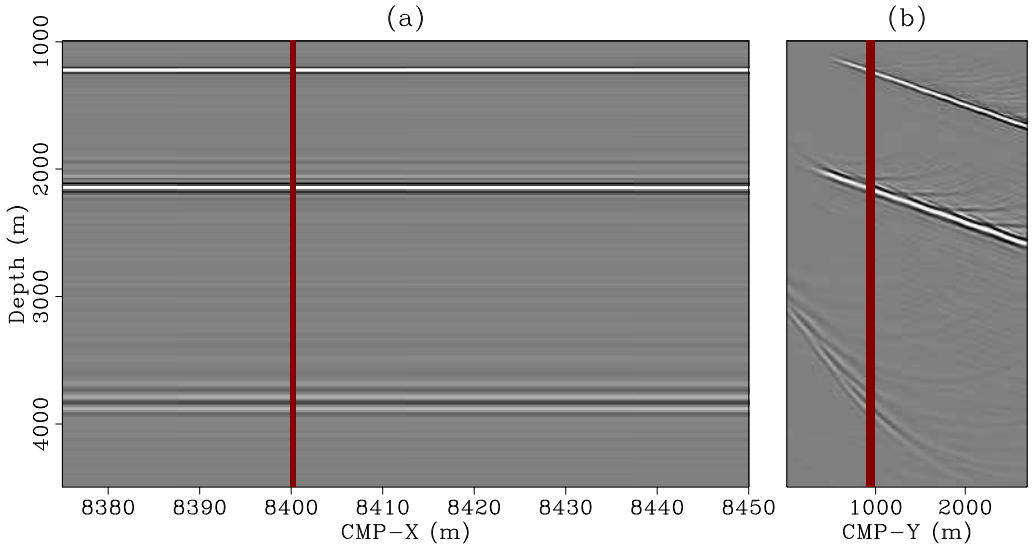


Figure 4.17: Source-receiver migration. Panel (a) is the migrated inline section at CMP-Y=912.5 m, zero inline subsurface offset and zero crossline subsurface offset. Panel (b) is the migrated crossline section at CMP-X=8400 m, zero inline subsurface offset and zero crossline subsurface offset. The image in the inline direction is good, but in the crossline direction has artifacts associated to the sparse sampling in that direction. 3dsynth-pre3dmig2 [CR]

## MAPPING TO 3D ADCIGS

In 3D angle gathers, the multiples and the primaries behave differently not only in terms of aperture angles but also in terms of reflection azimuth. For computational convenience, I first windowed the SODCIGs in depth and computed the ADCIGs for the water-bottom primary only. Panel (a) of Figure 4.18 shows the result for the ADCIG at CMP-X=8500 m and CMP-Y=837.5 m. It is flat for a given azimuth although the range of aperture angles as a function of the azimuth is limited. For zero aperture angle, by definition there is no azimuth resolution (the incident and reflected rays coincide) and therefore all azimuths are seen as equally likely to contribute to the image. Similarly, I windowed the water-bottom multiple and computed the ADCIG as shown in panel (b) of Figure 4.18. The depth slice shows different azimuth dependency compared with the primary. While the range of azimuths decrease with increasing aperture angle for the primary, it does not for the multiples (compare the two depth slices). As a function of aperture angle for a given azimuth, the multiple shows the expected over-migrated

residual moveout. At zero aperture angle there is no azimuth resolution.

It is interesting to analyze the angle gathers as a function of azimuth for different aperture angles. The water-bottom primary and the water-bottom multiple behave very differently as shown in Figures 4.19 and 4.20. For the primary, as the aperture angle increases, the angle gather as a function of azimuth becomes narrower as a consequence of the increase in azimuth resolution. For large enough aperture angles, the incident and reflected rays are no longer any where near co-linear and so nicely define a reflection plane whose azimuth is well defined (see panels (d) an (e)), except for an artifact due to insufficient padding when computing the ADCIG. For the multiple, as the aperture angle increases, the gather as a function of azimuth curves up because it is over-migrated. There is no similar increase in azimuth resolution because for the multiple there is not a clear notion of a reflection plane. Recall that, because of the crossline dip, the ray from the source to the reflector to the surface bounce point is contained in a plane normal to the reflector, whereas the ray from the bounce point to the reflector to the receiver is contained in a plane normal to the surface, that is, a vertical plane. The full multiple trajectory, from the source to the receiver, is therefore not contained on a single plane.

Another interesting piece of information that 3D angle gathers can give us is the range of aperture angles that are illuminated at a particular reflection azimuth angle. Figure 4.21 shows the angle gathers of the water-bottom primary as a function of aperture angle for five reflection azimuth angles: (a)-40, (b)-20, (c)0, (d)20 and (e)40 degrees. The moveout of the primary is flat for those aperture angles that are actually illuminated at the corresponding reflection azimuth. Given that both the water-bottom and the deep reflector dip in the same crossline direction, the reflection azimuth coverage is good in that direction but is poor in the opposite direction (positive azimuths with my sign convention). Notice that the angle gather may even curve down as if it were over-migrated for those reflection azimuths not actually illuminating the reflector. At first glance this is counter-intuitive, since the primary was migrated with the exact primary velocity (Biondi and Tisserant, 2004). The curvature is due to poor illumination and not to velocity errors.

Similarly, Figure 4.22 shows the corresponding gathers for the water-bottom multiple reflection. Unlike the primary, the multiple shows residual curvature at all azimuths. Not only

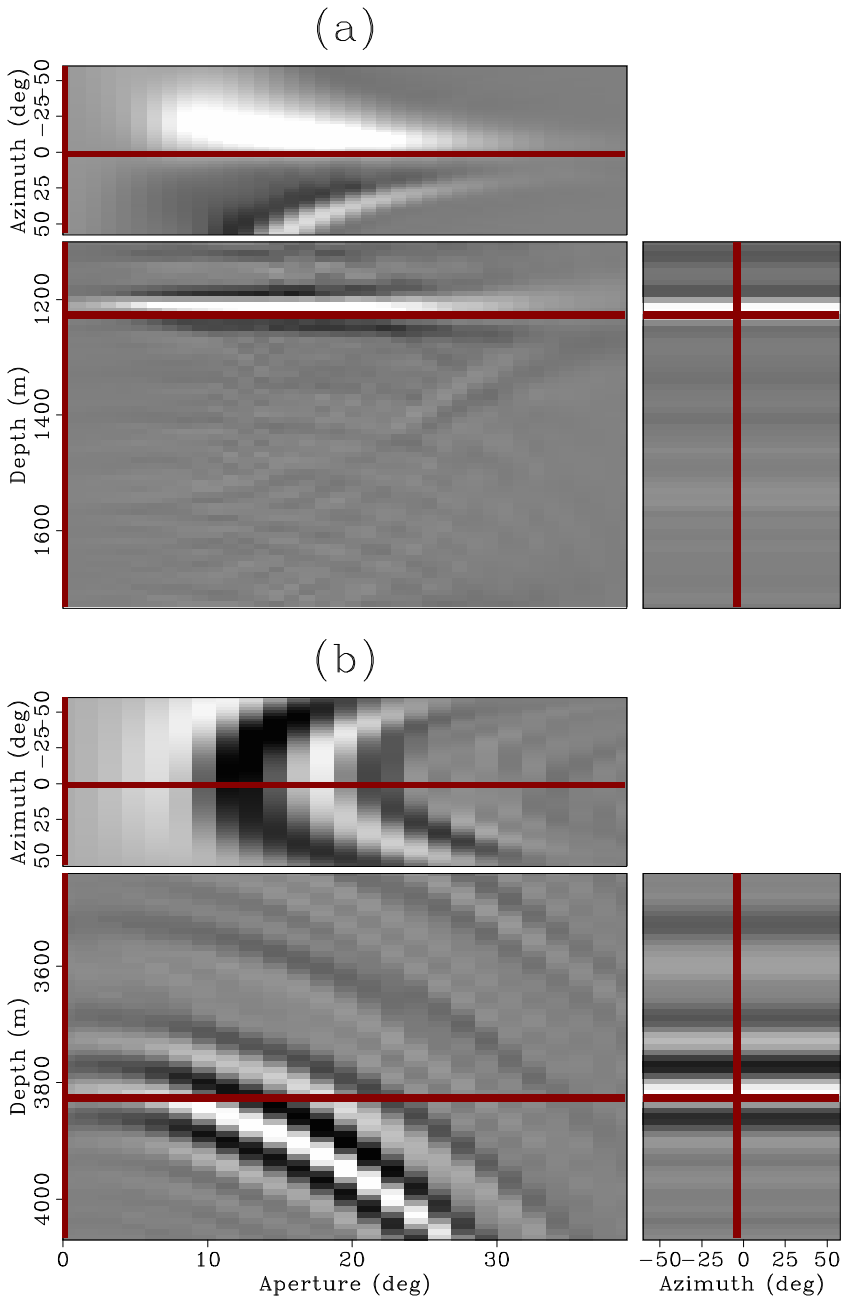


Figure 4.18: 3D ADCIG at CMP-X=8500 m and CMP-Y=837.5 m for the water-bottom primary (a) and the water-bottom multiple (b). The depth slice is taken at the depth of the primary (1220 m) in panel (a) and at the depth of the multiple (3840 m) in panel (b). The primary was correctly migrated and therefore its moveout is flat. The multiple was over-migrated and so exhibits residual moveout as a function of the aperture angle. 3dsynth-3dadcigs [CR]

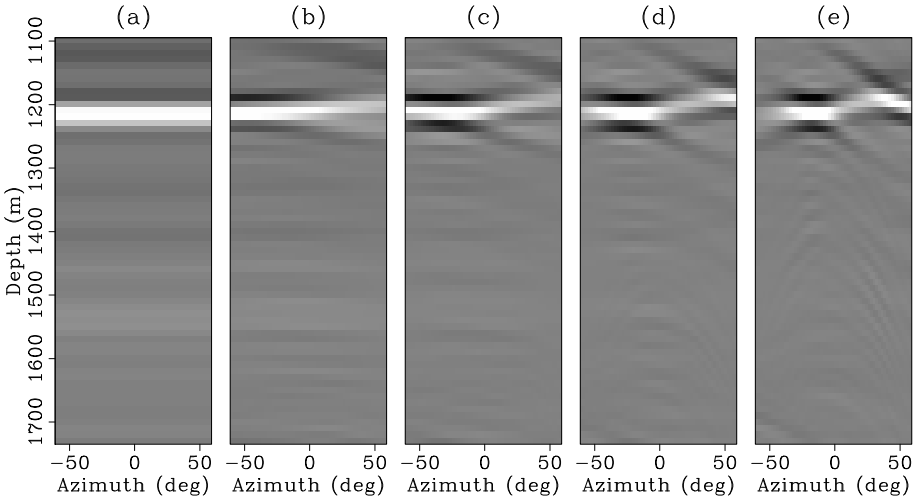


Figure 4.19: 3D ADCIG for the primary water-bottom reflection as a function of azimuth. The different panels correspond to different aperture angles: (a) 0, (b) 5, (c) 10, (d) 15 and (e) 20 degrees. As the aperture angle increases, the azimuth resolution increases as well. 3dsynth-az_gath1 [CR]

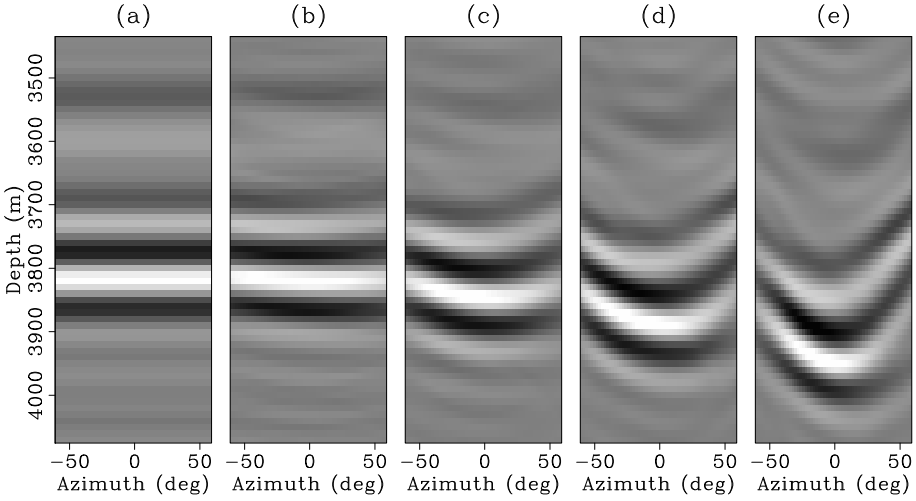


Figure 4.20: 3D ADCIG for the water-bottom multiple reflection as a function of azimuth. The different panels correspond to different aperture angles: (a) 0, (b) 5, (c) 10, (d) 15 and (e) 20 degrees. As with the primaries, there is no azimuth resolution at zero aperture angle. In contrast to the primary, however, the azimuth resolution does not increase with increasing aperture angle. 3dsynth-az_gath2 [CR]

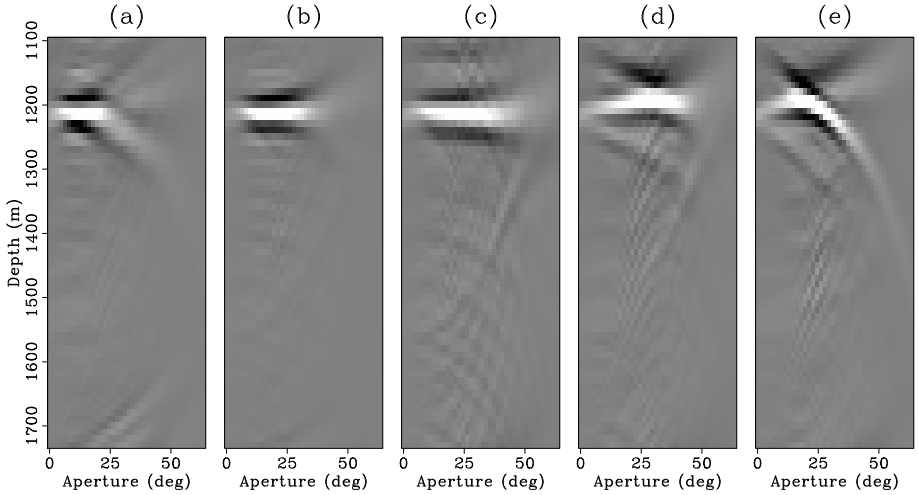


Figure 4.21: 3D ADCIG for the primary water-bottom reflection as a function of aperture angle. The different panels correspond to different reflection azimuth angles: (a)-40, (b)-20, (c)0, (d)20 and (e)40 degrees. 3dsynth-ap_gath1 [CR]

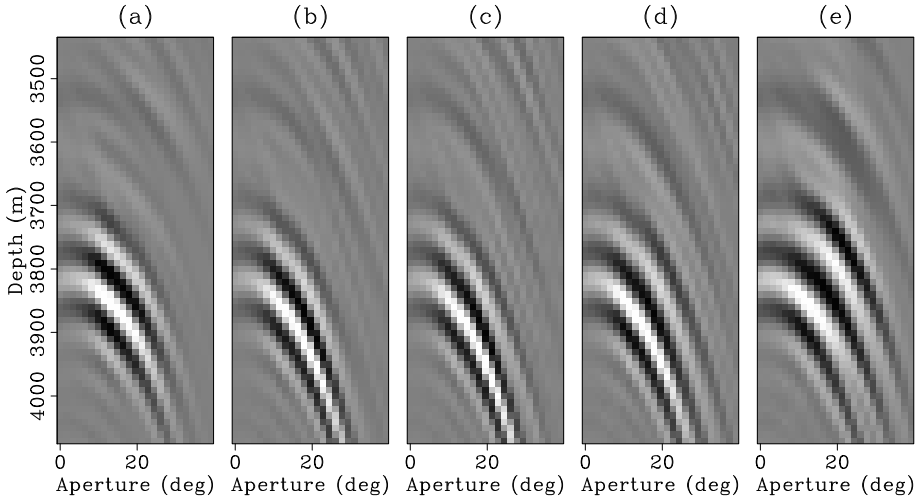


Figure 4.22: 3D ADCIG for the first-order water-bottom multiple reflection as a function of aperture angle. The different panels correspond to different reflection azimuth angles: (a)-40, (b)-20, (c)0, (d)20 and (e)40 degrees. 3dsynth-ap_gath2 [CR]

that, but because of the crossline dip, the over-migrated multiple illuminates the reflector at positive and negative azimuths.

## AZIMUTH ILLUMINATION

As I showed in the previous section, for a given non-zero aperture angle, the residual moveout of the primaries and the multiples in 3D ADCIGs is very different as a function of azimuth. In this section I explore the possibility of using this azimuth dependence as a tool to attenuate the multiples.

### Stack of all azimuths

I start by stacking the 3D ADCIGs for the multiple and the primary over all azimuths and aperture angles. The result should be their migrated images. Figure 4.23 shows a comparison of the stack cubes of the primary and the water-bottom multiple. Panel (a) is the inline stacked section of the primary at crossline CMP-Y=1500 m. Panel (b) is the crossline stacked section of the primary at inline CMP-X=8450 m. Panel (c) is the inline stacked section of the multiple taken at crossline CMP-Y=462.5 m and panel (d) is the crossline stacked section of the multiple taken at inline CMP-X=8450 m. All panels are clipped at the maximum amplitude of the primary which would have been the case if they would have both been in the same panel. Notice that the vertical scale is not the same for both panels nor is the scale of the crossline axis. While the primary and the multiple appear to have the same dip in the crossline direction, the dip of the multiple is about twice greater. The multiple looks so washed out because its maximum amplitude is only about one twentieth the maximum amplitude of the primary. Figure 4.24 shows the same figure but with panels (a) and (b) clipped at maximum amplitude of the the primary and panels (c) and (d) clipped at the maximum amplitude of the multiple so that we can assess better the character of the multiple.

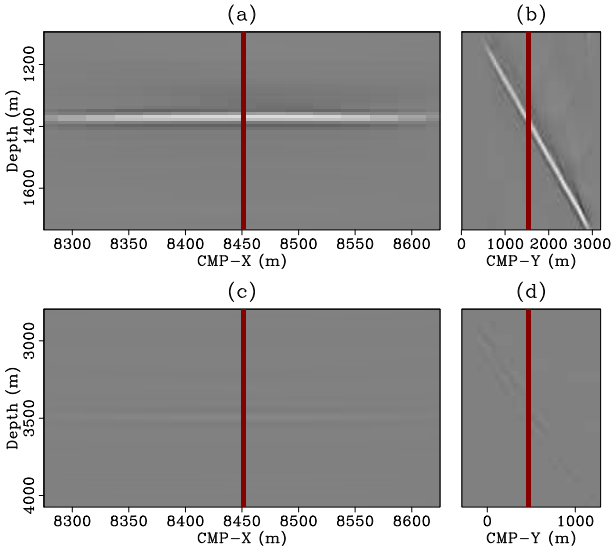


Figure 4.23: Stack over reflection azimuth and aperture angle of the 3DADCIGs computed for the water-bottom primary (panel (a)) and the water-bottom multiple (panel (b)). All panels clipped at the maximum amplitude of the primary. 3dsynth-full_az_stack_clip1 [CR]

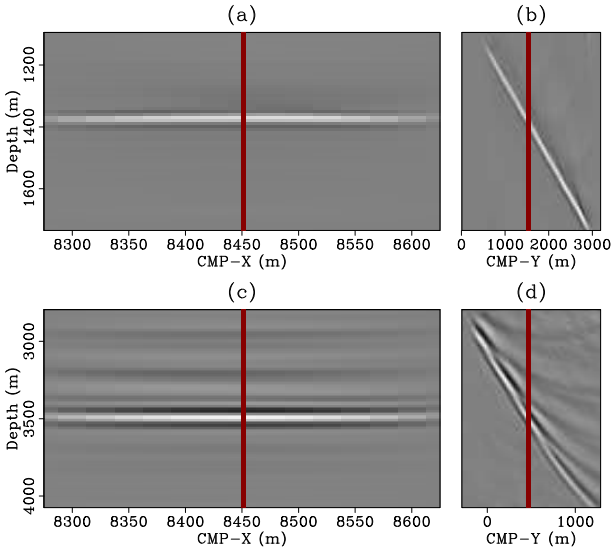


Figure 4.24: Stack over reflection azimuth and aperture angle of the 3DADCIGs computed for the water-bottom primary (panel (a)) and the water-bottom multiple (panel (b)). Panels (a) and (b) clipped at the maximum amplitude of the primary. Panels (c) and (d) clipped at the maximum amplitude of the multiple. 3dsynth-full_az_stack_clip2 [CR]

### Stack of selected azimuths

To select the combinations of aperture angle and reflection azimuths that more likely correspond to the primaries, I created a mask of ones and zeros and smoothed it. Figure 4.25 shows the mask. Compare with the depth slice in panel (a) of Figure 4.18. I then applied the mask and obtained, for both the primaries and the multiples.

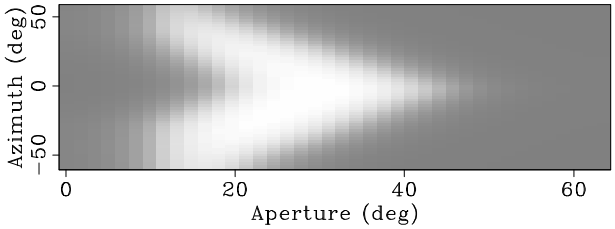


Figure 4.25: Mask to select the aperture angle-reflection azimuth combination illuminating the primary. White is one. 3dsynth-ap_az_mask [CR]

To assess how much of the multiple can be attenuated in the angle stack of the data I stacked the masked versions of both the primary and the multiple. In both cases I normalized by the number of traces (azimuths and aperture angles) that actually contributed to the stack given the mask. Figure 4.26 shows the results and is completely analogous to Figure 4.23. All panels are clipped at the maximum amplitude of the masked primary. The azimuth filtering decreased the overall energy of the already weak multiple. To better see the effect of the azimuth filtering, I plotted in Figure 4.27 the same data such that the primary is clipped at its maximum masked value and the multiple is clipped at the amplitude of the masked primary divided by the ratio between the maximum amplitudes of the un-masked primaries and the un-masked multiples, so that the figure is directly comparable to Figure **??**. Notice that the azimuth filtering decreased the overall amplitude of the multiple but did not appreciably alter its character.

### Azimuth of the multiple reflection

In the previous section I showed that, while the primaries were illuminated only by a relatively narrow range of azimuths at large aperture angles, the multiples were illuminated at a much wider range of azimuths and showed no increase in azimuth resolution as the aperture angle increased. This is not only due to the multiple being over-migrated. It is also due to the crossline

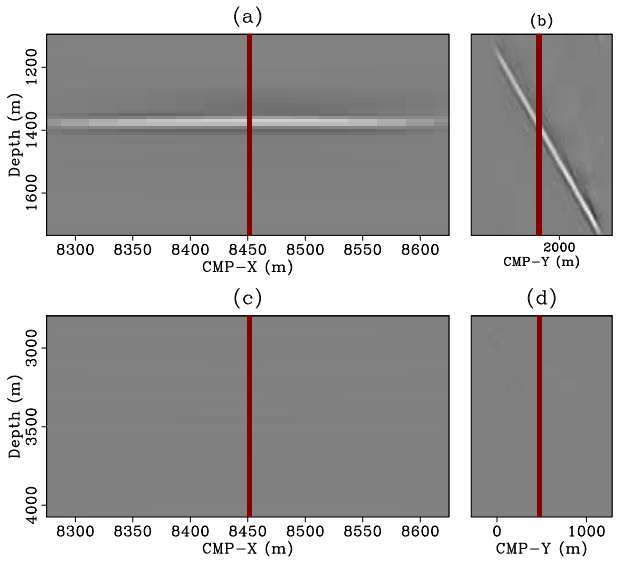


Figure 4.26: Stack over reflection azimuth and aperture angle of the masked 3D ADCIGs for the water-bottom primary (panel (a)) and the water-bottom multiple (panel (b)). All panels clipped at the maximum amplitude of the primary. 3dsynth-masked_az_stack_clip1 [CR]

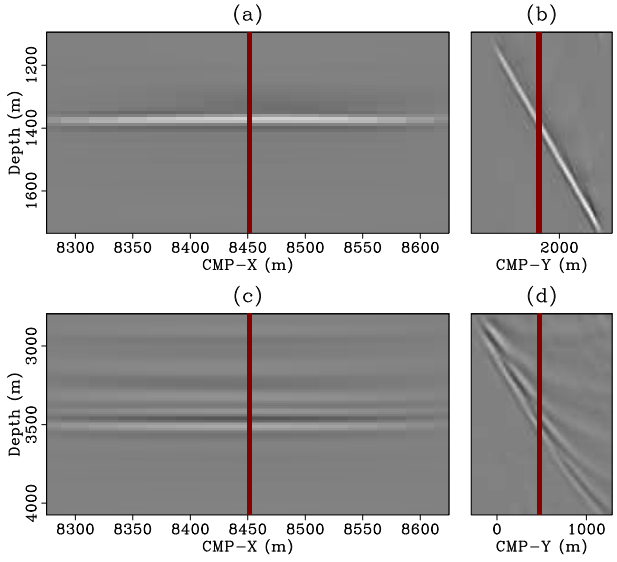


Figure 4.27: Stack over reflection azimuth and aperture angle of the masked 3D ADCIGs for the water-bottom primary (panel (a)) and the water-bottom multiple (panel (b)). Panels (a) and (b) clipped at the maximum amplitude of the masked primary and panels (c) and (d) clipped at that amplitude divided by the ratio between the maximum amplitude of the un-masked primary and the maximum amplitude of the un-masked multiple. 3dsynth-masked_az_stack_clip2 [CR]

dip of the water-bottom that makes the multiple path not being contained in a single plane. To emphasize this point, I migrated again the data with water velocity. In the absence of crossline dip, the multiple would behave exactly as a primary and would be well focused in SODCIGs and ADCIGs and show the same dependence with azimuth as the primary does. Figure 4.28 shows the inline SODCIG corresponding to exact same location as that in Figure 4.15. Notice how the multiple is now focused at zero inline subsurface offset while the deep primary (2000 m depth) is under-migrated and curves down. Similarly in Figure 4.29 that is equivalent to Figure 4.16. Notice that the water-bottom primary is migrated exactly as it was before since its migration velocity has not changed. Notice also the weak peg-leg multiple under-migrated at below 4000 m depth in panel (b).

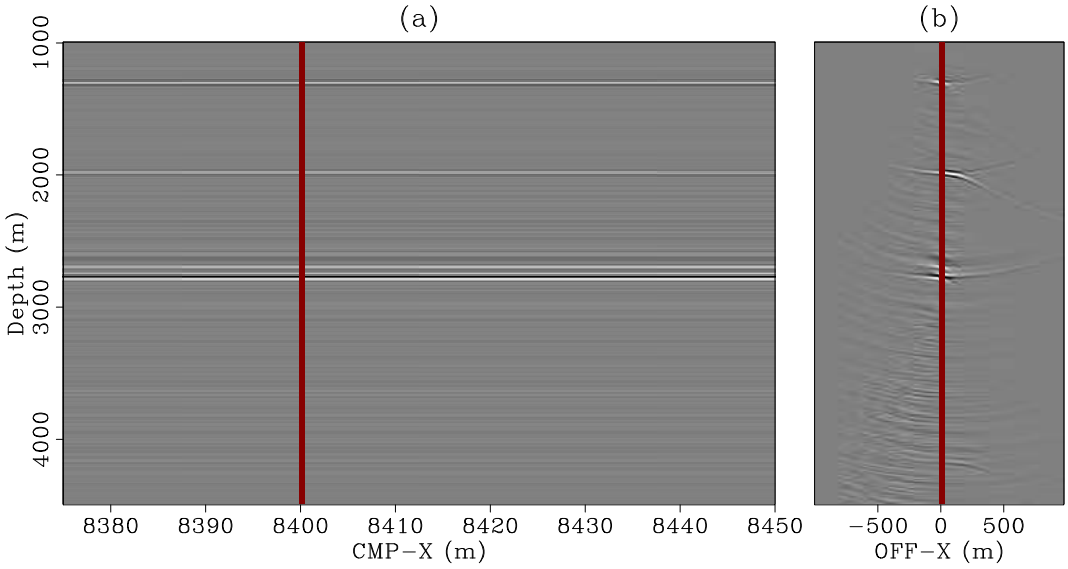


Figure 4.28: Migration with constant velocity. Panel (a) is the migrated inline section at CMP-Y=1212.5 m, zero inline subsurface offset and 25 m crossline subsurface offset. Panel (b) is the inline subsurface offset gather taken at CMP-X=8400 m, CMP-Y=1212.5 m and 25 m crossline subsurface offset. Notice again how the multiple is focused as a primary. 3dsynth-mig3d_inline_const_vel [CR]

To verify the azimuth dependence of the multiple migrated with the right velocity, I computed new ADCIGs. Figure 4.30 is equivalent to Figure 4.20. Although the multiple behaves like a primary in the inline SODCIGs, it behaves different from a primary in ADCIGs as a function of azimuth. Compare Figures 4.20 and 4.30. This is also emphasized in Figure 4.31

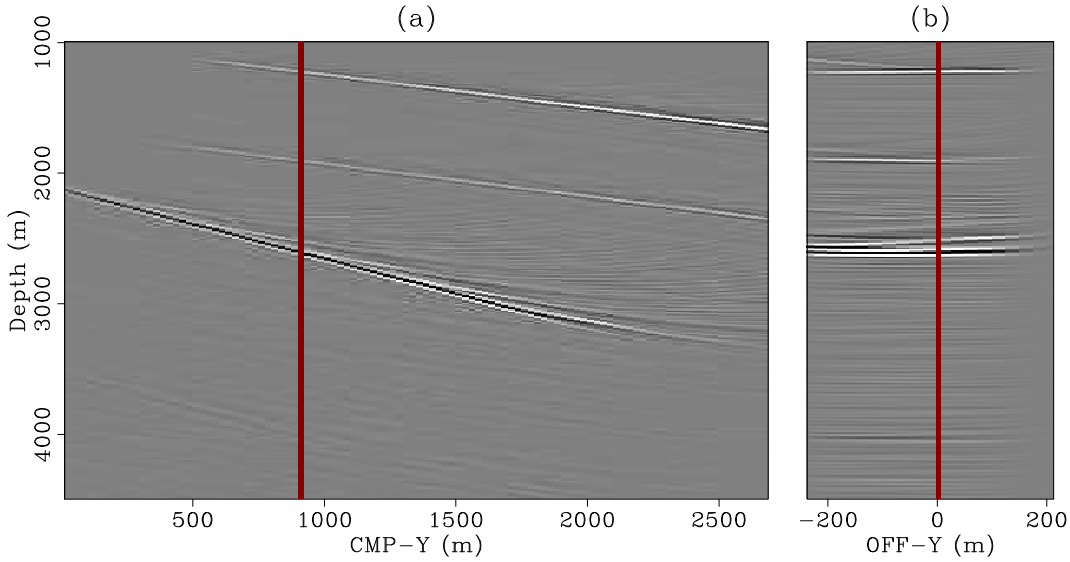


Figure 4.29: Migration with constant velocity. Panel (a) is the migrated crossline section at CMP-X=8450 m, zero inline subsurface offset and zero crossline subsurface offset. Panel (b) is the crossline subsurface offset gather taken at CMP-X=8450 m, CMP-Y=912.5 m and zero inline subsurface offset. 3dsynth-mig3d_xline_const_vel [CR]

which shows the residual moveout of the multiple as a function of aperture angle for fixed azimuth. This figure is the equivalent of Figure 4.22 for the primary. The effect of the crossline is to force the multiple reflection to take place in two different planes: one from the source to the reflector to the surface and a different one from the surface to the reflector to the receiver. The multiple, therefore, even though it was migrated with the correct velocity, is not equivalent to a primary ADCIGs.

## DISCUSSION

In principle, primaries and multiples can be separated not only in ADCIGs but even in SODCIGs. For this dataset, however, the crossline dips of the reflectors were relatively minor so that little difference existed in the crossline component of the SODCIGs between the primaries and the multiples. The discrimination between primaries and multiples in this case is exclusively in the inline subsurface offset direction. I will show in Chapters 5 and 6 with a real

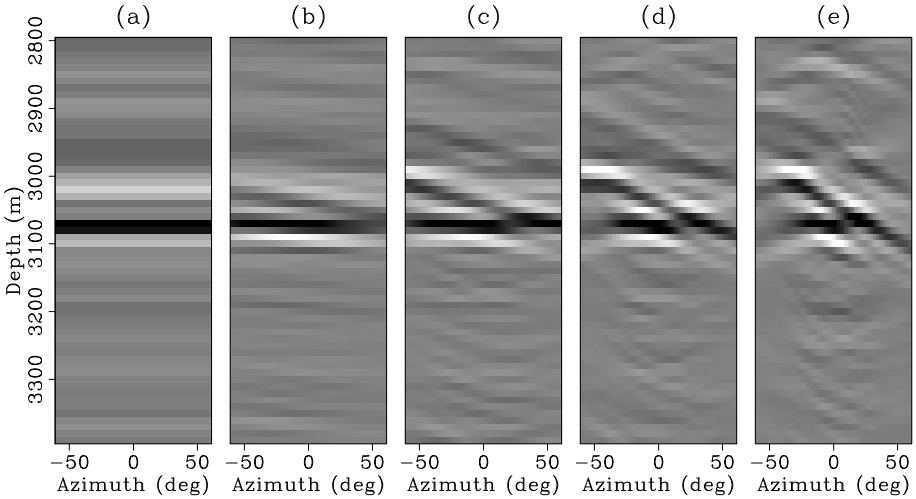


Figure 4.30: 3D ADCIG for the water-bottom multiple reflection migrated with water velocity as a function of azimuth. The different panels correspond to different aperture angles: (a) 0, (b) 5, (c) 10, (d) 15 and (e) 20 degrees. Compare with Figures 4.19 and 4.20. 3dsynth-az_gath2_const_vel [CR]

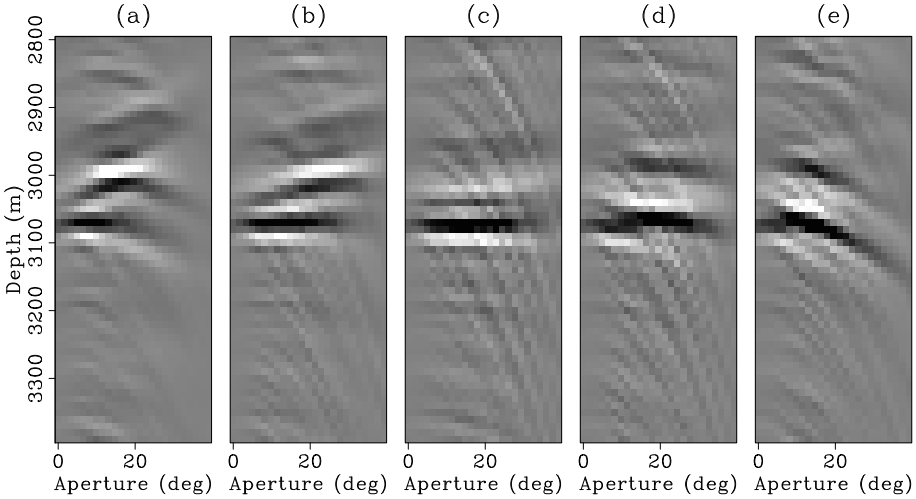


Figure 4.31: 3D ADCIG for the first-order water-bottom multiple reflection migrated with water velocity as a function of aperture angle. The different panels correspond to different reflection azimuth angles: (a)-40, (b)-20, (c)0, (d)20 and (e)40 degrees. Compare with Figures 4.21 and 4.22. 3dsynth-ap_gath2_const_vel [CR]

3D data example that, for subsalt reflections, and in general when the crossline dips are high, the discrimination between primaries and multiples can also happen in the crossline subsurface offset direction (provided enough crossline subsurface offsets were computed and enough crossline migration aperture was used).

Primaries and multiples can also be discriminated on the basis of their residual moveouts in 3D ADCIGs. Furthermore, in 3D ADCIGs there is the additional advantage of the multiples and the primaries behaving differently as a function of azimuth for a given aperture angle and as a function of aperture angle for a different azimuth. This differential azimuth dependency can be exploited to compute a three-dimensional Radon transform that is a function of aperture angle and azimuth similar to the apex-shifted Radon transform of chapter 2. For the sake of computer time, in Chapter 6 I will take the simpler route of attenuating the multiples as a function of aperture only by first stacking the data over azimuths. I use a slight modification of the methodology presented in Chapters 2 and 3.

In this chapter I make no attempt to actually compute a multiple model, and thereby estimate the primaries, for two reasons: first, the model is so simple that the multiples and the primaries separate completely as a function of depth in the Radon domain, defeating the purpose of separating them as a function of curvature. Second, a full application of the ideas presented in this chapter will be applied in Chapter 6 with all the challenges of real data and therefore it would be redundant to present it here. The value of this chapter is that the simple model allows a relatively straight forward interpretation of the mapping of the multiples in the five-dimensional image spaces of SODCIGs and ADCIGs, which would have been difficult with real data. The lessons learned in this chapter will prove useful in interpreting the less straight forward results of Chapter 6.

Another important result of this chapter is the realization that, despite its theoretical appeal, source-receiver migration is not an ideal imaging tool for these kinds of sparse geometry (even without feathering). For the imaging of the real dataset, therefore, I will use shot profile migration. The main advantage is that each shot can be migrated separately, feathering is easier to handle and, more importantly, there is no need to create a gigantic, regular, five-dimensional dataset.

## CONCLUSION

Although the migration results were somewhat limited because of the huge amount of data needed to form a complete five-dimensional dataset, even for a very small area, they do show that with 3D data we can discriminate between primaries and multiples in the image space on the basis of their different residual moveouts in SODCIGs or ADCIGs, and as a function of azimuth in 3D ADCIGs.

## ACKNOWLEDGMENTS

I would like to thank ExxonMobil for providing the 3D synthetic dataset.

# Chapter 5

# Imaging and mapping 3D multiples to image gathers: Example with a Gulf of Mexico dataset

**SUMMARY**

In this chapter, I migrate a real 3D seismic dataset from the Gulf of Mexico with shot profile migration. The dataset contains specular water-bottom multiples, peg-leg multiples associated with a large, shallow salt body, and diffracted multiples originating at the salt edges. Both the water bottom and the salt body have significant cross-line dip which makes it difficult to model the trajectory of the multiples and to apply 3D SRME. The location of the multiples in the image domain is severely affected by the presence of the salt and thus do not follow the geometry of the multiple-generating interface. As a consequence, some multiples could easily be interpreted as primaries. I show that primaries and multiples (even subsalt) can be discriminated by their different moveouts in SODCIGs and ADCIGs as in Chapter 4.

## INTRODUCTION

The Gulf of Mexico dataset, provided by VeritasDGC, was acquired over a complex salt body with structure in both the inline and the cross-line directions. The water-bottom dips in some places as much as 11 degrees in the cross-line direction making the mapping of the multiples in the image-space cube difficult to predict. The presence of the salt distorts the multiples so much that in many cases it is difficult to discern with any certainty which events are multiples and which events are primaries in the migrated cube. An important tool for that purpose are the SODCIGs where the multiples can be identified by their tendency to map away from zero inline and crossline subsurface offsets, and the ADCIGs where primaries should be flat as a function of aperture angle while multiples exhibit residual moveout as I showed in Chapter 4.

I first migrate a sail line, with shot profile migration, to assess the possibility of discriminating between primaries and multiples on inline subsurface offsets, where, according to the results of Chapter 4, there is better chance of imaging the multiples. The results are encouraging and show in several places that enough differential curvature exists between primaries and multiples in inline SODCIGS and ADCIGs even below salt. The image cube, however, is poor because of the large crossline dips that require that much more than one sail line be migrated in order to capture the flanks of the salt bodies and in one case even its top and bottom. The multiples, of course, are also improperly migrated in just one sail line. I then migrate the entire dataset with a large crossline migration aperture. Due to computer limitations, only a relatively small inline migration aperture was used and no prestack image gathers were created. The image cube shows great improvement in the image of the salt flanks as well as the top and bottom salt reflections that were missing from the migration of only one sail line. The steepest salt flanks are still poorly imaged because of the limitations in the amount of available data. This image cube was used to select a smaller dataset below a small salt body, to perform a full-fledged shot profile migration with the computation of prestack images in both the inline and crossline directions.

In this chapter I will compare the different prestack image domains and show the behavior of the primaries and multiples, in particular subsalt multiples. I will defer until the next chapter the actual attenuation of the multiples.

# DESCRIPTION OF THE DATA

## Acquisition geometry

The 3D dataset consists of 20 sail lines each with four active streamers and dual flip-flop shooting. The separation between streamers is 160 m and between receivers is 25 m. The shot interval is 37.5 m (between the flip and the flop). The minimum offset inline is 240 m and each streamer has 288 receivers for a maximum inline offset of 7175 m. Figure 5.1 shows the acquisition template. Figure 5.2 shows a map view of the subset of the shots used in this thesis. Although most sail lines were straight in the East-West direction, a few had significant curvature.

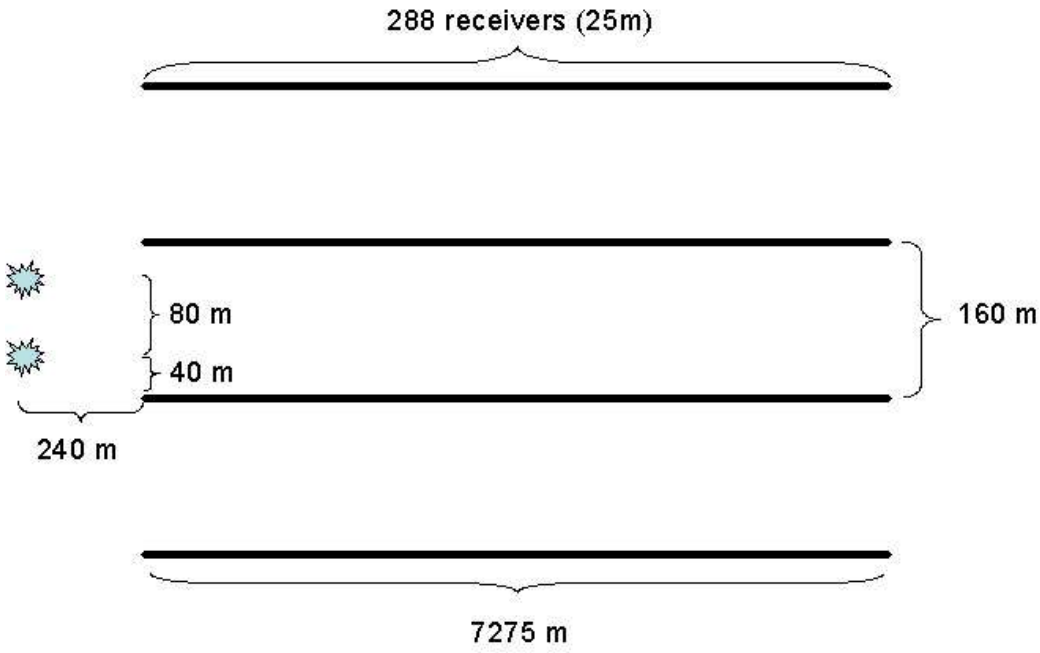


Figure 5.1: Sketch of the basic acquisition geometry 3dreal-acq_sktch1 [NR]

The strong currents present in the area caused significant feathering. Figure 5.3 shows an example for the sail-line at cross-line distance 11440 m (see Figure 5.2. The feathering angle is about 25 deg with respect to the inline direction. For most shots, the feathering was in the same South-North direction. Figure 5.4 shows the fold of coverage that in some places depart

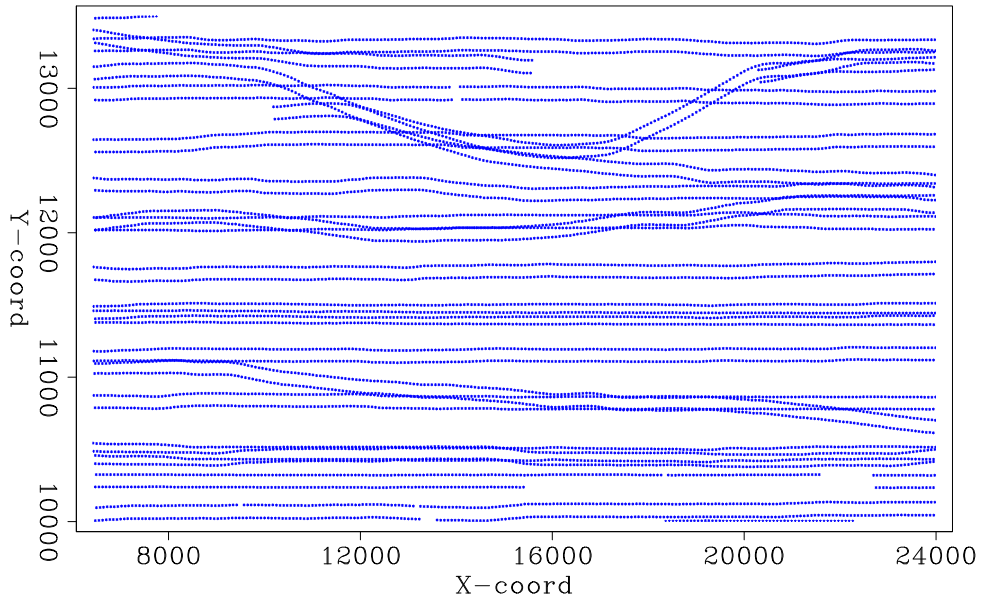


Figure 5.2: Map view of the source locations. 3dreal-shots_map [CR]

significantly from its design value of 48. Some of the short source lines in Figure 5.2 were acquired as infill to avoid large coverage holes.

### Migration velocity model

The migration velocity model (provided by Norsk Hydro), shows a large, complex salt body with steeply dipping flanks in both inline and cross-line directions (Figure 5.5). The water-bottom itself dips in some places as much as 11 degrees in the cross-line direction, although it is relatively flat in the inline direction.

## SHOT PROFILE MIGRATION

Attempting to migrate and compute 3D angle gathers for the entire dataset would be way too expensive, so I started by migrating the data without computing prestack 3D images. The idea is to obtain a good image that can be used to select a smaller, subsalt dataset, on which

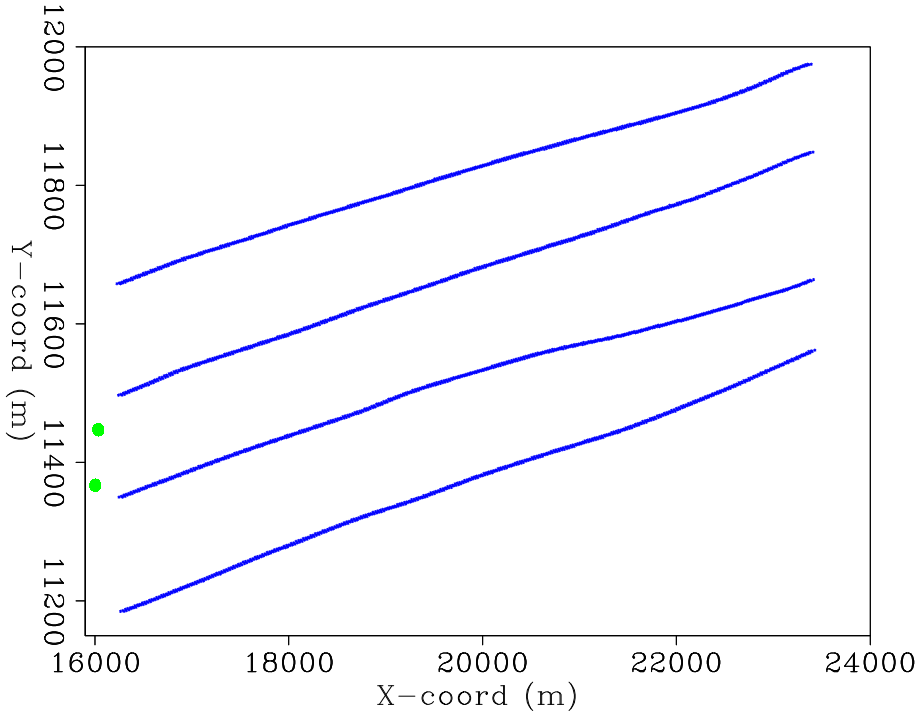


Figure 5.3: Map view of the receiver cables for one shot illustrating typical feathering. The feathering angle is about 25 deg with respect to the inline direction. 3dreal-feathering [CR]

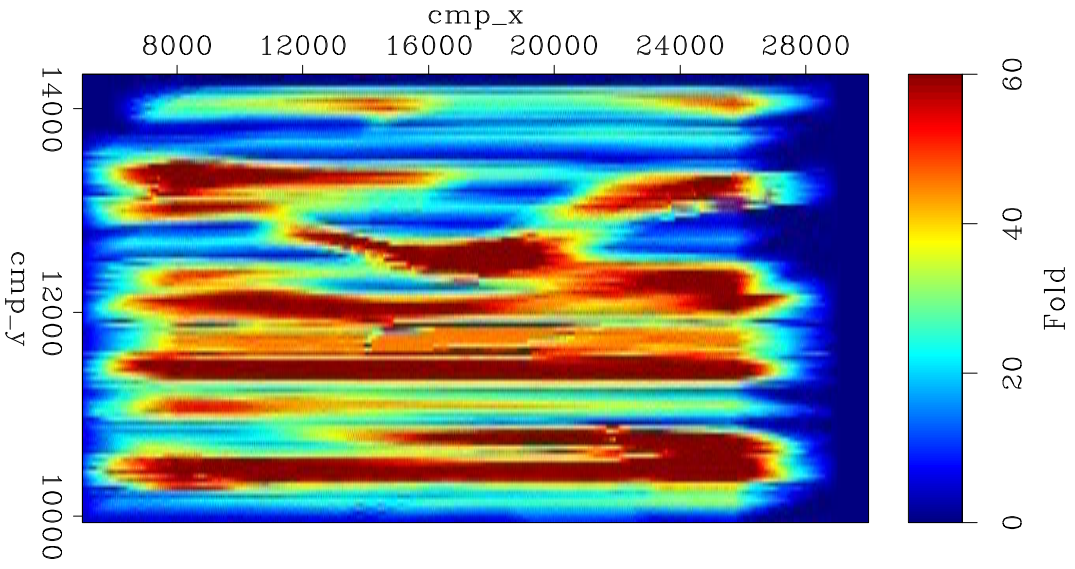


Figure 5.4: Fold map illustrating relatively uniform coverage. 3dreal-fold [CR]

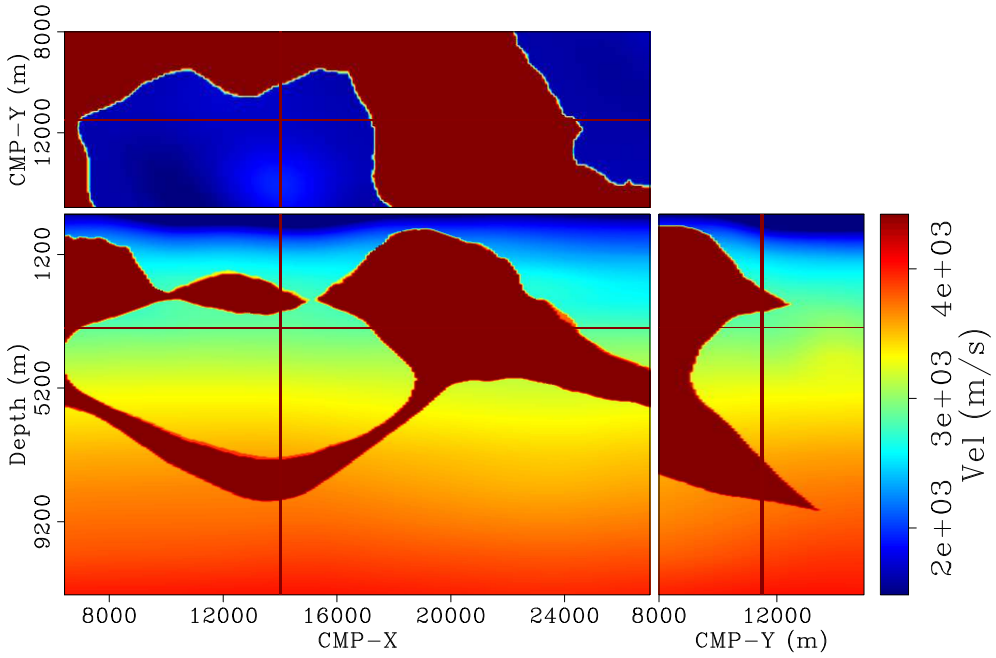


Figure 5.5: Subsurface velocity model. Note the strong dips in both the inline and cross-line directions. 3dreal-vmodel [CR]

to compute the image gathers. Table 5.1 shows the parameters and data extent used for this migration.

Table 5.1: Migration parameters and data extent for full migration.

| Inline | | | Crossline | | |
|---|---|---|---|---|---|
| Min CMP | Max CMP | Aperture (m) | Min CMP | Max CMP | Aperture (m) |
| 5000 | 32000 | 10000 | 10000 | 14000 | 4000 |

In order to efficiently migrate the data with shot profile migration, I removed the time samples before the water-bottom arrival. This is equivalent to time-shifting the data (changing its origin) and I compensated for it by applying a linear frequency shift to the source wavelet. The propagation through the water layer was done in two depth steps and from there down the depth sampling was 10 m. The propagation was done with a Phase Shift Plus Interpolation algorithm (Gazdag and Sguazzero, 1984; Biondi, 2006). For the sake of computer time, only

two reference velocities, computed with Lloyd's algorithm (Clapp, 2004), were used to propagate the data at each depth step. Four hundred frequencies were used from 6 to 40 Hz. A total of 8600 shots were migrated. Figure 5.6 shows an inline section taken at CMP-Y=11840 m. Again, recall that the depth axis is with respect to an arbitrary reference. The migrated data was filtered in depth and a gain proportional to the depth squared was applied for display purposes. Both the top and bottom reflections of the smaller salt body are well imaged, as are most subsalt reflections directly below it. The salt bottom reflection for the larger salt body is also well imaged but its right flank is poorly imaged because of lack of data. The available dataset did not extend enough beyond CMP-X=25000 m to capture the corresponding reflections. Notice what seems to be a multiple below 4000 m depth, specially around CMP-X=16000 m. The rectangle encloses the subset image that was deemed most promising to illustrate the attenuation of subsalt multiples. A new shot profile migration, including the computation of prestack images was carried out on this subset of the data.

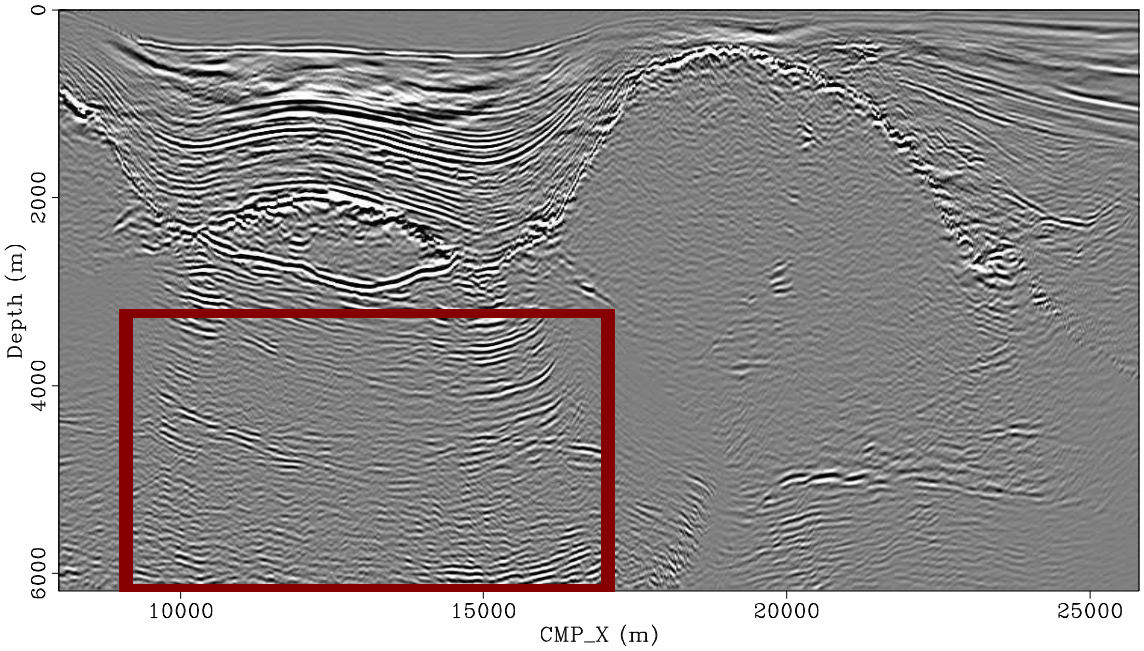


Figure 5.6: Shot profile migration. Inline image section at crossline CMP 11440 m. The rectangle encloses the subset of the image for which a new migration was performed including the computation of prestack images. 3dreal-mignooffs_inline [CR]

Figure 5.7 shows the crossline image section taken at CMP-X=12000 m. Notice that the

bottom of the salt and the subsalt reflections deteriorate to the left of about CMP-Y=11500 m. This again is due to lack of available data to the left of CMP-Y=10000 m. Here again the rectangle encloses the subset of the data to attempt the attenuation of subsalt multiples.

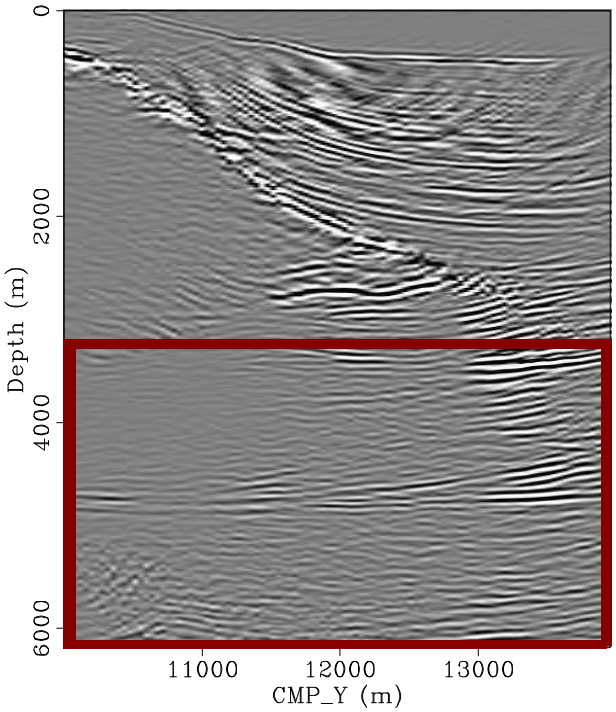


Figure 5.7: Shot profile migration. Crossline image section at inline 12000 m. The rectangle encloses the subset of the image for which a new migration was performed including the computation of prestack images. 3dreal-mignooffs_xline [CR]

## PRESTACK MIGRATED IMAGES

Based on the results of the previous section, I computed the full-fledged shot profile migration of the selected sub-salt dataset, including the computation of three-dimensional image gathers. The migration parameters and the range of data migrated are summarized in table 5.2. Four reference velocities were used at each depth extrapolation step, chosen with Lloyd's algorithm. Two hundred and fifty frequencies were used in the range 6-38 Hz. Three hundred depth extrapolation steps were taken at 10 m depth interval. A total of 4300 shots were migrated.

The result of the shot profile migration is a five-dimensional cube that is challenging to visualize. I will show some of the more common prestack subsets of the data to give an idea of the mapping of both primaries and multiples in the migrated domain. Figure 5.8 shows

Table 5.2: Migration parameters and data extent. The minimum and maximum offsets refer to the subsurface offsets for the SODCIGs.

| Inline | | | | |
|---|---|---|---|---|
| Min CMP | Max CMP | Min OFF (m) | Max OFF (m) | Aperture (m) |
| 9000 | 17000 | -750 | 250 | 8000 |
| **Crossline** | | | | |
| Min CMP | Max CMP | Min OFF (m) | Max OFF (m) | Aperture (m) |
| 10000 | 14000 | -600 | 600 | 4000 |

the 3D image cube taken at zero inline and zero crossline subsurface offsets. The top panel shows a depth slice at 4630 m where there is a hint of a multiple cutting through the primary reflections shown in the inline section (left panel) and pointed to by the arrow. This inline section is taken at CMP-Y=13000 m. The right panel shows the crossline section at CMP-X=14400 m. It is very difficult to discriminate which of these subsalt reflections are primaries and which are multiples without the help of prestack migrated images. The image in the crossline direction (right panel) is not nearly as clear because of the relatively few crossline CMPs that went into the prestack migration. This makes the identification of multiples in that panel even more difficult.

Ideally, the primaries should migrate to zero inline and zero crossline subsurface offsets. Errors in migration velocity and illumination problems may make them shift away from zero subsurface offsets, but in most situations these shifts away from zero subsurface offset are minor when compared to those of the multiples for which the difference between propagation and migration velocity is large. Therefore, we can expect that the primaries and the multiples be relatively easy to identify by their mapping in both the inline and crossline subsurface offsets. Figure 5.9 shows one 3D SODCIG taken at the spatial location CMP-X=14400 m and CMP-Y=13000 m (see Figure 5.8). The inline offset gather (panel (a)), corresponds to OFF-Y=0 while the crossline offset gather (panel (b)), corresponds to OFF-X=-500 m. In the inline offset gather we see that the primaries map near zero offset (above 3000 m) whereas the multiples map entirely to the negative subsurface offsets (around 4500 m and below 5500 m). Since the crossline offset gather is taken at the inline offset of the multiple (-500 m), the

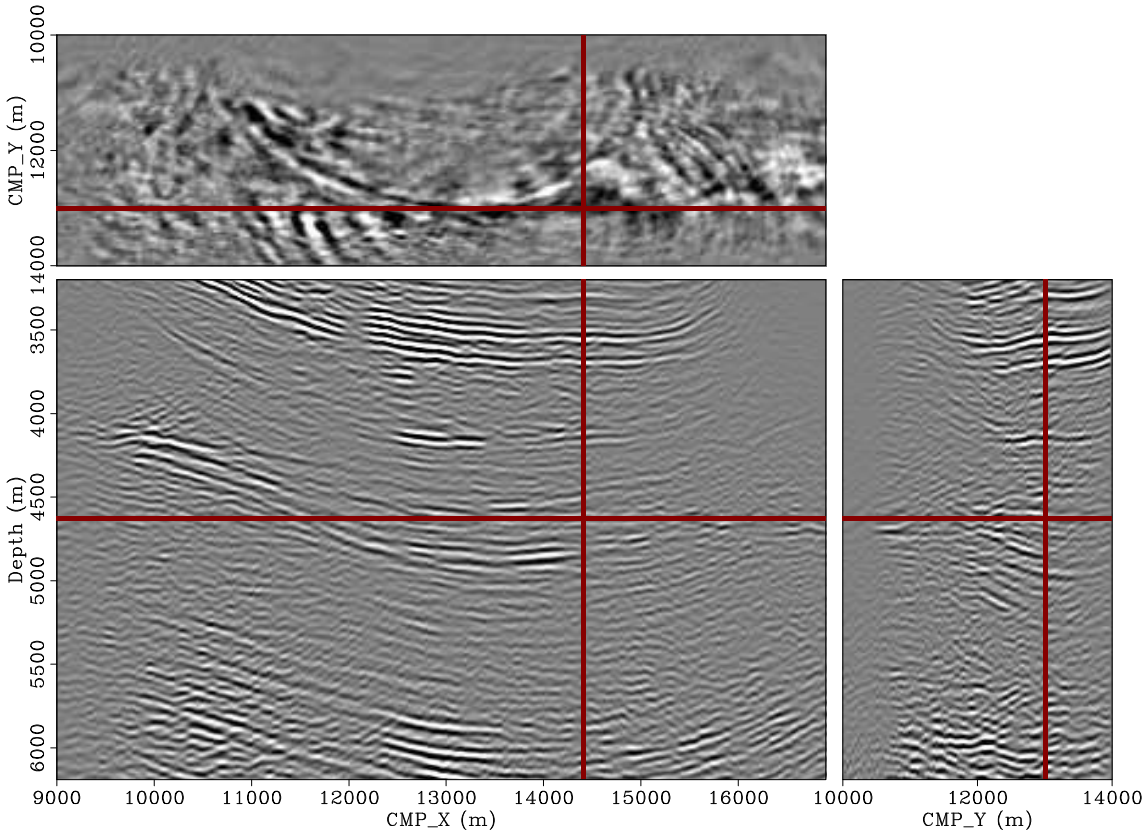


Figure 5.8: Shot profile migration. Zero subsurface offset cube. Top panel is a depth slice at 6430 m, left panel is the inline section at crossline 13000 m and right panel is the crossline section at inline 14400 m. 3dreal-3dzoff [CR]

primaries are absent and the multiples map to both positive and negative subsurface offsets. This is a consequence of the geometry of acquisition that had positive inline surface offsets only but positive and negative crossline surface offsets. Notice also that more subsurface offsets, specially in the crossline direction, should have been computed in order to capture the multiples in their entirety.

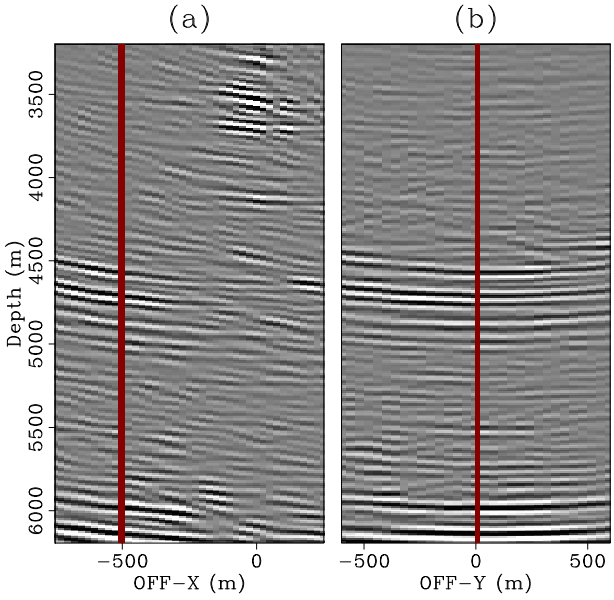


Figure 5.9: Shot profile migration. SODCIG at CMP-X=14400 m and CMP-Y=13000 m. Panel (a) is the inline offset gather taken at OFF-Y=0 and panel (b) is the crossline offset gather taken at OFF-X=-500 m. 3dreal-gather_14400_13000 [CR]

Figure 5.10 shows a subset of the five dimensional hyper-cube taken at CMP-Y=13000 m and OFF-Y=0 m. There is, therefore, no crossline information on this figure. Panels (a) and (c) show the inline sections at zero and -400 m inline subsurface offsets respectively, while the middle panel shows the inline gather at CMP-X=14400. Since the crossline offset is zero in all the panels, we can expect to see the primaries near the zero inline offset in panel (b) and as the dominant reflections in panel (a). The multiples (at least those that did not map away from zero crossline offset), we can expect to find at the negative inline offsets in panel (b) and as the dominant reflections in panel (c). Notice how it would have been very hard to visually distinguish primaries and multiples without the aid of these prestack images.

To take an even closer look at the multiples, Figure 5.11 shows a similar figure to Figure 5.10 but for CMP-X=9900 m. This time both panels (a) and (c) correspond mostly to multiples. An interesting observation is that the residual moveout of the multiple in panel (b) seems to have its bottom away from zero inline subsurface offset, indicating perhaps a

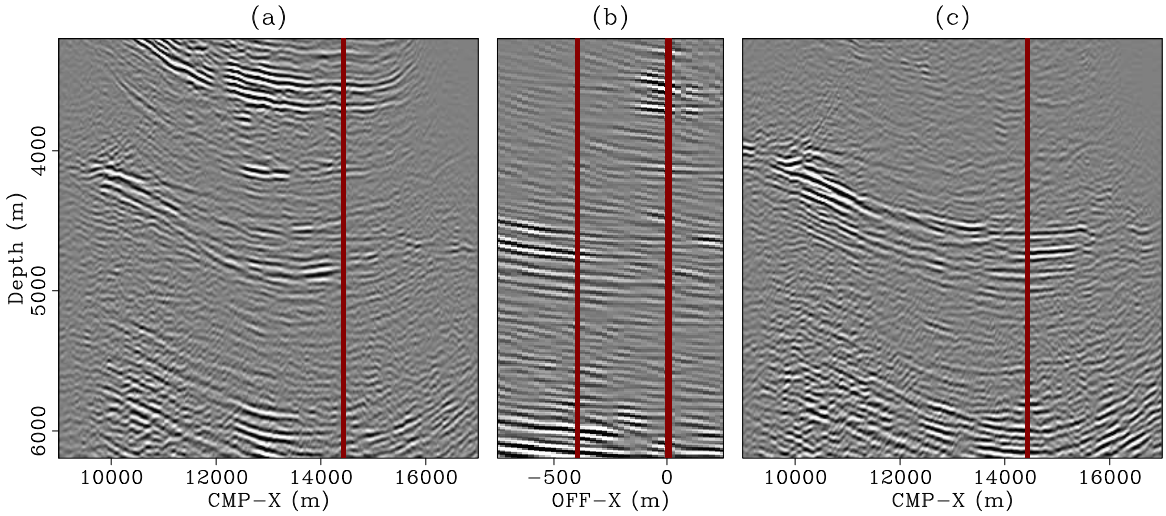


Figure 5.10: Inline section and inline offsets at CMP-Y=13000 m and OFF-Y=0. Panel (a) is the inline section at zero inline offset. Panel (b) is the inline offsets at CMP-X=14400 m and Panel (c) is the inline section at -400 m inline offsets. Panel (a) should be mostly primaries while panel (c) should be mostly multiples. 3dreal-inline1_0_13000 [CR]

diffracted multiple. Furthermore, recall that this inline plane is taken at zero crossline offset. The situation is even more manifest if the section is taken at a crossline offset away from zero.

Finally, to illustrate the mapping of the multiples in the crossline direction, Figure 5.13 shows the subset taken at CMP-X=14000 m and OFF-X=0. As with the previous two figures, panel (a) corresponds to the crossline section at OFF-Y=0 while panel (c) is a similar section at OFF-Y=-400 m. The middle panel corresponds to the crossline offset gather. Here also the primaries should map to panel (a) while some of the multiples (those that did not map away from zero inline offset), should map to panel (c). In panel (b) we can see that the primaries map near zero crossline offset while the multiples map away from zero both to positive and negative subsurface offsets. Similarly, Figure 5.14 shows the subset taken at the same CMP-X location but at OFF-X=-600 m. Both panels (a) and (c) should now correspond to multiples and no primaries should be mapped to any of these panels.

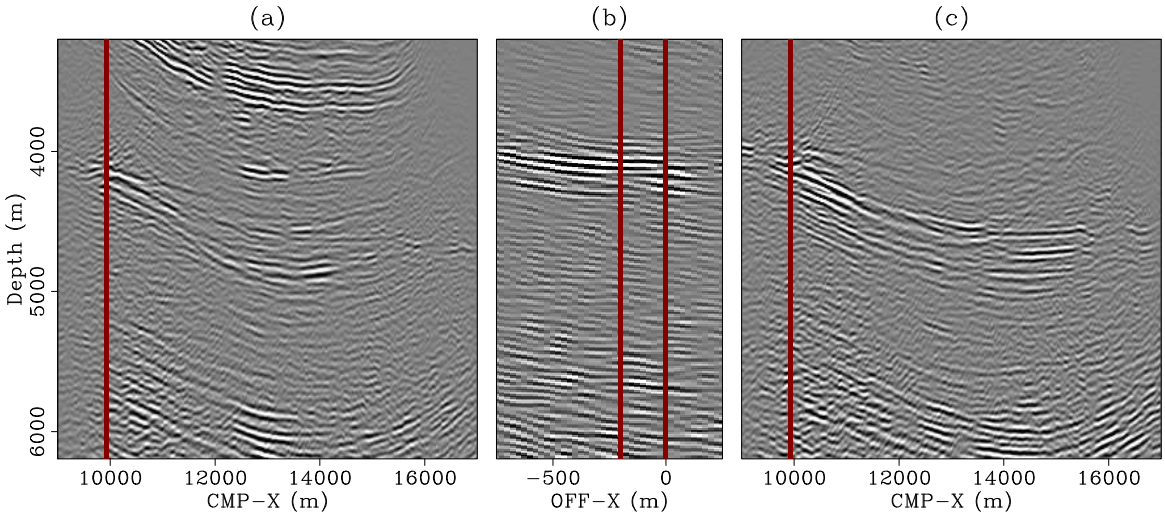


Figure 5.11: Inline section and inline-offset gather at CMP-Y=13000 m and OFF-Y=0. Panel (a) is the inline section at zero inline offset. Panel (b) is the inline offsets at CMP-X=9900 and Panel (c) is the inline section at -200 m inline offsets. Panel (a) is mostly primaries and panel (c) is mostly multiples. 3dreal-inline2_0_13000 [CR]

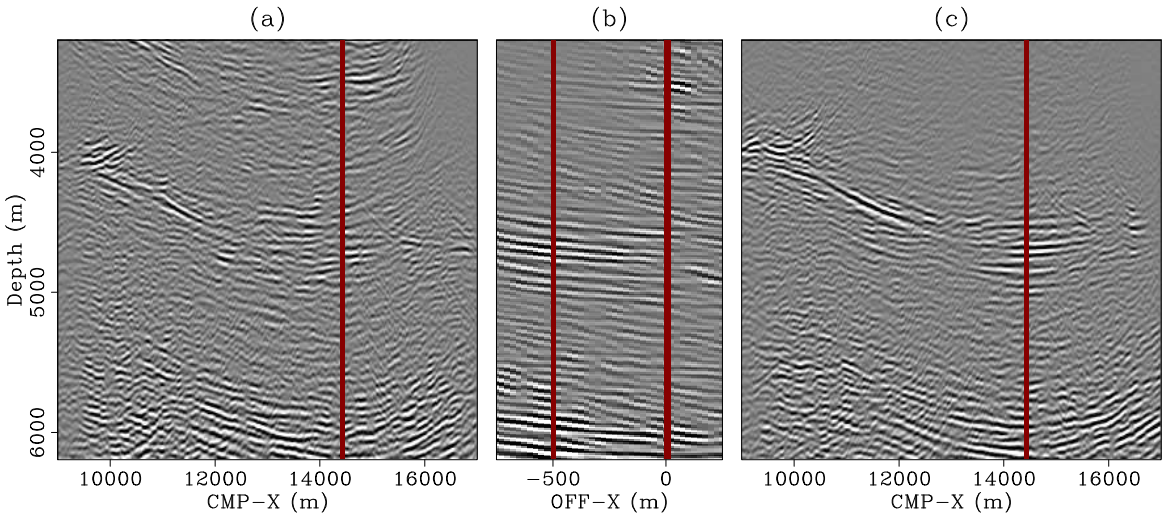


Figure 5.12: Inline section and inline-offset gather at CMP-Y=13000 m and OFF-Y=-400. Panel (a) is the inline section at zero inline offset. Panel (b) is the inline offsets at CMP-X=14400 and Panel (c) is the inline section at -500 m inline offsets. Panel (a) has some contributions from primaries and multiples whereas panel (c) should be almost exclusively multiples. 3dreal-inline1-400_13000 [CR]

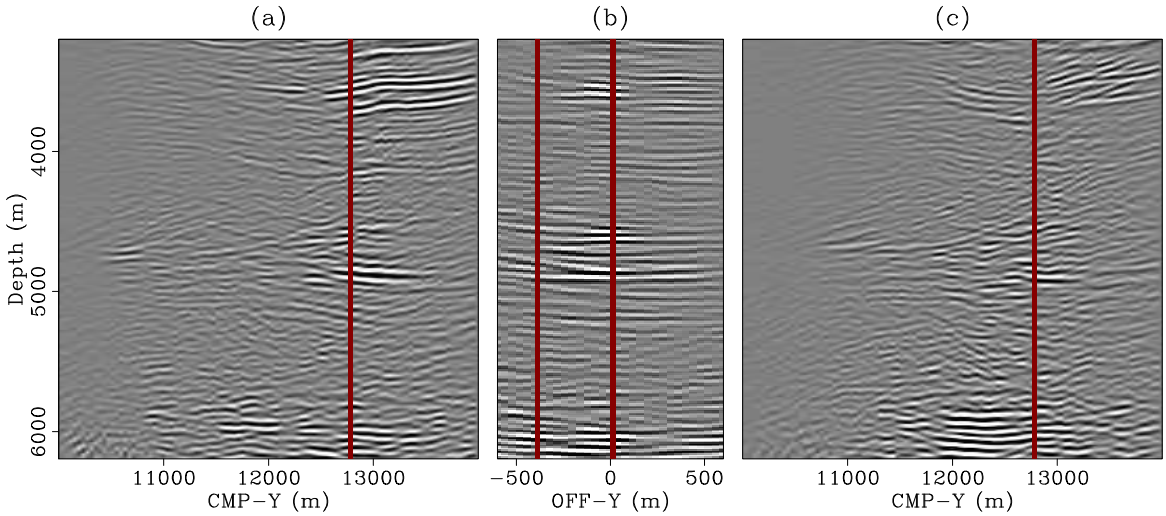


Figure 5.13: Shot profile migration. Crossline section and crossline offsets at CMP-X=14000 m and OFF-X=0. Panel (a) is the crossline section at zero crossline offset. Panel (b) is the crossline offsets at CMP-Y=12760 m and Panel (c) is the crossline section at -400 m crossline offsets. Panel (a) should be mostly primaries while panel (c) should be mostly multiples. 3dreal-xline1_0_14000 [CR]

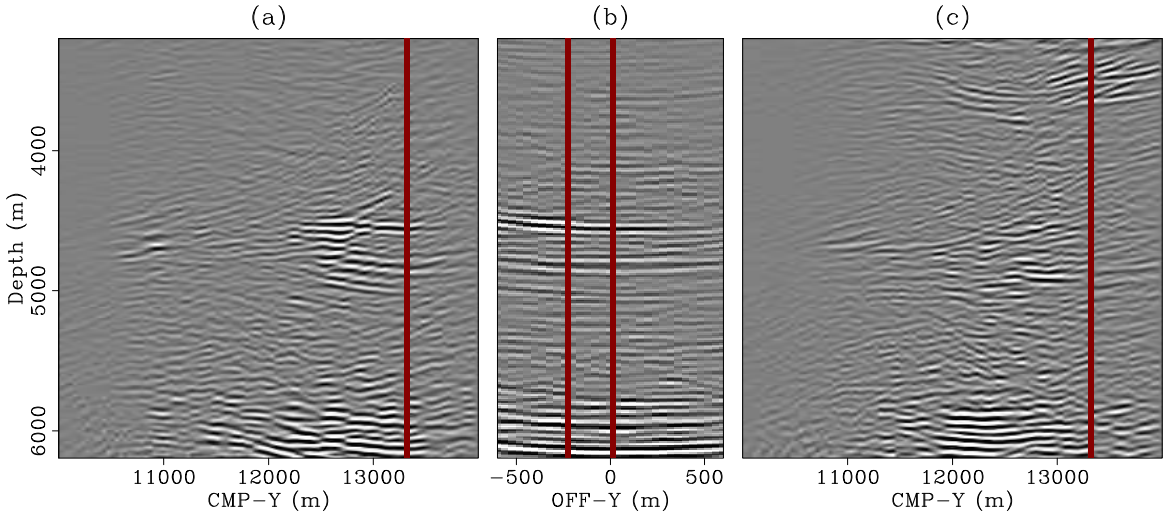


Figure 5.14: Shot profile migration. Crossline section and crossline offsets at CMP-Y=14000 m and OFF-X=-600. Panel (a) is the crossline section at zero crossline offset. Panel (b) is the crossline offsets at CMP-Y=13300 m and Panel (c) is the crossline section at -240 m crossline offsets. Both panels (a) and panel (c) should be multiples. 3dreal-xline1-600_14000 [CR]

## MULTIPLES IN ADCIGS

I will now show the results of computing the 3D angle gathers from the SODCIGs shown in the previous section. Figure 5.15 shows two 3D angle gathers. The first one (panel (a)) is taken at CMP_X=14000 m and CMP_Y=13500 m and the second one (panel (b)) at CMP_X=11000 m and CMP_Y=13000 m. The 3D ADCIG in Panel (a) shows two strong primaries at the top and and weak multiples at the bottom. Notice in the depth slice a pattern similar to the one obtained for the synthetic data primary in Chapter 4 (recall panel panel (a) of Figure 4.18). Notice also that the azimuth coverage of the primaries decreases (that is, the azimuth resolution increases), as the aperture angle increases. The two primaries focus at slightly different azimuths as seen in the azimuth gather of panel (a). The 3D ADCIG in Panel (b), on the other hand, shows a weak primary at the very top and a strong multiple at the bottom. Again, the depth slice is consistent with the one obtained for the synthetic data multiple in Chapter 4 (recall panel (b) of Figure 4.18) and, contrary to the primary, shows a broad range of azimuth coverage at large aperture angles.

In order to investigate the variation of the residual moveout of primaries and multiples with reflection azimuth, I plot in Figure 5.16 the angle gather at location CMP_X=13000 m and CMP_Y=13000 m for aperture angles of 0, 5, 10, 15 and 20 degrees. At zero aperture angle (panel (a)), neither the primaries nor the multiples show any azimuth resolution. As the aperture angle increases, the primaries are focused to a relatively narrow range of azimuths (panel (e) above 5500 m) whereas the multiples are essentially scattered. Similarly, Figure 5.17 shows the same gathers but at location CMP_X=14000 m and CMP_Y=14000 m. Again, notice the azimuth focusing of the weak primaries at the top (panel (e)) and the upswings of the multiple (panels (c), (d) and (e)). The lack of azimuth focusing of the multiples with increasing aperture angle is a consequence of the crossline dip and velocity lateral velocity variations that cause the multiple path to be very complex with no defined azimuth even for large aperture angle.

Finally, to investigate the variation of the residual moveout of the primaries and the multiples with aperture angle, Figures 5.18 and 5.17 show angle gathers at reflection azimuths of -40, -20, 0, 20, 40 at the same locations as Figures 5.16 and 5.19, respectively. Notice that in

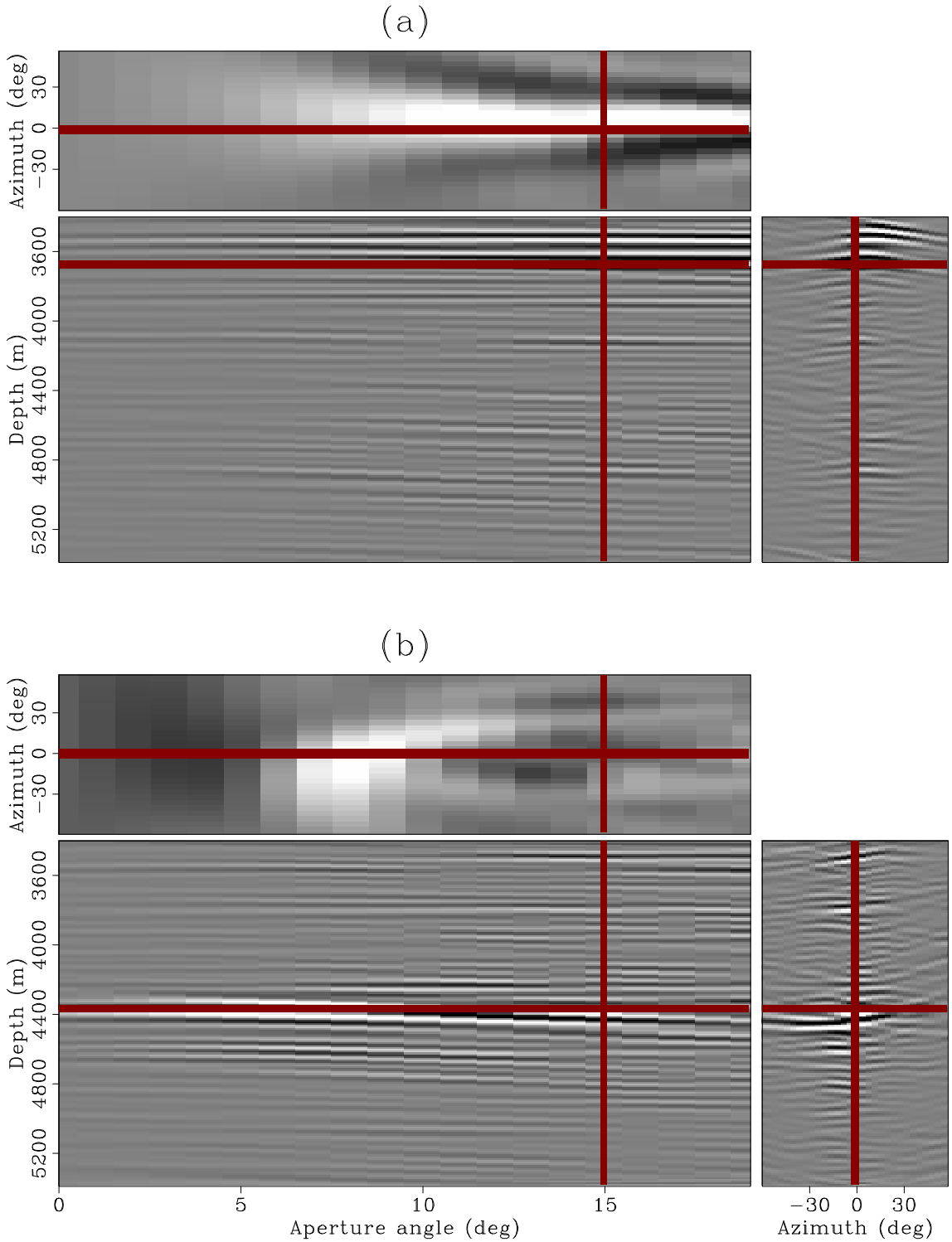


Figure 5.15: 3D angle gathers. (a) at CMP_X=14000 m and CMP_Y=13500 m. (b) at CMP_X=11000 m and CMP_Y=13000 m. Notice the strong primaries above 5500 m depth in panel (a) and the strong multiple below 6000 m depth in panel (b). 3dreal-3d_gaths_14000_13500-11000_13000 [CR]

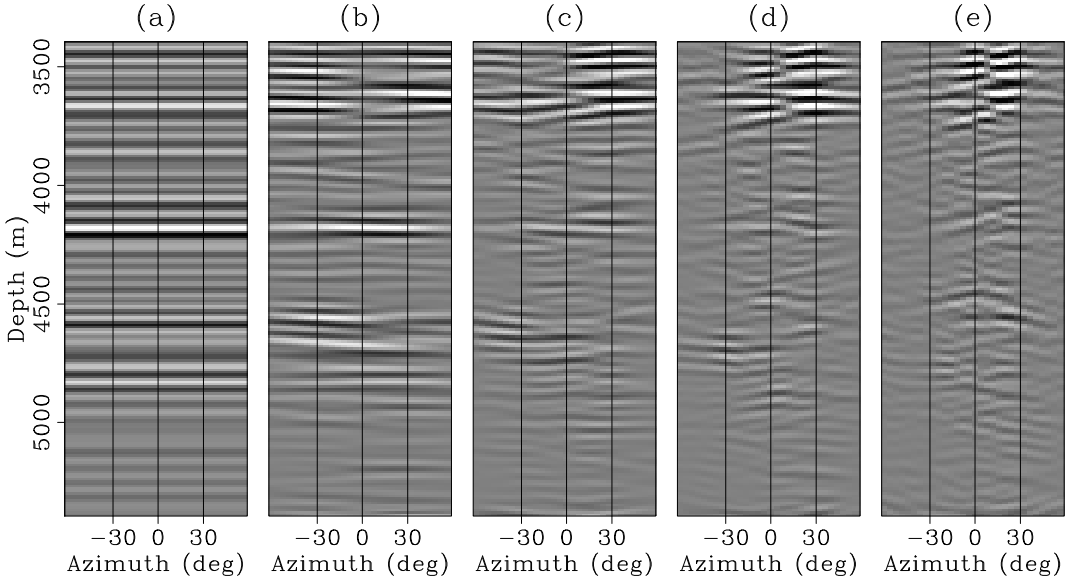


Figure 5.16: 3D angle gathers as a function of azimuth for aperture angles of 0, 5, 10, 15 and 20 degrees (panels (a) through (e)). The gather is taken at CMP_X=13000 m and CMP_Y=13000 m. 3dreal-3d_az_13000_13000 [CR]

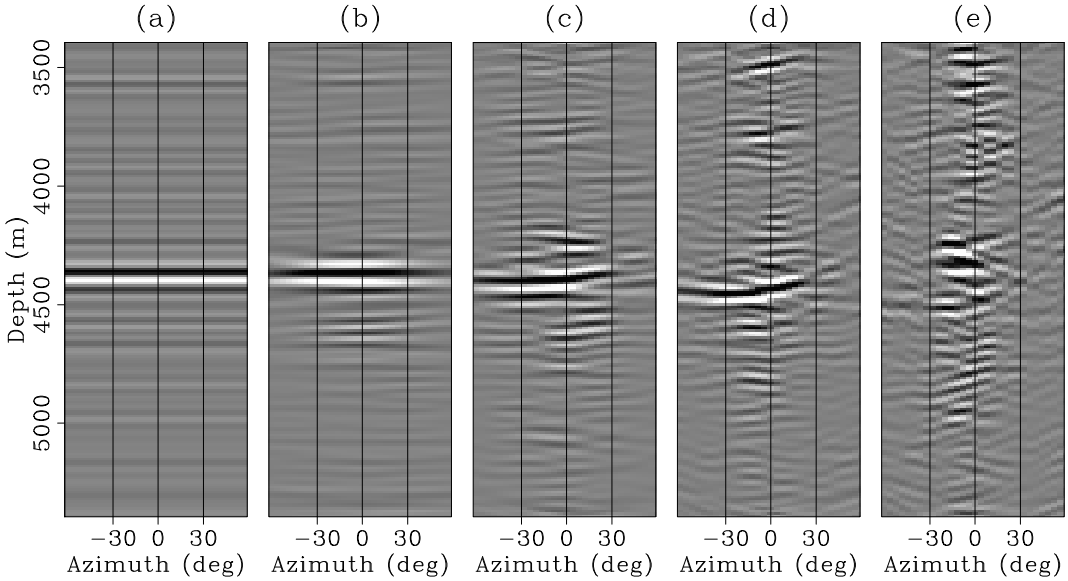


Figure 5.17: 3D angle gathers as a function of azimuth for aperture angles of 0, 5, 10, 15 and 20 degrees (panels (a) through (e)). The gather is taken at CMP_X=11000 m and CMP_Y=13000 m. 3dreal-3d_az_11000_13000 [CR]

both figures the moveout of the primaries is flat at all the azimuths that illuminate the reflector whereas the multiple shows the expected over-migrated moveout. It is interesting to see that the multiple essentially disappears in panel (e) of Figure 5.18 indicating that it was not illuminated at that azimuth (at least not in the aperture range of 0 to 20 degrees). This is somewhat in contrast to the results for the synthetic data in Chapter 4 that indicated that the multiple was illuminated with an azimuth range similar to that of the primary (compare the depth slices in panels (a) and (b) of Figure 4.18. This is not the case with this real data (compare the depth slices in panels (a) and (b) of Figure 5.15) for which the multiples seem to be illuminated preferentially at small aperture angles. A similar behavior is well known with 2D data.

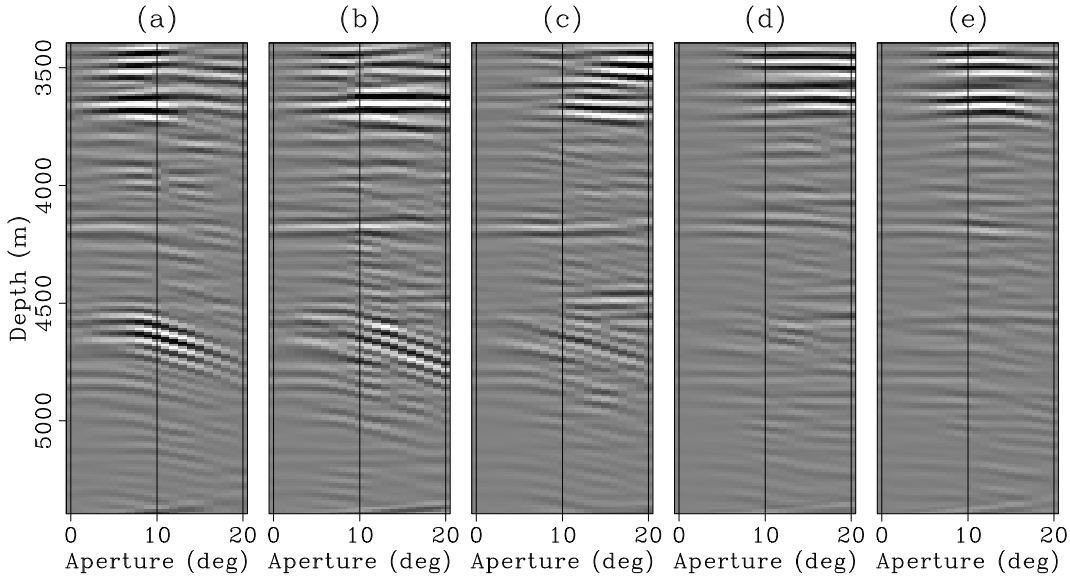


Figure 5.18: 3D angle gathers as a function of aperture angle for reflection azimuths of -40, -20, 0, 20 and 40 degrees (panels (a) through (e)). The gather is taken at CMP_X=13000 m and CMP_Y=13000 m. 3dreal-3d_ap_13000_13000 [CR]

## DISCUSSION

The results of Chapter 4 indicated that we could discriminate between primaries and multiples in inline subsurface offset gathers but perhaps not in the crossline subsurface offset. In this chapter I showed that we can discriminate between primaries and multiples in both subsurface

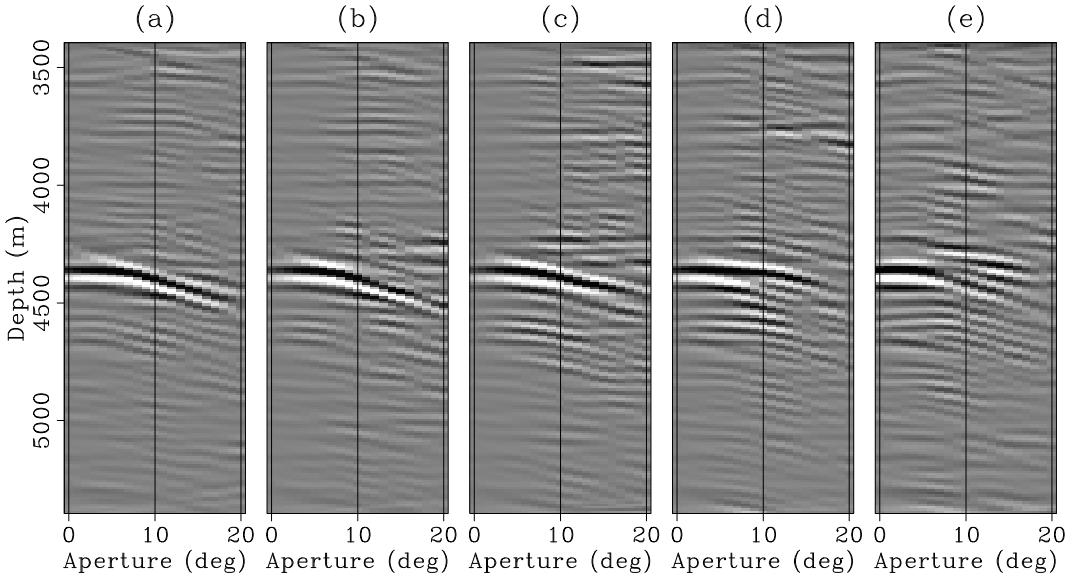


Figure 5.19: 3D angle gathers as a function of aperture angle for reflection azimuths of -40, -20, 0, 20 and 40 degrees (panels (a) through (e)). The gather is taken at CMP_X=11000 m and CMP_Y=13000 m. 3dreal-3d_ap_11000_13000 [CR]

offset directions if there is enough crossline dip.

A full 3D migration with large inline and crossline migration apertures is necessary to correctly image the multiples. To attenuate the multiples we need to compute prestack image gathers as a function of subsurface offset or aperture and azimuth angles. Below salt both primaries and multiples are illuminated only by a narrow range of aperture angles. This makes the difference in moveout between primaries and multiples relatively small. In fact, if we consider only inline subsurface offset gathers at zero crossline subsurface offset and vice-versa, the difference in moveout may indeed be too small. But we need to remember that in a way that is the worst case scenario because the difference between the moveout of primaries and multiples in inline subsurface offsets is larger at non-zero crossline subsurface offsets and vice-versa. Similarly for the 3D ADCIGs.

It is challenging to fully appreciate all the information in the five-dimensional SODCIGs or ADCIGs and just looking at individual planes gives only glimpses of the true difference between the primaries and the multiples. The main message of this chapter is that we can

indeed discriminate between them even for subsalt reflections. In the next chapter I go into the craft of actually attenuating the multiples in the Radon domain.

## CONCLUSIONS

Complex subsurface distorts multiples and make their identification difficult in the image space. SODCIGs help in discriminating between primaries and multiples but are expensive to compute. 3D ADCIGs are even more expensive to compute but can be used to attenuate the multiples as will be shown in the next chapter.

## ACKNOWLEDGMENTS

I would like to thank CGGVeritas for providing the dataset and Dr. Jan Pajchel of Norsk Hydro for providing the velocity model and for his help in securing permission to use the dataset.

# Chapter 6

# Attenuation of subsalt multiples with Gulf of Mexico dataset

**SUMMARY**

In Chapter 5 I showed, with the real 3D dataset, that multiples could be identified relatively easily in SODCIGs and ADCIGs even below salt. In this chapter I will show the results of attenuating the subsalt multiples in both SODCIGs and ADCIGs. A reasonably good level of multiple attenuation is achieved by simply muting the multiple energy that mapped away from zero subsurface offsets and stacking the results. This simple strategy do not completely attenuate the multiples, but provide a quick and dirty way of getting a reasonably accurate estimate of the primaries. Better results can be achieved by going to the expense of applying Radon filtering in 3D-ADCIGs. I applied the same approach used in 2D in Chapter 2 on azimuth-stacked ADCIGs. The results are good. Some multiple energy remains, but the bulk of it is well attenuated. A full 3D Radon transform that accounts for azimuth and aperture angle has the potential for even better attenuation of the multiples but it would be very computer intensive.

## INTRODUCTION

The standard migrated cube corresponds to zero inline and zero crossline subsurface offset and therefore avoids the bulk of the multiples which migrate away from zero subsurface offset in both directions. We could also think of this migrated cube as analogous (although not equal) to an angle stack. The stack itself is effective in attenuating some of the multiples, especially at large aperture angles. A direct way to improve the power of the stack is to mute the multiple energy that mapped away from zero subsurface offsets and stacking the results. The idea is that, specially under salt, primaries are not just migrated to zero subsurface offsets but to a small region around them. By stacking in SODCIGs we can improve the relative amplitudes of the primaries and the residual multiples. This simple strategy does not completely attenuate the multiples, but provides a quick way of getting a reasonably accurate estimate of the primaries.

In order to improve the level of multiple attenuation, I apply Radon filtering in 3D-ADCIGs. I applied the same method described for 2D data in Chapter 2 on azimuth-stacked ADCIGs. This is appropriate because the primaries are flat for those azimuths that illuminate them. I show that the multiples exhibit nice obvious curvature as a function of the aperture angle and therefore are well focused in the Radon domain. As I did in Chapter 2, I then muted out the primaries in the Radon domain to estimate a multiple model. Subtraction from the data provides an estimate of the primaries. These estimates were then used to adaptively match and subtract the multiples in the way presented in Chapter 3. The results are good, with most of the multiple energy being attenuated.

## MULTIPLE ATTENUATION IN SODCIGS

Since multiples map away from zero in inline and crossline subsurface offsets whereas the primaries map near zero subsurface offset when migrated with an accurate primary velocity, there is an opportunity to attenuate the multiples directly in SODCIGs without having to compute 3D-ADCIGs, apply Radon filtering, and do adaptive matching. This would not only be easier but also much less expensive. We have a good approximation for the residual moveout of the multiples in SODCIGs so we could apply a Radon transform directly to the SODCIGs

to focus the multiples. The problem is that, unlike in ADCIGs, the primaries do not have flat residual moveout. Applying a Radon transform would map the primaries to all curvatures in the Radon domain, thus making it difficult to separate them from the multiples. An even simpler alternative is to apply a tapered mute in SODCIGs as a function of subsurface offsets to get rid of anything that mapped away from zero inline and zero crossline subsurface offset. Stacking the muted SODCIGs should, therefore, attenuates some of the multiples. We cannot expect to get rid of the multiples completely, because some energy from the multiples map into the same region as the primaries, especially in crossline subsurface offsets.

Figure 6.1 shows a comparison of an inline section taken at crossline position CMP-Y=13200 m of the stacked cube of the un-muted SODCIGs (panel (a)) and the muted SODCIGs (panel (b)). Muting the large subsurface offsets resulted in a stacked section where the primaries are better defined and the main multiple is moderately attenuated (pointed to by the arrow). We know from Chapter 5 that this is a strong multiple. This multiple had little curvature in the crossline subsurface offsets and therefore survived the mute and stack process. Likewise, Figure 6.2 shows the comparison on a crossline section taken at CMP-X=13300 m. Again, the main multiple, pointed to by the arrow, has been only moderately attenuated. In general, multiple attenuation directly in SODCIGs leaves significant residual multiple energy and is only a quick and inaccurate solution.

It should be noticed that we do not usually stack the SODCIGs. The zero inline and zero crossline subsurface offset cube should be a good approximation to the angle stack in a manner analogous to a CMP stack section being a good approximation to the zero offset section in data space. I am stacking the SODCIGs here simply to illustrate that the difference in the mapping of the primaries and the multiples is so large in SODCIGs that a good level of multiple attenuation can be achieved simply by muting and stacking. I am assuming that the primaries were migrated with a migration velocity accurate enough that they do not have significant curvature in SODCIGs, which is consistent with the results of Chapter 5.

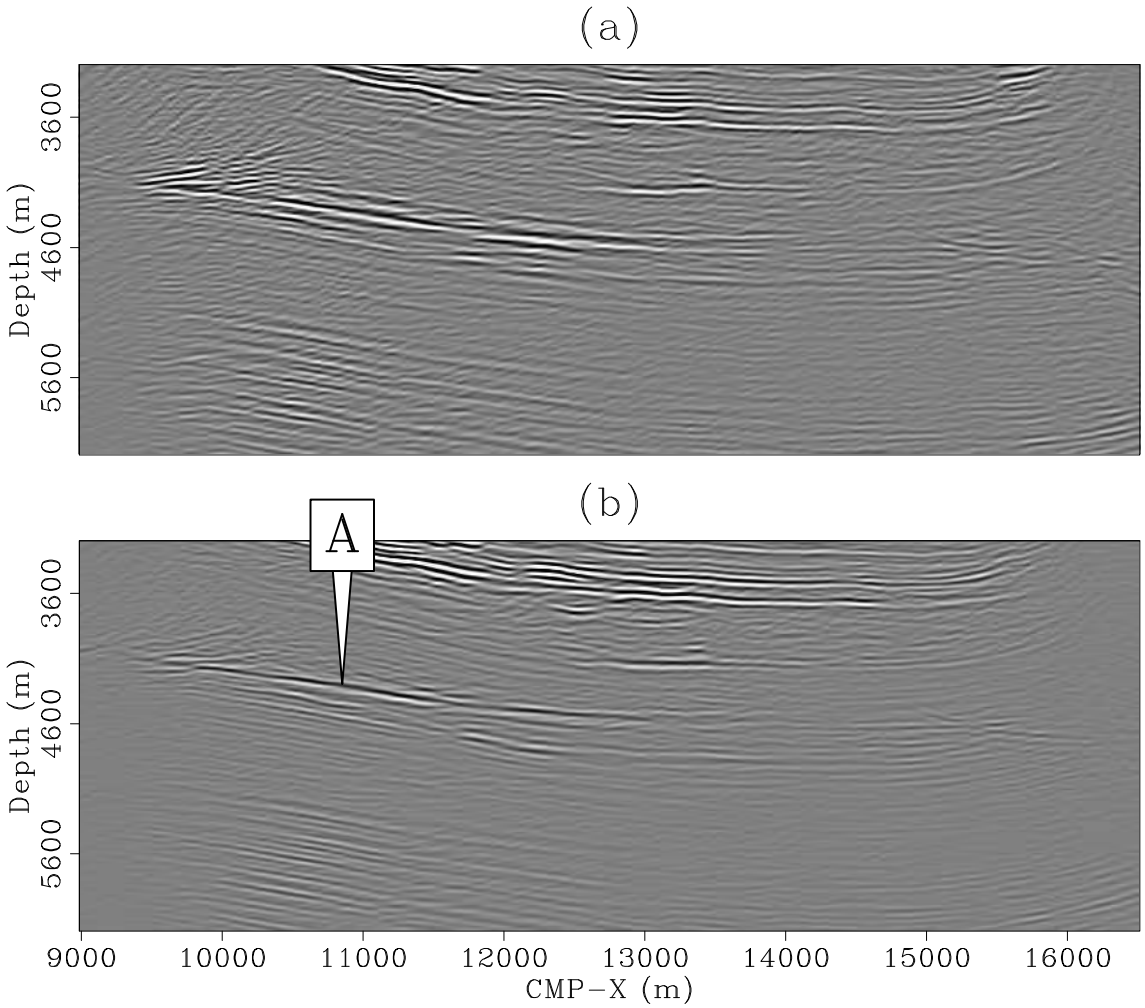


Figure 6.1: Comparison of stacked SODCIGs for Inline section at CMP-Y=13200 m. Panel (a) corresponds to un-muted SODCIGs and contains primaries and multiples. Panel (b) corresponds to the muted SODCIGs and should have less energy from the multiples. The arrow points to the main multiple that was only moderately attenuated. 3dreal2-inline_sodcig_stk_13200 [CR]

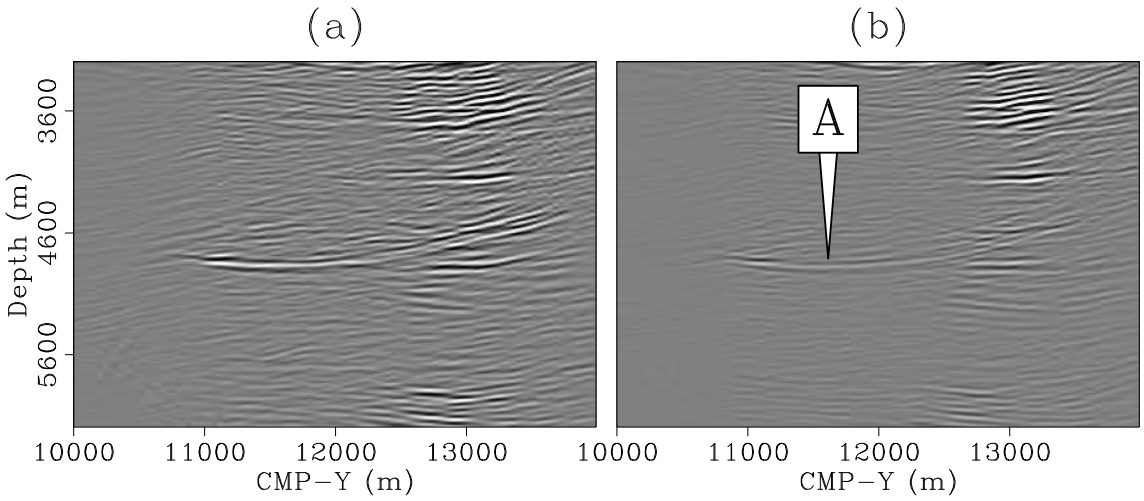


Figure 6.2: Comparison of stacked SODCIGs for crossline section at CMP-X=13300 m. Panel (a) corresponds to un-muted SODCIGs while panel (b) corresponds to the muted SODCIGs. The strong multiple, pointed to by the arrow, was attenuated but not eliminated. 3dreal2-xline_sodcig_stk_13300 [CR]

## MULTIPLES IN RADON DOMAIN

I showed in the previous section that some level of multiple attenuation was possible in the image space without Radon filtering, but much of the multiple energy remained. In order to improve the level of multiple attenuation, Radon filtering is necessary. In this section I apply a direct extension of the Radon transform presented in Chapter 2.

The primaries in 3D angle gathers as a function of azimuth, for large aperture angles, are localized to the reflection azimuth of the reflecting plane. The multiples, on the other hand, due to the effect of crossline dip, may have strong moveout as a function of azimuth except at zero aperture angle for which there is no azimuth resolution. This was shown for the synthetic dataset in Chapter 4 and again in Figure **??**. Exploiting this variation, however, is not easy, since the multiple trajectory is hard to approximate by an explicit equation of the type presented in Chapter 2. Instead, I applied the Radon transform to 3D ADCIGs after stacking over azimuth. Figure 6.3 shows two 3D ADCIGs (stacked over azimuth) along with the envelopes of their Radon transforms. Planes (a) and (b) correspond to the ADCIG at

location CMP-X=10000, CMP-Y=12000 whereas panels (c) and (d) correspond to the ADCIG at CMP-X=13800 CMP-Y=13000. Panels (a) and (b) are meant to illustrate a location in which the multiple dominates and little primary energy is present. Panels (c) and (d), on the other hand, illustrate a location where significant primary energy exits. It is very encouraging that the moveout of the multiple in ADCIGs is so well defined and therefore well focused in the Radon domain. Notice how the Radon transform nicely maps the multiples in both panels (b) and (d) away from zero curvature, thus separating them from the primaries (at zero curvature, see for example the top of panel (d)).

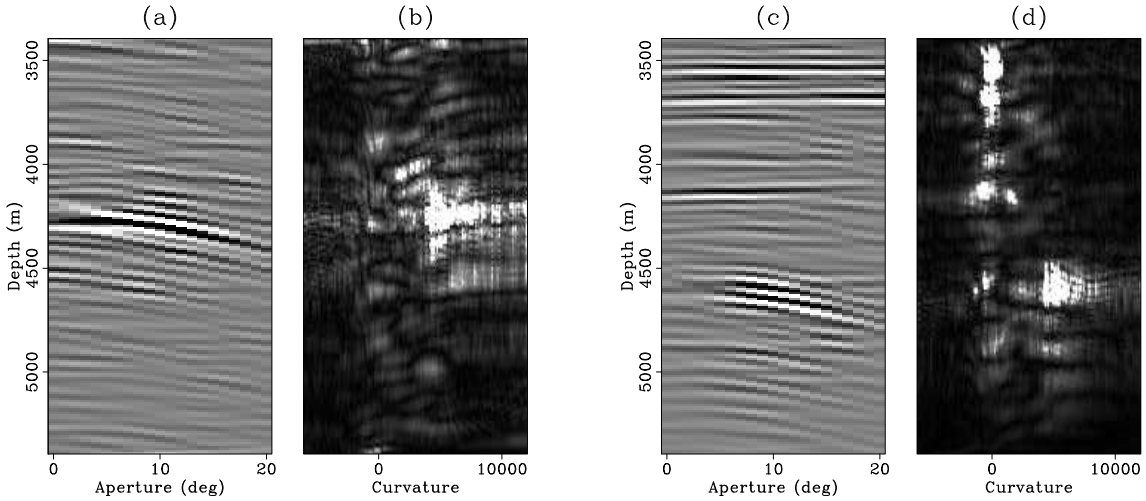


Figure 6.3: Radon transform of two azimuth-stacked 3D ADCIGs. Panel (a) is the ADCIG at CMP-X=10000 CMP-Y=12000 and panel (b) is its Radon transform. Panel (c) is the ADCIG at CMP-X=13800 CMP-Y=13000 and panel (d) is its Radon transform. 3dreal2-radon_10000_12000_13800_13000 [CR]

In the next section I will show the multiple models obtained by muting the primary region in the Radon domain and taking the inverse transform just as I showed in Chapter 2.

## MULTIPLE ATTENUATION ON ANGLE GATHERS

In this section I will show the results of multiple attenuation computed with azimuth-stacked 3D angle gathers.

**Results on ADCIGs**

Figure 6.4 shows a comparison of the ADCIG at CMP_X=10000 and CMP_Y=12000 m stacked over azimuth (as in panel (a) of Figure 6.3 but plotted with a different clip value), the initial estimate of the multiples (panel (b)), the initial estimate of the primaries (panel (c)), the matched estimate of the multiples (panel (d)) and the matched estimate of the primaries (panel (e)). The matched estimates of primaries and multiples were computed with the algorithm presented in Chapter 3. The effect of matching is not too striking because our version of the Radon transform is optimized to produce amplitudes close to the model. Nonetheless, notice that the matching mapped back to the multiple panel the residual multiple energy that contaminated the initial estimate of the primaries (just below 6000 m depth in panel (c)). Compare panel (c) and (e). Figure 6.5 shows a similar comparison for the ADCIG taken at CMP-X=13800 m CMP-Y=13000 m as in panel (c) of Figure 6.3. The multiple is well recovered.

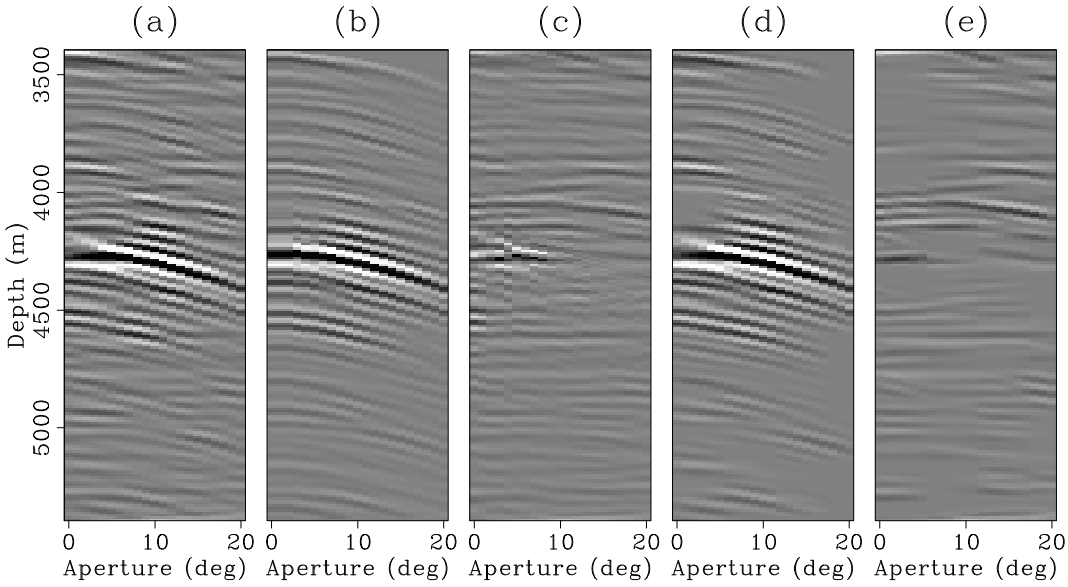


Figure 6.4: Multiple attenuation in ADCIG at CMP_X=10000 and CMP_Y=12000 m. Panel (a) is the original ADCIG. Panel (b) is the initial multiple estimate. Panel (c) is the initial primary estimate. Panel (d) is the matched multiple estimate and panel (e) is the matched primary estimate. 3dreal2-comp-2d-ap-10000-12000 [CR]

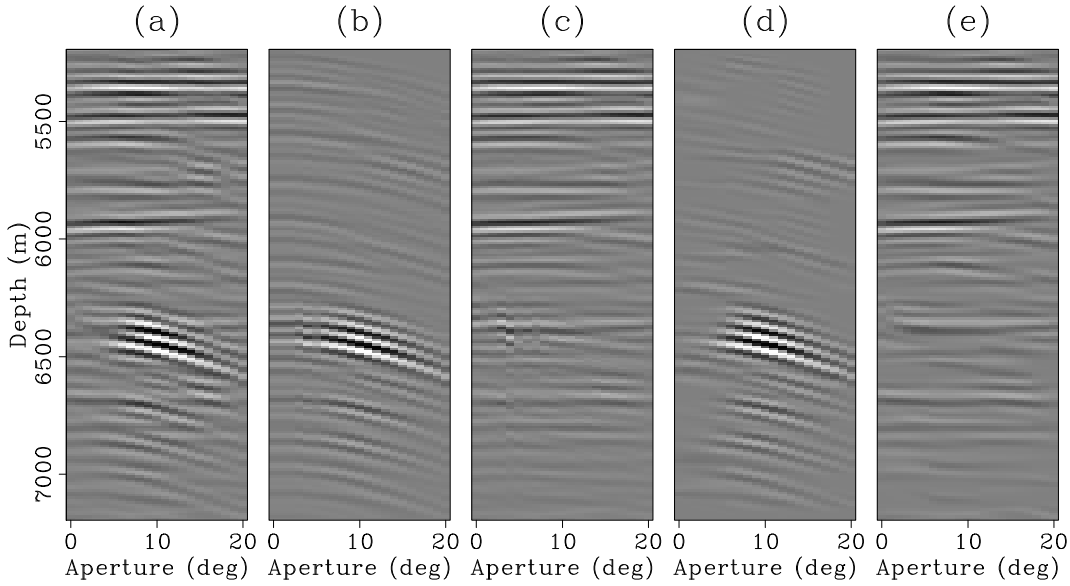


Figure 6.5: Multiple attenuation in ADCIG at CMP_X=13800 and CMP_Y=13000 m. Panel (a) is the original ADCIG. Panel (b) is the initial multiple estimate. Panel (c) is the initial primary estimate. Panel (d) is the matched multiple estimate and panel (e) is the matched primary estimate. 3dreal2-comp-2d-ap-13800-13000 [CR]

**Results on inline sections from the angle stacked-cube**

To assess the level of multiple attenuation on the stacked images, I applied the Radon filtering approach to all the azimuth-stacked 3D ADCIGs and stacked them over aperture angle. I will show the results of the multiple attenuation on three inline angle stacks. Panel (a) of Figure 6.6 shows the inline angle stack at CMP_Y=11600 m before multiple attenuation. Panel (b) shows the angle stack of the matched multiples and panel (c) shows the angle stack of the matched primaries. The main multiple reflection has been nicely attenuated and, above CMP-X=10000 m we seem to have uncovered a weak flattish primary (pointed by arrow A). The oval points to residual multiple energy that intersects another weak primary.

Figure 6.7 shows a similar comparison for the inline angle stack at CMP-Y=12400 m. In this section there are two strong multiples. One on the left hand side (see panel (b)), which seems to be the same multiple in panel (b) of Figure 6.6, and the flat event cutting across the primary reflections on the right hand side of panel 6.7(b). Both multiples have been attenuated

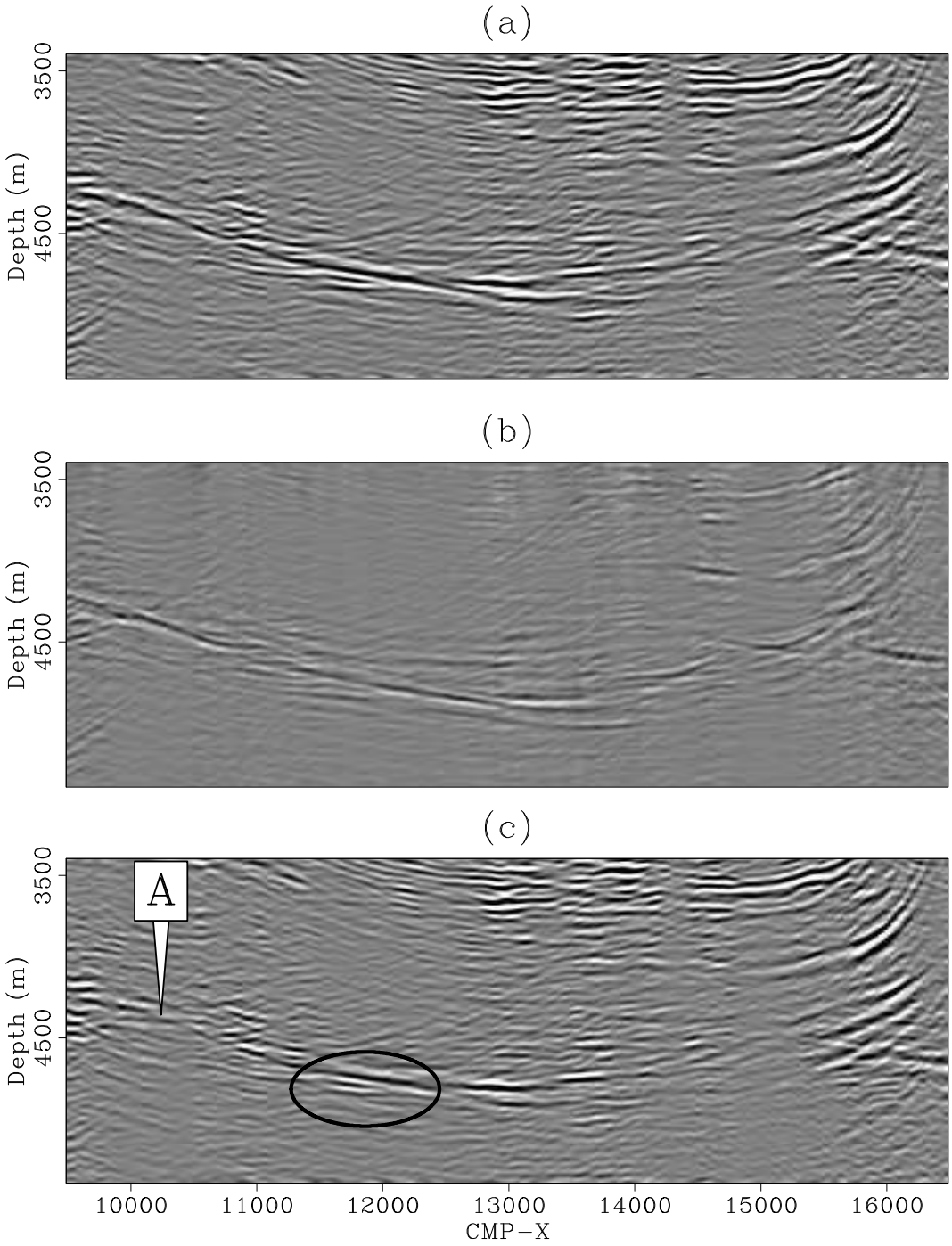


Figure 6.6: Inline angle stack at CMP_Y=11600 m. Panel (a) is the angle stack of the original data while panel (b) is the angle stack of the matched multiples and panel (c) is the angle stack of the matched primaries. 3dreal2-comp-2d-inline-stack-11600 [CR]

although not completely eliminated. Arrows A and B point to the weak residual energy from each multiple. Notice also on the left-hand side of panel 6.7(b) what appear to be diffractions. These could be diffracted multiples that were imperfectly attenuated (see panel 6.7(c)). There was some evidence of the presence of diffracted multiples in a few prestack images but because of computer limitations no attempt was made to target them with the apex-shifted Radon transform of Chapter 2.

Figure 6.8 shows a similar comparison for the inline angle stack at CMP-Y=13200 m. In this section we again see one strong multiple that seems to be the same in shown in the previous two sections (panel (b) of Figures 6.6 and 6.7). Here again, the attenuation of the multiple has uncovered a weak primary (pointed by arrow A). Although the attenuation of the multiple was successful, some weak residual energy remains pointed to by arrow B.

**Results on crossline sections from the angle-stacked cube**

Although the quality of the migrated image in the crossline direction is not very good, it is still important to assess the level of multiple attenuation in crossline sections taken from the angle stack. I will show the results for three crossline sections.

Panel (a) of Figure 6.9 shows the crossline angle stack at CMP_X=13300 m before multiple attenuation. Panel (b) shows the angle stack of the matched multiples and panel (c) shows the angle stack of the matched primaries. Here also, the multiple has been nicely identified despite the poor signal-to-noise ratio. Some energy from the multiple remains as indicated by the ovals.

Figure 6.10 shows a similar comparison for the crossline angle stack at CMP-Y=15500 m. Again, most of the multiple has been attenuated although some still remains on the left edge as indicated by the oval. Notice also at the top of panel (b) that some energy from the primary leaked into the multiples.

Figure 6.11 shows a similar comparison for the crossline angle stack at CMP-X=15500 m. This section has a different character than the previous two and multiples would have been even more difficult to identify. There seem to be two different multiples, one coming from the

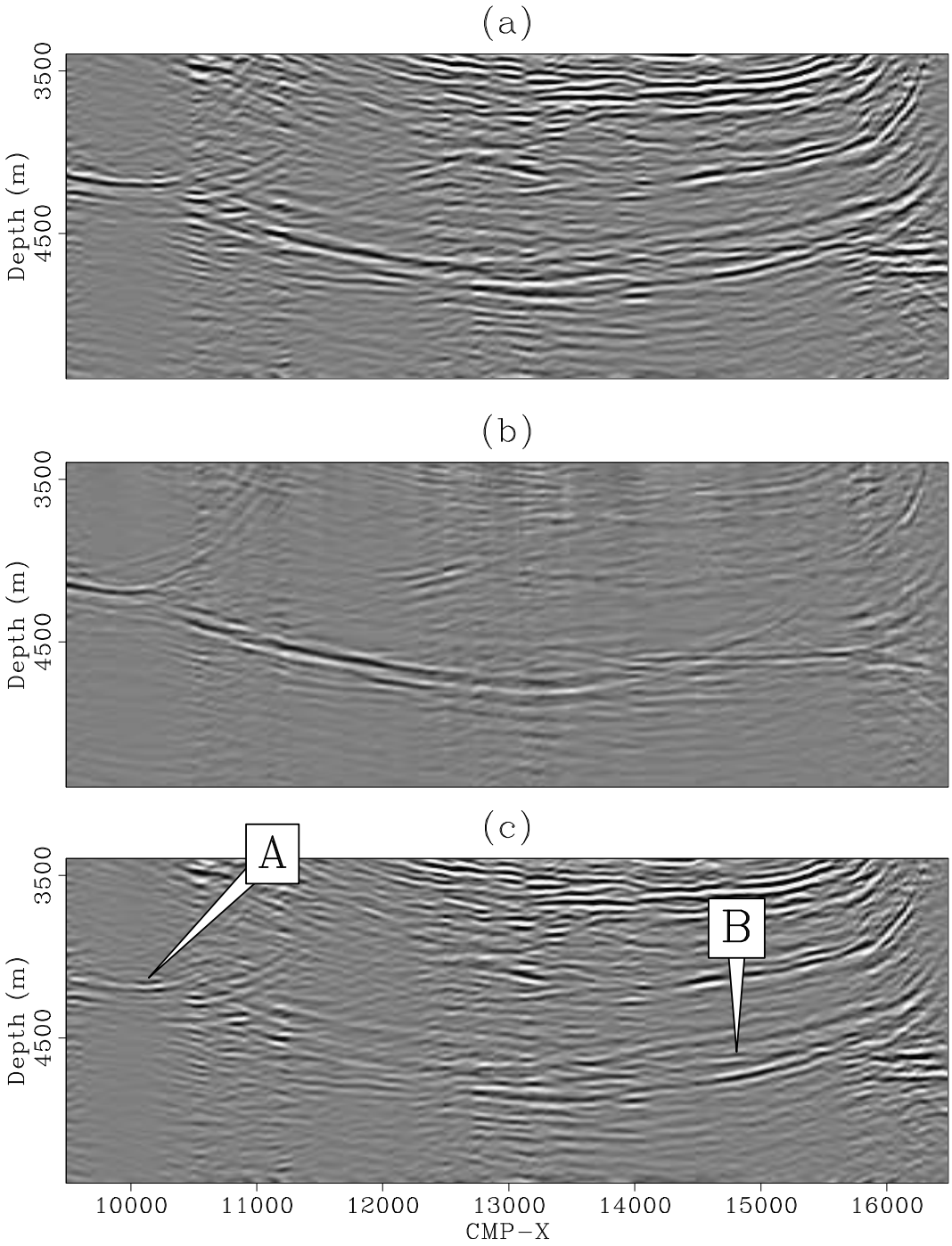


Figure 6.7: Inline angle stack at CMP_Y=12400 m. Panel (a) is the angle stack of the original data while panel (b) is the angle stack of the matched multiples and panel (c) is the angle stack of the matched primaries. 3dreal2-comp-2d-inline-stack-12400 [CR]

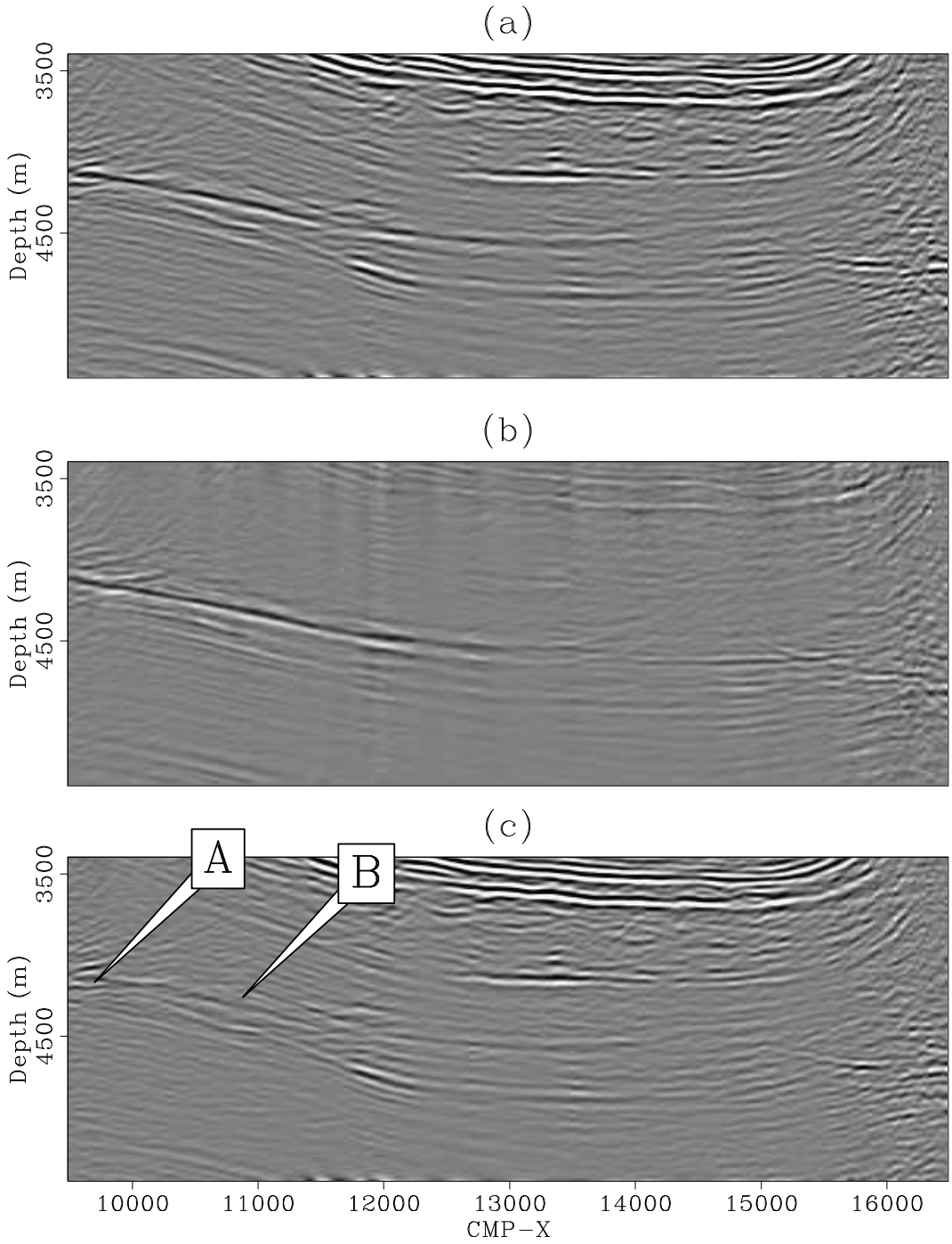


Figure 6.8: Inline angle stack at CMP_Y=13200 m. Panel (a) is the angle stack of the original data while panel (b) is the angle stack of the matched multiples and panel (c) is the angle stack of the matched primaries. 3dreal2-comp-2d-inline-stack-13200 [CR]

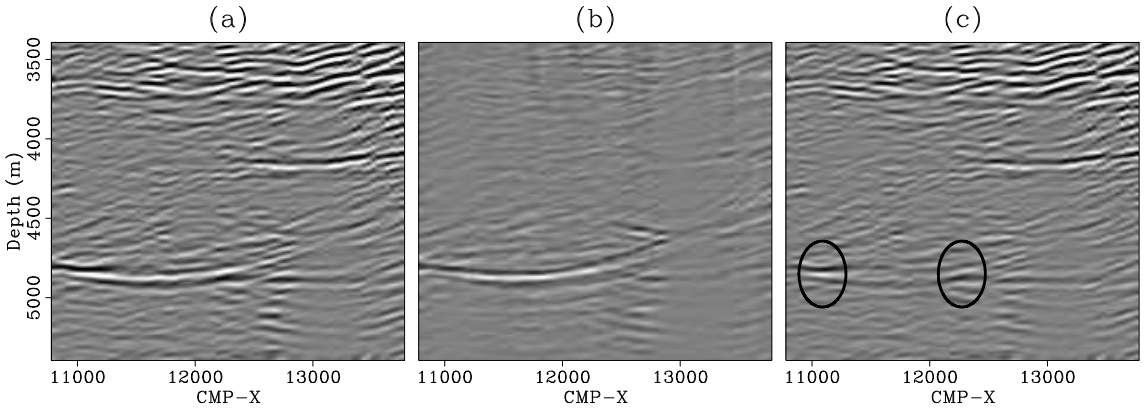


Figure 6.9: Crossline angle stack at CMP_X=13300 m. Panel (a) is the angle stack of the original data while panel (b) is the angle stack of the matched multiples and panel (c) is the angle stack of the matched primaries. The ovals point to residual multiples. 3dreal2-comp-2d-xline-stack-13300 [CR]

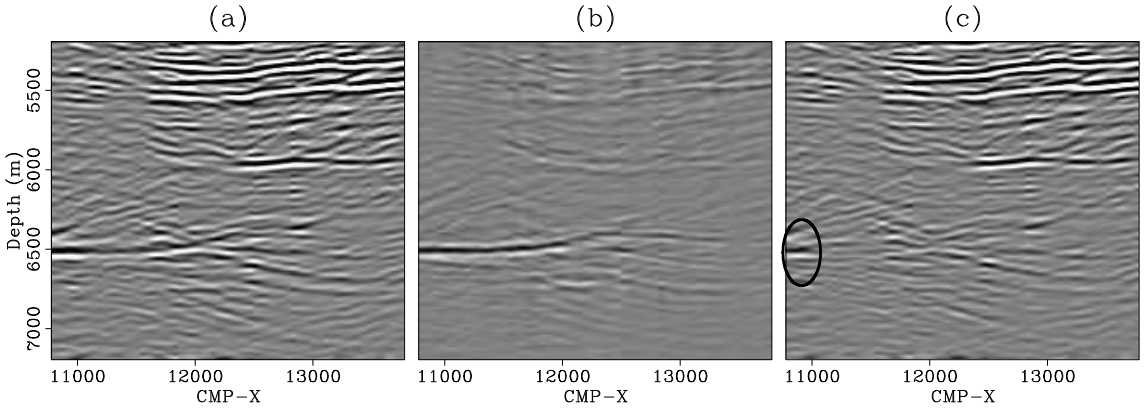


Figure 6.10: Crossline angle stack at CMP_X=14400 m. Panel (a) is the angle stack of the original data while panel (b) is the angle stack of the matched multiples and panel (c) is the angle stack of the matched primaries. 3dreal2-comp-2d-xline-stack-14400 [CR]

left end which may be the same in the previous two sections and another one below it in the middle of the section. Subsalt multiples are so broken up that it is hard to say if these two multiple segments could come from different multiple-generating interfaces or from the same one. The oval points at residual multiple energy.

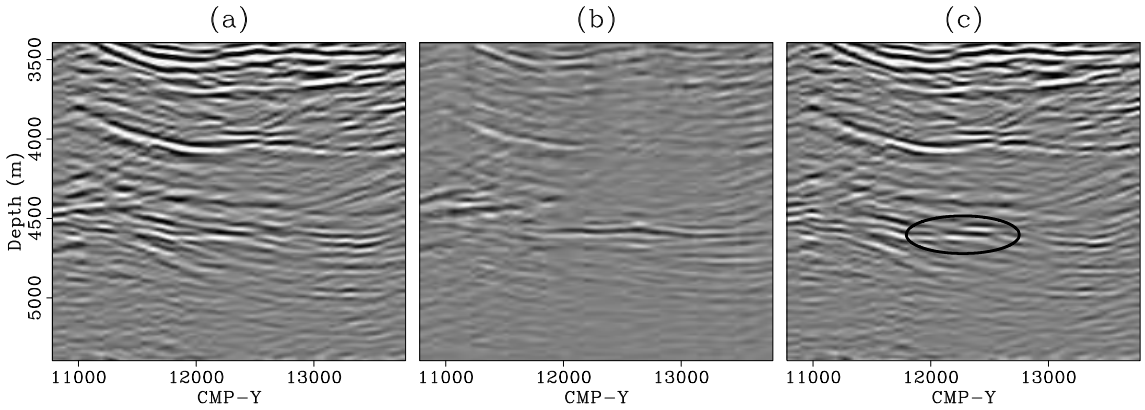


Figure 6.11: Crossline angle stack at CMP_X=15500 m. Panel (a) is the angle stack of the original data while panel (b) is the angle stack of the matched multiples and panel (c) is the angle stack of the matched primaries. The oval points at residual multiple energy 3dreal2-comp-2d-xline-stack-15500 [CR]

## DISCUSSION

Muting out the most significant energy contribution from the multiples directly in SODCIGs is an easy but not very accurate way of attenuating the multiples. The problem arises because part of the multiple energy maps close to zero inline and especially crossline subsurface offsets. The higher the dips in the inline and crossline direction, the better the chances of the multiples mapping away from the zero inline and crossline subsurface offsets where the primaries map and the better the chances to estimate a reasonably accurate multiple model with this straight forward approach. The approach is more likely to fail for subsalt multiples because of poor illumination of both the primaries and the multiples. Primaries in particular are more likely to be spread around the zero subsurface offsets rather than been nicely focused. Errors in migration velocity also cause the primaries to not focus tightly around zero subsurface offsets. Muting the SODCIGs is therefore unlikely to give an acceptable level of multiple attenuation

in the more challenging situations where data space methods are more likely to fail

Converting the SODCIGs to ADCIGs allows the computation of an accurate multiple model provided that the primaries were illuminated at large enough aperture angles to provide good discrimination with respect to the multiples. I showed here that even though the multiples were illuminated only by aperture angles less than 20 degrees that was enough to separate them from the primaries in the Radon domain. Radon filtering in true ADCIGs is the best way to exploit the moveout difference between primaries and multiples. Choosing the Radon parameters is not trivial but involves the same considerations that were pointed out in the discussion section of Chapter 2 so I will not repeat them here.

I would like to point out that there is room to improve the results of the multiple attenuation further by either of two changes to the approach I used here: (1) we could design yet another Radon kernel that directly maps the entire ADCIG into the Radon transform as function of one or two global curvature parameters. This will be a very computer intensive approach since the non-linear inversion used in computing the sparse Radon transform will then have to be done in a higher-dimensional space. The mute pattern will also be more difficult to design and apply. These are research ideas that may provide better results although with much more effort and computer cost. (2) we could apply the 2D version of the apex-shifted Radon filtering to the azimuth-stacked ADCIGs or an apex-shifted full 3D version of the Radon filtering to the 3D ADCIGs. This will obviously be an extremely computer intensive problem but is the most accurate and flexible application of the method to target both the specular and the diffracted subsalt multiples.

## CONCLUSIONS

Multiple attenuation in the image space is effective even below salt. Radon filtering of azimuth-stacked ADCIGs is a reasonable compromise between accuracy and computer cost that produces a very nice level of multiple attenuation.

**ACKNOWLEDGMENTS**

I would like to thank CGGVeritas for providing the dataset and Dr. Jan Pajchel of Norsk Hydro for providing the velocity model and for his help in securing permission to use the dataset.

# Chapter 7

# Conclusions

The attenuation of multiples reflections in complex subsurface areas is best done in the image space. This domain is smaller, regular, and the primaries are guaranteed to map to well known regions: near zero subsurface offsets in SODCIGs and to flat, well focused events in ADCIGs. Multiples have predictable (to first order) residual moveout in this domains and we can separate them from the primaries in the Radon domain.

In Chapter 2 I showed the approach in detail for the 2D case. I presented the equations for the residual moveout of the specular water-bottom multiples in SODCIGs and ADCIGs and use them to design a new Radon kernel that improves the focusing of the multiples in that domain. I attenuated specular and diffracted multiples with synthetic and real data using an apex-shifted version of the Radon transform.

Before subtracting the estimated multiples from the data to estimate the primaries, we need to make sure that differences in phase and amplitude between the data and the multiple model are taken into account. In Chapter 3 I presented a new approach to simultaneously match estimates of multiples and primaries to the data. I posed the adaptive matching as a least-squares problem to estimate non-stationary filters for both the primaries and the multiples. The process is iterative with the estimates of the primaries and multiples being updated every time the least-squares solution is found. I showed that we can get good results with relatively few iterations and illustrated the method with synthetic and real data.

I extended the ideas of Chapter 2 to 3D in Chapter 4 and used a synthetic 3D prestack dataset to illustrate the mapping of both primaries and multiples to SODCIGs and ADCIGs. In particular I showed that primaries and multiples behave differently in ADCIGs not only as a function of aperture angle but also as function of azimuth. While the azimuth resolution of primaries increases with the increase of aperture angle, the multiples never show any azimuth resolution at all. This is a consequence of the crossline dip that prevents them from traveling in a single plane even in constant velocity.

In Chapter 5 I illustrate the mapping of subsalt primaries and multiples from a real 3D dataset from the Gulf of Mexico. The five-dimensional prestack image cubes of SODCIGs or ADCIGs are challenging to visualize on paper but I showed that, similar to the results in 2D and with the 3D synthetic example, the multiples map away from zero subsurface offsets in SODCIGs and with non-flat residual moveout as a function of aperture angle in ADCIGs. SODCIGs are shown to be a simple but useful tool in identifying multiples and telling them apart from primaries. I also showed that, despite the relatively narrow range of aperture angles that illuminate both the primaries and the multiples, enough difference in residual moveout exists between them to make it possible to attenuate the multiples in the Radon domain.

For the sake of computer time, I applied the Radon filtering on azimuth-stacked ADCIGs. The final results of the multiple attenuation, presented in Chapter 6, show that the most significant multiples were indeed attenuated. I showed that on individual azimuth-stacked ADCIGs as well as inline and crossline sections. Most of the multiple energy was attenuated but some multiple energy remained and some weak energy from the primaries still mapped into the multiples.

I believe that there is ample opportunity to refine the basic procedure I developed in this thesis and I look forward to seeing improvements from other researchers. Attenuation of multiples is still a germane problem in our industry.

# Appendix A

# Traveltime of refracted rays

In this Appendix I derive equations 2.7 and 2.8. From equation 2.5 we have:

$$t_{s_1}\cos\alpha_s + \rho\tilde{t}_{s_2}\cos\beta_s = t_{r_1}\cos\alpha_r + \rho\tilde{t}_{r_2}\cos\beta_r, \tag{A.1}$$

and, from the imaging condition (the sum of the traveltime of the extrapolated rays at the image point has to be equal to the traveltime of the multiple) we have

$$t_{s_2} + t_{r_2} = \tilde{t}_{s_2} + \tilde{t}_{r_2}. \tag{A.2}$$

Solving those two equations for $\tilde{t}_{s_2}$ and $\tilde{t}_{r_2}$ we get

$$\tilde{t}_{s_2} = \frac{t_{r_1}\cos\alpha_r - t_{s_1}\cos\alpha_s + \rho(t_{s_2}+t_{r_2})\cos\beta_r}{\rho(\cos\beta_s+\cos\beta_r)}, \tag{A.3}$$

$$\tilde{t}_{r_2} = \frac{t_{s_1}\cos\alpha_s - t_{r_1}\cos\alpha_r + \rho(t_{s_2}+t_{r_2})\cos\beta_s}{\rho(\cos\beta_s+\cos\beta_r)}. \tag{A.4}$$

It is interesting to check these equations in two particular cases:

1. For a specular multiple from a flat water-bottom, we have $\alpha_s = \alpha_r$, $\beta_s = \beta_r$, $t_{s_1} = t_{s_2} = t_{r_2} = t_{r_1}$ and therefore we get $\tilde{t}_{s_2} = t_{s_2}$ and $\tilde{t}_{r_2} = t_{r_2}$ as the geometry of the problem requires. Notice that this is true for any $\rho$.

2. For a specular water-bottom multiple migrated with water velocity ($\rho = 1$), we have $\beta_s = \alpha_s$ and $\beta_r = \alpha_r$. Furthermore, since the multiple behaves as a primary, $(t_{s_1} + t_{s_2})\cos\alpha_s = (t_{r_1} + t_{r_2})\cos\alpha_r$ and we again get $\tilde{t}_{s_2} = t_{s_2}$ and $\tilde{t}_{r_2} = t_{r_2}$.

# Appendix B

# Image Depth in ADCIGs

Figure B.1 shows the basic construction to compute the image depth in ADCIGs based on the image depth in SOCIGs. Triangles $ABD$ and $CBD$ are congruent since they have one side common and the other equal because $|AB| = |BC| = h_\xi$. Therefore, $\theta = \pi/2 - \beta_r + \delta$. Also, triangles AED and FCD are congruent because $|AD| = |CD|$ and also $|AE| = |CF|$ (Biondi and Symes, 2004). Therefore, the angle $\delta$ in triangle $DCF$ is the same as in triangle $AED$. We can compute $\delta$ from the condition

$$\begin{aligned} \theta + \delta + \beta_s &= \frac{\pi}{2}, \\ \frac{\pi}{2} - \beta_r + \delta + \delta + \beta_s &= \frac{\pi}{2}, \\ \delta &= \frac{\beta_r - \beta_s}{2}. \end{aligned}$$

The depth of the image point in the ADCIG, from triangle ABC, is therefore

$$z_{\xi_\gamma} = z_\xi + z^* = z_\xi + (\text{sign}(h_\xi)) h_\xi \cot\left(\frac{\pi}{2} - \beta_r + \delta\right). \tag{B.1}$$

Replacing the expression for $\delta$ we get, after some simplification (and taking $\text{sign}(h_\xi) = -1$)

$$z_{\xi_\gamma} = z_\xi + z^* = z_\xi - h_\xi \tan\left(\frac{\beta_r + \beta_s}{2}\right) = z_\xi - h_\xi \tan(\gamma). \tag{B.2}$$

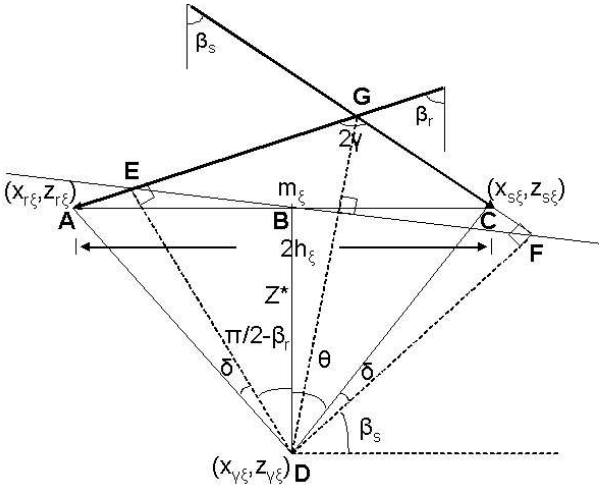


Figure B.1: Sketch to show the computation of the image depth in an ADCIG. append-mul_sktch17 [NR]

# Appendix C

# Residual Moveout in ADCIGs

In this appendix I show that, for a flat reflector, the residual moveout of the multiples in ADCIGs reduces to the tangent-squared expression derived by Biondi and Symes (2004) for the residual moveout of under-migrated primaries:

$$\Delta \mathbf{n}_{\mathrm{RMO}} = (\rho - 1)\tan^2\gamma\, z_0 \mathbf{n}. \tag{C.1}$$

Start with Equation 2.23

$$z_{\xi_\gamma} = \frac{z_{\xi_\gamma}(0)}{1+\rho}\left[1 + \frac{\cos\gamma(\rho^2 - (1-\rho^2)\tan^2\gamma)}{\sqrt{\rho^2 - \sin^2\gamma}}\right], \tag{C.2}$$

where $z_{\xi_\gamma}(0)$ is the normal-incidence migrated-depth, (*i.e.* $z_0$) in the previous equations.

There is an important and unfortunate difference in notation here, however, because $\rho$ in equation C.1 is the ratio of the migration to the true *slowness* whereas $\rho$ in equation C.2 is the ratio of the migration to the true *velocity*. Therefore, in order to get a better idea of how the approximation for the RMO of the multiples (accounting for ray bending at the reflector interface) relates to that of the primaries (neglecting ray bending), I rewrite equation C.2 replacing

$\rho$ by $1/\rho$ and $z_{\xi_\gamma}(0)$ with $z_0$ to get:

$$z_{\xi_\gamma} = \left[ \rho + \frac{\cos\gamma(1-(\rho^2-1)\tan^2\gamma)}{\sqrt{1-\rho^2\sin^2\gamma}} \right] \frac{z_0}{1+\rho}. \tag{C.3}$$

Since $\Delta n_{\text{RMO}} = z_0 - z_{\xi_\gamma}$ we get:

$$\Delta n_{\text{RMO}} = \left[ 1 - \frac{\cos\gamma(1-(\rho^2-1)\tan^2\gamma}{\sqrt{1-\rho^2\sin^2\gamma}} \right] \frac{z_0}{1+\rho}. \tag{C.4}$$

For small $\gamma$, $\sin\gamma \approx 0$ and $\cos\gamma \approx 1$, therefore

$$\Delta n_{\text{RMO}} = (\rho^2-1)\tan^2\gamma \frac{z_0}{1+\rho} = (\rho-1)\tan^2\gamma z_0. \tag{C.5}$$

This is the same as equation C.1 save for the unit vector **n**. This result is intuitively appealing because it shows that the approximation of neglecting ray bending at the reflecting interface deteriorates as the aperture angle increases which is when the ray bending is larger.

# Bibliography


Alvarez, G., 2005, Mapping of water-bottom and diffracted 2D multiple reflections to image space, *in* SEP–123.: Stanford Exploration Project 129–154. URL `http://sepwww.stanford.edu/sep/gabriel/Papers/SEP123_gabriel1.pdf`.

—, 2006, Attenuation of 2d specularly-reflected multiples in image space: SEP– **124**.

Alvarez, G., Biondi, B., and Guitton, A., 2004, Attenuation of diffracted multiples in angle-domain common-image gathers, *in* 74th Annual International Meeting: Soc. of Expl. Geophys. 1301–1304.

Artman, B., and Matson, K., 2006, Image-space surface-related multiple prediction, *in* SEP–125: Stanford Exploration Project 47–60.

Baumstein, A., and Hadidi, M., 2006, 3d surface-related multiple elimination: Data reconstruction and application to field data: **71**, E25–E33.

Berkhout, A., and Verschuur, D., 1997, Estimation of multiple scattering by iterative inversion, part i: theoretical considerations: Geophysics, **62**, 1586–1595.

Biondi, B., 2006, Three Dimensional Seismic Imaging: Society of Exploration Geophysicists.

Biondi, B., and Palacharla, G., 1996, 3-d prestack migration of common-azimuth data: Geophysics, **61**, 1822–1832.

Biondi, B., and Symes, W., 2004, Angle-domain common-image gathers for migration velocity analysis by wavefield-continuation imaging: Geophysics, **69**, 1283–1298.

Biondi, B., and Tisserant, T., 2004, 3D angle-domain common-image gathers for migration velocity analysis: Geophysical Prospecting, **62**, 575–591.

Claerbout, J., and Fomel, S., 2002, Image Estimation by Example: Geophysical soundings image construction: Class notes, http://sepwww.stanford.edu/sep/prof/index.html.

Clapp, R., 2004, Reference velocity selection by a generalized lloyd method, *in* 74th Annual International Meeting: Soc. of Expl. Geophys. 981–984.

Curry, W., 2006, Interpolating diffracted multiples with prediction-error filters, *in* 76th Annual International Meeting: Soc. of Expl. Geophys. 2709–2713.

van Dedem, E., and Verschuur, D., 1998, 3d surface-related multiple elimination and interpolation, *in* 68th Annual International Meeting: Soc. of Expl. Geophys. 1321–1324.

Dragoset, W., 1999, A practical approach to surface multiple attenuation: The Leading Edge, **3**, 772–789.

Dragoset, W., and Jericevic, Z., 1998, Some remarks on multiple attenuation: Geophysics, **63**, 772–789.

Foster, D., and Mosher, C., 1992, Suppression of multiple reflections using the radon transform: Geophysics, **57**, 386–395.

Gazdag, J., and Sguazzero, P., 1984, Migration of seismic data by phase-shift plus interpolation: Geophysics, **49**, 124–131.

Guitton, A., 2005a, Multidimensional seismic noise attenuation: Ph.D. thesis, Stanford University.

—, 2005b, Multidimensional seismic noise attenuation: Ph.D. thesis, Stanford University.

Guitton, A., and Symes, W., 2003, Robust inversion of seismic data using the huber norm: Geophysics, **68**, 1310–1319.

Hampson, D., 1986, Inverse velocity stacking for multiple elimination: Canadian Journal of Exploration Geophysicists, **22**, 44–55.

Hargreaves, N., VerWest, B., Wombell, R., and Trad, D., 2003, Multiple attenuation using an apex-shifted radon transform, *in* 74th Annual International Meeting: Soc. of Expl. Geophys. 1929–1932.

Levin, F., and Shah, M., 1977, Peg-leg multiples and dipping reflectors: Geophysics, **42**, 957–981.

Matson, K., and Abma, R., 2005, Fast 3d surface-related multiple elimination using azimuth moveout for multiples, *in* 75th Annual International Meeting: Soc. of Expl. Geophys. 2064–2067.

Nekut, A., 1998, 3d surface-related multiple elimination, *in* 68th Annual International Meeting: Soc. of Expl. Geophys. 1511–1514.

Paffenholz, J., McLain, B., Zaske, J., and Keliher, P., 2002, Subsalt multiple attenuation and imaging: Observations from the sigsbee2b synthetic dataset, *in* 72nd Annual International Meeting: Soc. of Expl. Geophys. 2122–2125.

Rickett, J., Guitton, A., and Gratwick, D., 2001, Adaptive multiple subtraction with non-stationary helical shaping filters, *in* 63rd Meeting: Eur. Assn. Geosci. Eng. Session: P167.

Robinson, E. A., and Treitel, S., 2000, Geophysical Signal Analysis: Society of Exploration Geophysicists.

Rosales, D., and Biondi, B., 2005, Converted-waves angle-domain common-image gathers, *in* 75th Annual International Meeting: Soc. of Expl. Geophys. 959–962.

Ross, W., Yu, Y., and Gaspaarotto, F., 1999, Traveltime prediction and suppression of 3-d multiples: Geophysics, **64**, 261–277.

Sacchi, M., and Ulrych, T., 1995, High-resolution velocity gathers and offset space reconstruction: Geophysics, **60**, 1169–1177.

Sava, P., and Fomel, S., 2003, Angle-domain common-image gathers by wavefield continuation methods: Geophysics, **68**, 1065–1074.

Sava, P., and Guitton, A., 2003, Multiple attenuation in the image space, *in* 73rd Annual International Meeting: Soc. of Expl. Geophys. 1933–1936.

—, 2005, Multiple attenuation in the image space: Geophysics, **70**, 10–20.

Trad, D., 2003, Interpolation and multiple attenuation with migration operators: Geophysics, **68**, 2043–2054.

Verschuur, D., and Berkhout, A., 1997, Estimation of multiple scattering by iterative inversion, part ii: practical aspects and examples: Geophysics, **62**, 1596–1611.

Verschuur, D., Berkhout, A., and Wapenaar, C., 1992, Adaptive surface-related multiple elimination: Geophysics, **57**, 1166–1167.

Weglein, A., Gasparotto, F., Carvalho, P., and Stolt, R., 1997, An inverse scattering series method for attenuating multiples in seismic reflection data: Geophysics, **62**, 1975–1989.